AN AUTOMATED ALGORITHM TO EXTRACT FEATURES FROM RETINAL FUNDUS IMAGES TO DETECT DIABETIC RETINOPATHY AND ASSESS ITS SEVERITY USING DEEP LEARNING

Thesis submitted to

UNIVERSITY OF CALICUT

in fulfilment for the award of the degree of

DOCTOR OF PHILOSOPHY

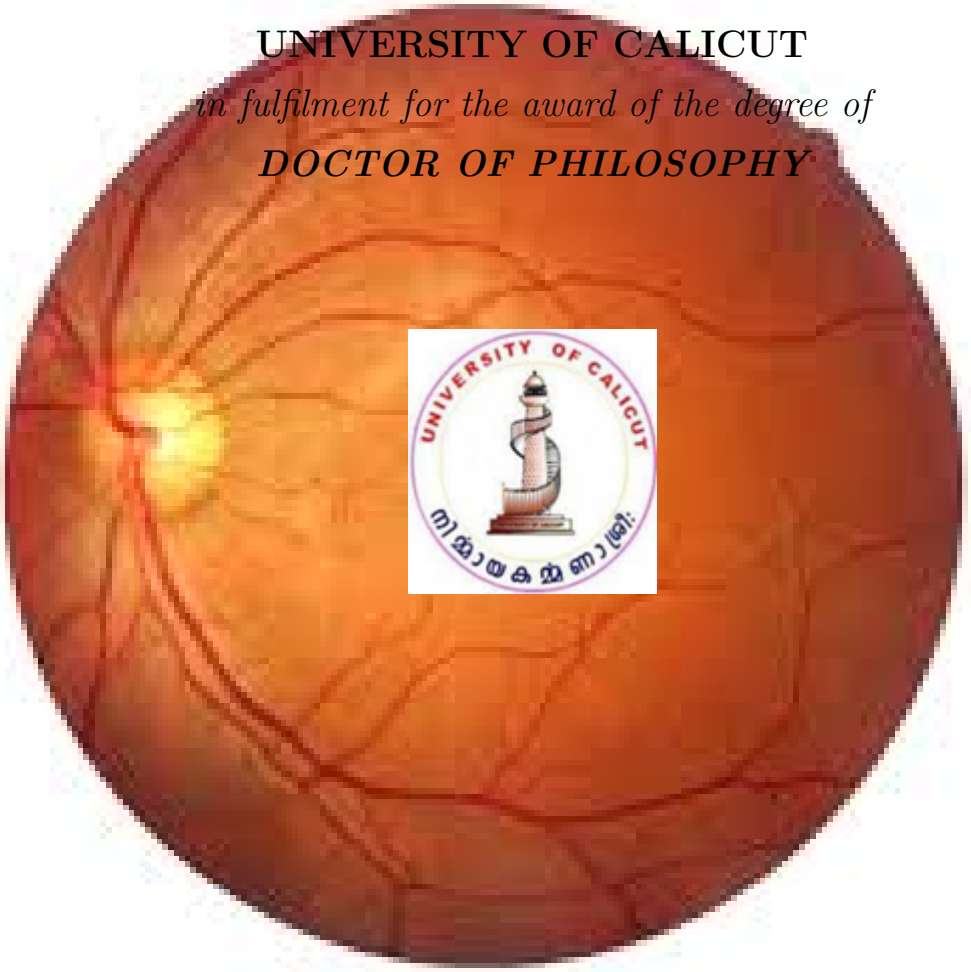

By

ANIL KUMAR K R

Department of Electrical and Electronics Engineering

Government Engineering College, Thrissur-9

University of Calicut

December, 2020

AN AUTOMATED ALGORITHM TO EXTRACT FEATURES FROM RETINAL FUNDUS IMAGES TO DETECT DIABETIC RETINOPATHY AND ASSESS ITS SEVERITY USING DEEP LEARNING

Thesis submitted to

UNIVERSITY OF CALICUT

in fulfilment for the award of the degree of

DOCTOR OF PHILOSOPHY

By

ANIL KUMAR K R

Under the Guidance of

Dr. K. Meenakshy

Professor

Department of Electrical and Electronics Engineering

Government Engineering College, Thrissur-9

University of Calicut

December, 2020

DEPARTMENT OF ELECTRICAL AND ELECTRONICS ENGINEERING
GOVERNMENT ENGINEERING COLLEGE, THRISSUR
Engineering College P.O., Ramavarmapuram
Thrissur, Kerala, India, Pin code:-680009
Phone No. 0487-2334144 Fax: 0487-2336124
Web site: www.gectcr.ac.in

Certificate

This is to certify that the thesis entitled **AN AUTOMATED ALGORITHM TO EXTRACT FEATURES FROM RETINAL FUNDUS IMAGES TO DETECT DIABETIC RETINOPATHY AND ASSESS ITS SEVERITY USING DEEP LEARNING** is the record of bonafide research work done by Mr. Anil Kumar K.R. under my supervision and guidance at Department of Electrical and Electronics Engineering, Govt. Engineering College, Thrissur in partial fulfilment of the requirement for the Degree of Doctor of Philosophy under Faculty of Engineering, University of Calicut.

Thrissur
26-12-2020

Dr.K.Meenakshy
Professor
Dept.of Electrical and Electronics Engg.
Govt. Engineering College, Thrissur

Certified that all corrections and suggestions by the adjudicators in their report of evaluation as communicated in the letter No. 213918/RESEARCH-C-ASST-1/2020/Admn Dated 17.06.2021 are incorporated in the thesis.

Thrissur
19-07-2021

Dr.K.Meenakshy
Professor
Dept.of Electrical and Electronics Engg.
Govt. Engineering College, Thrissur

Declaration

I, ANIL KUMAR K R, declare that this thesis titled, "AN AUTOMATED ALGORITHM TO EXTRACT FEATURES FROM RETINAL FUNDUS IMAGES TO DETECT DIABETIC RETINOPATHY AND ASSESS ITS SEVERITY USING DEEP LEARNING" and the work presented in it are my own. I confirm that:

- This work was done wholly or mainly while in candidature for a research degree at this University.
- Where any part of this thesis has previously been submitted for a degree or any other qualification at this University or any other institution, this has been clearly stated.
- Where I have consulted the published work of others, this is always clearly attributed.
- Where I have quoted from the work of others, the source is always given. With the exception of such quotations, this thesis is entirely my own work.
- I have acknowledged all main sources of help.
- Where the thesis is based on work done by myself jointly with others, I have made clear exactly what was done by others and what I have contributed myself.

Signed:

Anil Kumar K R
December, 2020

Abstract

Name of the student:	**Anil Kumar K R**
Degree for which submitted:	**Ph.D**
Department:	**Electrical and Electronics Engineering**
Thesis title:	**An Automated Algorithm to Extract Features from Retinal Fundus Images to Detect Diabetic Retinopathy and Assess its Severity Using Deep Learning**
Thesis supervisor:	**Dr.K.Meenakshy**
Month and year of thesis submission:	**December, 2020**

Diabetes may lead to retinal pathologies such as microaneurysms, hard exudates and haemorrhages, which are the early symptoms of Diabetic Retinopathy (DR). If these symptoms are not diagnosed at the early stage and left untreated, blindness may result. The diagnosis demands service of experienced ophthalmologists, but the number of patients to number of ophthalmologists is disproportionate. With this motivation an algorithm is developed to detect the presence of diabetic retinopathy and its severity level automatically from fundus images. This effort will assist in the early diagnosis and treatment of diabetic retinopathy. The work also describes methods for segmenting the main components of retinal fundus images (RFIs) such as blood vessels, optic-disc and fovea. Retinal image contrast is enhanced utilizing Non Subsampled Contourlet Transform (NSCT) and the Normal Inverse Gaussian (NIG) Probability Density Function (PDF). The suggested procedure employs the NIG distribution to attain the Bayesian maximum a posteriori probability of the membership values of NSCT coefficients. Mathematical morphology utilizing the multistructure elements is employed to identify ridges of the retinal blood vessels. Erroneous edges are removed by connected component analysis and length filtering. Area with the highest variation in intensity of adjacent pixels is recognized as optic disc and the darkest area adjacent to the

optic disc is identified as fovea. 8-connectivity region growing algorithm is used to localize optic disc and fovea. Normal retinal components extracted images are fed as input to Bag-of Visual Words (BoVW) model to differentiate normal and abnormal RFIs. The BoVW model along with speeded up robust features (SURF) descriptor provide 100% accuracy while classifying normal and abnormal RFIs. Finally deep learning algorithm utilizing the pretrained EfficientNetB4 network is used to assess the severity of DR in the abnormal RFIs. The algorithms developed is tested on images collected from DRIVE, HRF, e-Ophtha databases along with images obtained from a local hospital. Deep learning algorithm is tested on 3662 images obtained from Kaggle dataset. The performance of the classifier is evaluated using precision, recall, f1-score, accuracy and kappa score. The values obtained for these parameters reveals that the proposed classifier can be utilised for detecting and classifying the severity level of DR.

Acknowledgement

First and above all, I bow my head before the **Almighty** Lord whose grace has been with me always throughout the research work.

I would like to express my wholehearted gratitude to my supervising guide, **Dr.K. Meenakshy**, Professor, Department of Electrical and Electronics Engineering, Govt. Engineering College, Thrissur, for her valuable guidance, understanding, support and most importantly her friendly relationship during the whole period of my research. I also acknowledge her patience and guidance during the documentation process.

I would like to place on record my gratitude to **Sri. G.Sukumaran Nair**, Chairman, Governing Body, NSS College of Engineering, Palakkad for giving me the permission to do research on part time basis.

My sincere thanks to **Dr.Sheeba V.S.**, The Principal, Government Engineering College, Thrissur, also the internal Doctoral Committee member for her valuable suggestions and support. I am grateful to **Dr.R.Gopikakumari**, Professor, Division of Electronics Engineering, School of Engineering, Cochin University of Science and Technology (CUSAT), for her valuable guidance as the external Doctoral Committee member.

I must express my gratitude to **Prof.K.P.Preetha**, Head of the Department, Electrical and Electronics Engineering, Government Engineering College, Thrissur, for her support. I would like to thank **Dr.B.Jayanand**,Professor, Department of Electrical and Electronics Engineering, Government Engineering College, Thrissur, and **Dr.M.Nandakumar**, Former Head, Department of Electrical and Electronics Engineering, Government Engineering College, Thrissur, for their constant encouragement during my research work. I also thank all the faculty members and technical staff in Electrical and Electronics Engineering Department, Government Engineering College, Thrissur. I aslo thank all office staff of Government Engineering College, Thrissur for their help during the period of research.

I express my sincere gratitude to The Principal, NSS College of Engineering, Palakkad and all my colleagues in the Department of Electronics and Communication Engineering, NSS College of Engineering, Palakkad for their support and encouragement. I extend my gratitude to **Prof.P.Nandakumar**, Professor,Department of Electronics and Communication Engineering, NSS College of Engineering, Palakkad and **Prof. Vinod G.**, Associate Professor, Department of Electronics and Communication Engineering, NSS College of Engineering, Palakkad for providing timely help. I also acknowledge **Prof.Rajesh Menon B.**, Associate Professor, Department of Mechanical Engineering, NSS College of Engineering, Palakkad and **Dr.Suresh P.R**, Professor, Department of Mechanical Engineering, NSS College of Engineering, Palakkad.

I also thank my fellow researchers, **Dr.Benzy V.K.**, **Dr.Maya U.C.**, **Dr. Remya George**, **Prof.Premanand B.**, **Prof.Sunny T.D.**, **Prof.Manilal A.M.**, and **Prof.Jayadevan R.** for their support, encouragement and suggestions.

I am also indebted to **Anu S. Balan**, **Arya P.E.**, **Bhavyalakshmi K.K.**, **Chaithra Sree K.**, **K.V.Geethika**, **Megha P.M.**, and **Noushira K.I.** for their help during my research.

I gratefully acknowledge the efforts put by **Dr.Soman Nair** Specialist Ophthalmologist & Vitreoretinal Surgeon, Thumbay Hospital, Dubai, UAE and **Dr.S. Vishnumohan**, IVS Eye Clinic, G.B.Road, Palakkad for their help extended to complete this research work.

I am highly indebted to my **Parents** for their constant encouragement and support. I thank my wife **Dr.Anjana R.**, for the consistent encouragement and absolute support. I also thank my sons **Rohith Krishna A.K.** and **Rahul Krishna A.K.** for patiently co-operating with me to complete the work successfully.

Thrissur
December, 2020 **Anil Kumar K R**

Contents

List of Figures

List of Tables

List of Abbreviations

ACC Accuracy

ACM Active Contour Model

ACO Ant Colony Optimization

AI Artificial Intelligence

AUC Area Under the Curve

AutoML Automated Machine Learning

BoVW Bag of Visual Words

BPF Band Pass Filter

CAD Computer Assisted Diagnosis

CCA Connected Component Analysis

CHT Circular Hough Transform

CLAHE Contrast Limited Adaptive Histogram Equalization

CNN Convolutional Neural Network

conv_base Convolution Base

DFB Directional Filter Bank

DIP Digital Image Processing

DL Deep Learning

DM Diabetes Mellitus

DME Diabetic Macular Edema

DR Diabetic Retinopathy

DRRI Diabetic Retinopathy Risk Index

EXs Exudates

FIR Finite Impulse Response

FN False Negatives

FP False Positives

FRP False Positive Rate

FT Fourier Transform

GPD Gumble Probability Distribution

GPU Graphical Processing Unit

GVF Gradient Vector Flow

HMs Haemorrhages

HPF High Pass Filter

IEM Image Enhancement Metric

LPF Low Pass Filter

MAs Microaneurysms

MBConv Mobile inverted Bottleneck Convolution

MCA Morphological Component Analysis

MCC Matthews Correlation Coefficient

MNAS Mobile Neural Architecture Search

MSE Mean Square Error

NIG Normal Inverse Gaussian

NPDR Non-Proliferative Diabetic Retinopathy

NSCT Non-Subsampled Contourlet Transform

NSDFB Non-Subsampled Directional Filter Banks

NSFB Non-Subsampled Filter Bank

NSP Non-Subsampled Pyramid

NSWT Non-Subsampled Wavelet Transform

OC Optic Cup

OCT Optical Coherence Tomography

OD Optic Disc

OS Overlapping Score

PCA Principal Component Analysis

PDF Probability Density Function

PDR Proliferative Diabetic Retinopathy

PR Precision

PSNR Peak Signal-to-Noise Ratio

RFIs Retinal Fundus Images

ROC Receiver Operating Curve

RT Radon Transform

SBF Sliding Band Filter

SD-OCT Spectral Domain Optical Coherence Tomography

SE Sensitivity

SE Structure Elements

SEs Structure Elements

SEVERE SEgmenting VEssels in REtina images

SP Specificity

SPCA Sparse Principal Component Analysis

SSAE Tacked Sparse Auto Encoder

STARD Standard index

std Standard Deviation

SURF Speeded Up Robust Feature

SURF Speeded Up Robust Feature

SVM Support Vector Machine

T1D Type-1 Diabetes

T2D Type-2 Diabetes

TN True Negatives

TP True Positives

TPR True Positive Rate

Dedicated to My Teachers...

Chapter 1

Introduction

Eye is one of the sophisticated sensory organs in the human body. It works like a camera by focusing the visible light reflected from objects to the retina situated at the back of the eye. From there the images are transmitted to the brain. Changes happening in the anatomy of eye due to pathological or diseased condition will affect the vision and subsequently the quality of life. Hence it is highly important to identify even the minute abnormalities associated with the eye structure. The escalation in Digital Image Processing (DIP), Artificial Intelligence (AI), and modelling methods along with high performance computing has had a significant impact on the diagnosis and ministration of eye diseases. Digital fundus, Optical, Infrared, Optical Coherence Tomography (OCT), as well as Heidelberg Retina Tomography are a few imaging techniques to identify abnormalities of eye [1].

The retina doles out with an optimal expedient to investigate the part of microvascular pathology in the pathophysiology of cardiovascular diseases. Over the last tenner, progress in retinal vascular imaging empowered the development of explicit and dependable quantitative parameters such as retinal vascular calibers which are coupled to cardiovascular diseases. Variations in the vascular structure of the retina can point the existence of different types of pathology, such as arteriosclerosis, hypertension, myopia, proliferative diabetic retnopathy, and retnopathy of prematurity. But, there is little data on the interrelationship between retinal vascular calibers and the risk of diabetic retinopathy (DR) [2].

1.1 Introduction to Diabetic Retinopathy

As per International Diabetes Federation, in 2019 around 463 million adults (Age group:20-80 years) were living with diabetes. This number may increase to 700 million by 2045. 80% of adults with diabetes were living in low- and middle- in-

come countries [3].

Diabetic retinopathy is one of the complications of diabetes that affects the eyes. This complication occurs in 80% of diabetes. At its early stage, the disease sits silently in the background giving no symptoms. As a consequence the patient is ignorant of its presence. At this juncture, there is no immediate warning of sight impairment, but it is the onset of serious retina damage and it is considered to be the first phase of blood vessel declination. Roughly one-fifth of patients with these cases advance to the stage where vision is acutely damaged.

The distinguishing features of diabetic retinopathy are Microaneurysms (MAs), Haemorrhages (HMs), and Exudates (EXs). A retinal microaneurysm is a small region of blood sticking out from an artery or vein in the back of the eye. These bulging may open and leak blood into the retinal tissue surrounding it. Microaneurysms by itself are not likely to cause any symptoms that could be noticed. Almost all microaneurysms are reversible with treatment of diabetes, high blood pressure or other disorder causing them. Haemorrhages are impairments of the blood-retina barrier which come off either as a red 'dot' or flame-shaped. In the latter case, they have an idiosyncratically " feather-shaped" edge [4]. Hard exudates are tiny white or yellowish white deposits. They have sharp margins and look shiny, waxy or glistering. They are found in the outer layers of the retina, deep to the retinal vessels. Microaneurysms that come across as white dots without visible blood in the lumen are inferred as hard exudates.

One of the leading cause of vision impairments in the adults aged between 20 years and 70 years is diabetic retinopathy. This disease can be prevented and treated if the condition is given effective screening and management. Most people are oblivious to the fact that they have eye damage.

The most risky constraint to vision in diabetes give little or no warning. These initial changes can be seen only through direct examination with an ophthalmoscope and hence ministrations could be started before sight becomes seriously affected. Therefore to protect vision periodic thorough eye examinations are essential.

Diabetic retinopathy can be treated by laser surgery. Here a strong light beam is focused on to the retina. As a result the abnormal vessels shrink. Laser surgery has reduced the risk of severe sight loss from diabetic retinopathy by 90%. But usually laser surgery cannot restore the lost vision. Thus, early screening of

diabetic retinopathy is the best method to prevent vision loss.

1.2 Diagnosis of Diabetic Retinopathy

Routine check-up by an experienced ophthalmologist is important for early detection and treatment of diabetic retinopathy. DR administration requires screening huge numbers of people (About 30,000 individuals per million of the total population) [5, 6]. Proper screening can reduce the risk of DR by 70%. Also proper screening makes public health systems cost effective [7, 8]. Even though screening has been proved to be cost effective [9] the required number of ophthalmologists to perform the screening of all diabetics is very high [10]. Majority of methods to detect DR require intervention from an experienced personnel [11].

Conventional screening steps for diabetic retinopathy can be summarised as follows

1. Patient directed to the screener for examining his/her medical details.
2. Using a Snellen acuity chart best corrected visual acuity is tested.
3. Pupils dilated with Trepicamide 1% eye drops.
4. Obtain 4 images from the dilated pupils. Two from each eye.
5. Fundal examination is performed by medical staff to detect and classify the severity of diabetic retinopathy.

Current screening procedure demands the involvement of trained and experienced medical staff. Also the accuracy of screening is a big concern. There is a pressing demand for an inexpensive screening method free from intervention from trained ophthalmologist.

A fully automated method to analyse fundus image could classify retinopathy without the involvement of specialist. Digital fundus images provides us digitised data that could be used for computerised detection of several other diseases. Nowadays many investigators perform image analysis using computers, but they still require direction of a human observer. A fully automated method would greatly improve the management of diseases. Automated screening system is very much beneficial to those residing in rural areas who are unable/unwilling to travel to hospitals. It is possible to operate the camera by a minimally trained person,

since the examination is fully automated, and does not require human intervention.

A non-mydriatic fundus camera has been recommended as an appropriate means of diabetic retinopathy screening [12]. Its foremost advantages are that pupillary dilation is not required, it can be operated with an unskilled person and that it can be rather easily transported. Hence it sounds to be of value for use in the society. Assessment in the setting of hospital clinic has proven that, besides its limitations, in general the method gives better results when compared with ophthalmoscopic examination through a dilated pupil.

1.3 Fundus Camera

A variety of special equipments have been developed to image the eye. This section describes one of the common clinical instruments-the fundus camera-for capturing fundus images.

In this camera, the light beams emerging from two sources, an incandescent lamp meant for viewing the fundus and a flash lamp for photography, are optically combined using a beam splitter as demonstrated in Figure 1.1.

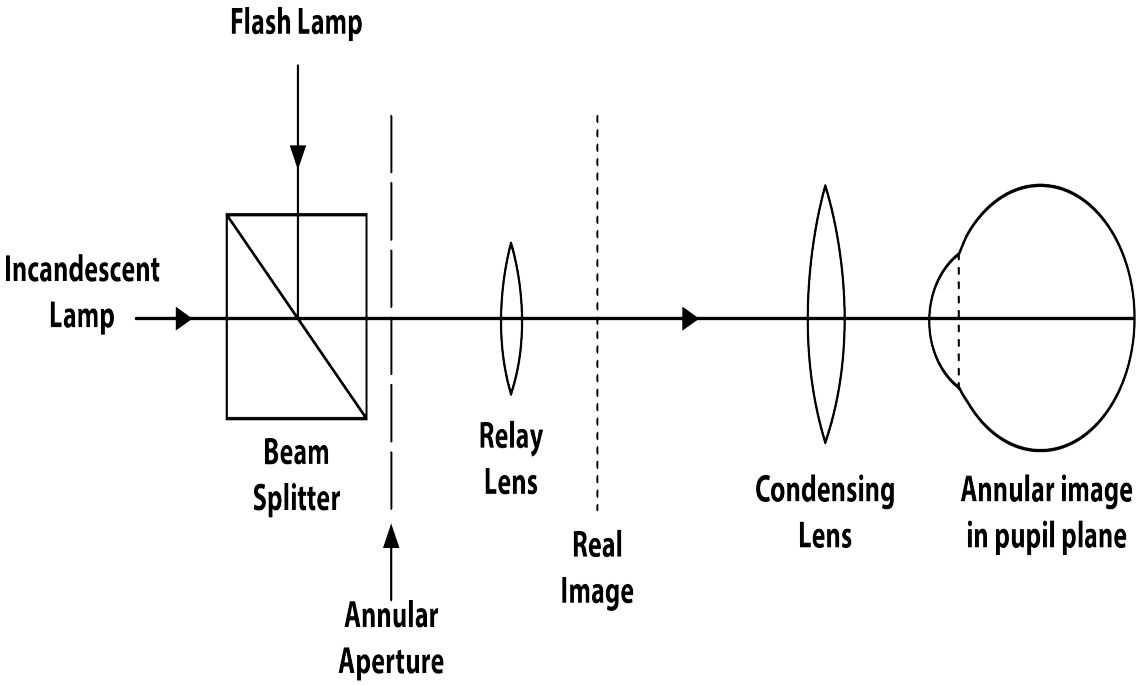

Figure 1.1: Illumination system of fundus camera. [13]

The combined light sources are confined to an annulus using an iris di-

aphragm that controls the outer diameter. To capture and position the annular aperture in the plane of the patients's pupil an auxiliary condensing lens is fitted in the equipment.

The diagram in Figure 1.2 demonstrates how the fundus image is observed with a normal camera. The condensing lens is used to form the image. The camera lens focuses on this image. The movable mirror, also known as beam splitter, cater a separate path for observation. This system is akin to an ophthalmoscope. There exists two major differences between these two. One is that the viewing beam is confined with an aperture which is mirrored in the pupil plane and the other is that image magnification is achieved using a microscope. The illumination and viewing beams in the pupil plane are separated. This ensures that no light reflected by the corner or condensing lens enters the viewing system. Thus the viewing system accomplishes a reflex-free image. By correcting the astigmatic errors of the candidate's eye the image quality is improved.

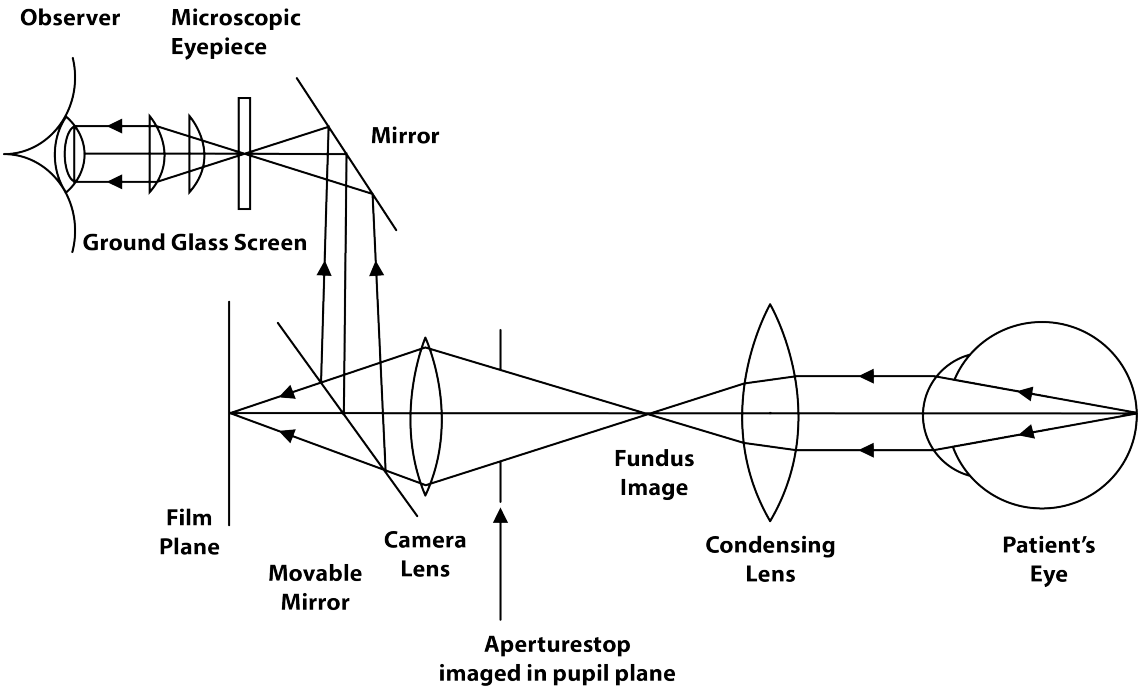

Figure 1.2: Observation system of fundus camera. [13]

Many different methods exists to combine viewing and illumination systems. One of the methods reflects the illumination beam by ensuring both apertures are imaged in the same plane but are physically separated. Here the aperture stop

in the observation system is the central hole in the tilted annular mirror. Thus a simple iris diaphragm can be used in the illumination beam. Various techniques also prevail for combining observation beam and camera and observation systems and the illumination.

Fibre optics are used to furnish annular illuminations in some illumination systems. In some other systems, infra-red illumination is employed. Here a visible display unit screen converted from an infra-red sensitive video camera is used as a visible display of the image. This unique method reduces pupil construction from the illuminating beam [13].

A fundus camera brings an upright and magnified image of the fundus. A typical fundus camera have a field of view of 30^0 to 50^0 of the retinal area. It also provides a magnification of 2.5 times which can be extended upto 5 times with the use of some auxiliary lenses. The field of view can be increased upto 150^0 by giving penalty to the peripheral image quality. Figure 1.3 shows a fundus camera. Figure 1.4 depicts a normal fundus image where the structures on the fundus includes the blood vessels, optic disc, fovea and macula.

Figure 1.3: Fundus camera.

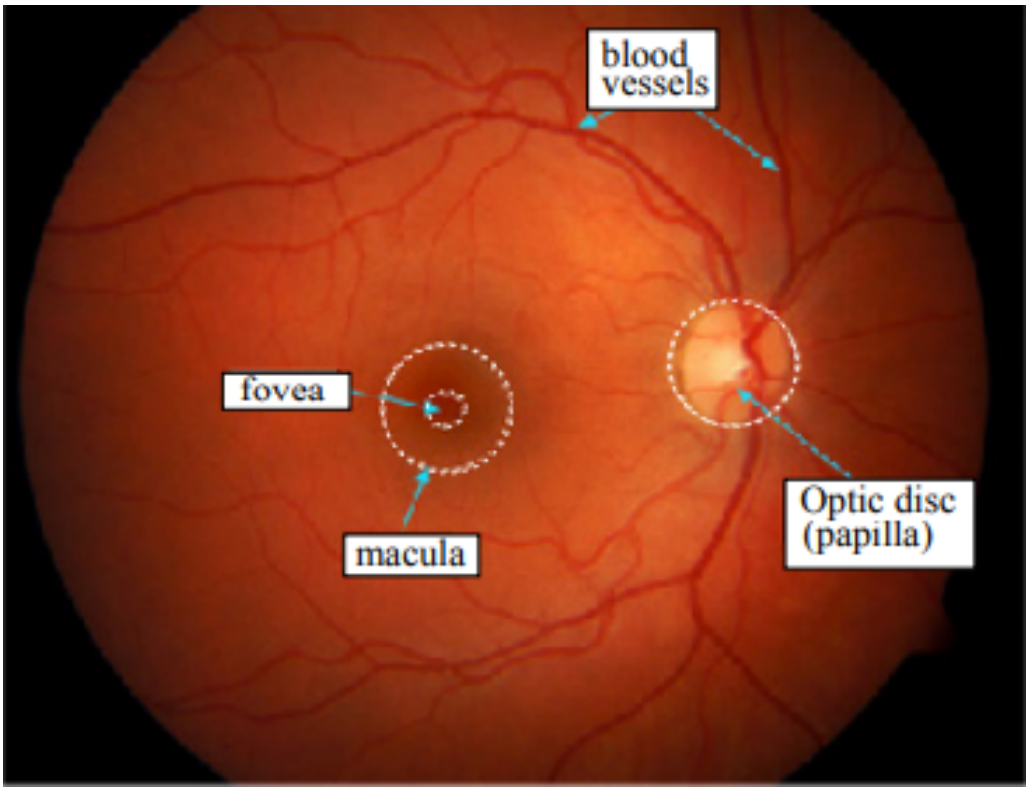

Figure 1.4: The normal fundus image.

1.4 Motivation

At present around 463 million adults are living with diabetes. This number can grow up to 700 million by 2045. Among this diabetic affected people 80% are from low- and middle- income countries. Also 80% of diabetes are prone to diabetic retinopathy. In the developing stage DR does not give any symptoms and so patients are unaware of its presence. But, if untreated, this will lead to vision impairment. As per International Diabetes Federation, roughly $\frac{1}{8}^{th}$ of the people affected by DR advance to the stage where their vision is permanently damaged. Proper screening among diabetes can reduce the chance of diabetic retinopathy. The fact that the ratio of number of diabetic patients to number of experienced ophthalmologists is very large prevents people from under going routine eye examination. If the presence of DR can be detected by an automated system developed through technical means we can prevent the advancement of the disease to vision loss. Since the developed system does not require the expertise of an ophthalmologist, the identification of the disease can be performed in equipped medical labs similar to routine check ups. This is the motivation behind this work.

1.5 Objectives

The main objectives of the current work are

1. Development of a novel fundus image contrast enhancement technique without affecting the diabetic retinopathy features present in it.
2. Detect the presence of diabetic retinopathy from fundus images.
3. Classify the severity of diabetic retinopathy in detected cases.

1.6 Structure of the Thesis

This thesis elucidates research steered towards developing a technique for an automatic diagnosis of DR and assess its severity. The thesis layout is as follows.

Chapter 1 introduced diabetic retinopathy and its diagnosis procedure. An over view of fundus camera is also presented in this chapter. The chapter concludes with the motivation and objectives of this work. The contents of the subsequent chapters are also briefed here.

Literature review is carried out in Chapter 2. An extensive survey is conducted by reviewing papers published in this field especially for the last six years. The review is presented under different aspects like blood vessel extraction, Optic disc and cup segmentation, EXs, MAs, and HMs detection and CAD based DR detection. The chapter ends by pointing out the scope of further research in the field of automatic DR detection.

Chapter 3 describes the pre-processing algorithm developed to enhance the image contrast. Image pre-processing is carried out by using non-subsampled contourlet transform. In this proposed enhancement method the term contrast is considered as a qualitative rather than a quantitative measure.

Extraction of anatomical features of retina, an important step in DR identification, is explained in Chapter 4. The blood vessels are extracted using multistructure elements morphology by reconstruction. Chapter 4 also describes how region growing algorithm can be effectively used to localize optic disc and fovea.

Chapter 5 deals with the detection of Diabetic Retinopathy. Bag-of-Visual-Words model (BoVW) is used to correctly identify the DR affected images. The results obtained confirms that BoVW model can be used as a binary classifier which classify normal and abnormal images.

Chapter 6 introduces deep learning approach to classify retinal images as per the severity level of DR. The newly introduced EfficientNetB4 is used for performing transfer learning. The kappa score obtained for the classifier confirms that the classifier obtained is a perfect classifier.

Chapter 7 gives conclusion of the work proposed and it also points out some further research scope in this area.

The frame work of this thesis is represented in Figure 1.5.

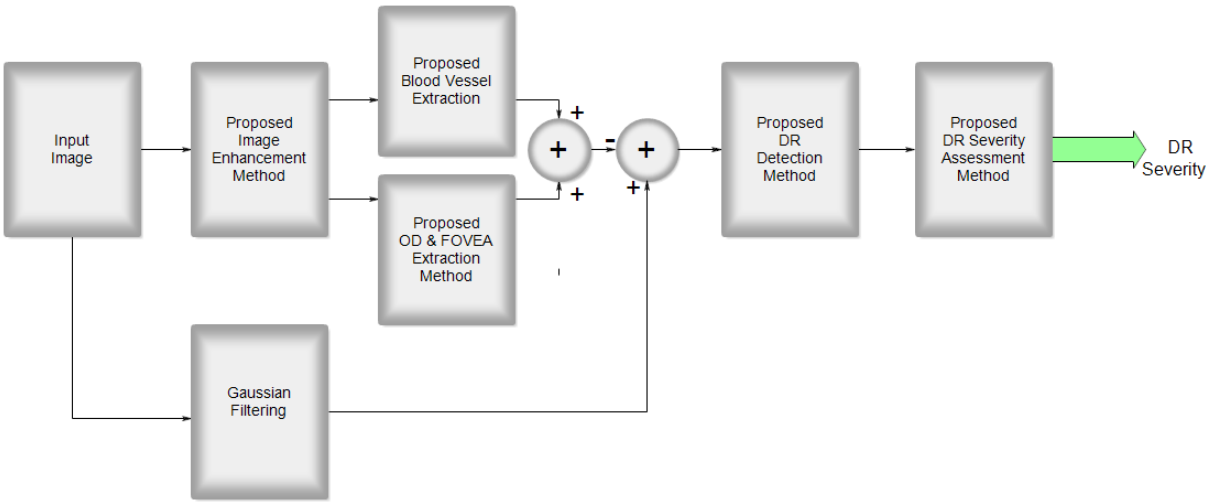

Figure 1.5: Framework of the thesis

Chapter 2

Literature Review

Diabetic Retinopathy is a complication widely prevalent among diabetic patients. The increased glucose level in blood causes changes in the microvasculature of retina. The threat of DR lies in the fact that it does not show any pre-emptive symptoms. Hence it ends with sheer vision loss. But despite that, screening at the beginning and appropriate treatment can control the ascendancy of DR. But non-automatic examination of morphological variations in the retinal components are tiresome and incapable of being surmounted. Therefore, Computer-Assisted Diagnosis (CAD) methods were accomplished to aid ophthalmologists for checking intra- and inter- diversities. In this chapter, a latest survey of modern CAD systems for detecting and classifying DR is presented. This chapter come up with most of these CAD methods that have been accomplished by different computational intelligence and image processing approaches. The bounds and hopes of contemporary CAD systems are as well depicted comprehensively to aid researchers. Furthermore, existing CAD techniques are quantitatively evaluated concerning their statistical parameters. The comparison results signify the need for more accurate CAD systems to aid in the quantifiable diagnosis of DR.

2.1 Introduction

Diabetes Mellitus (DM) is described by a pool of unbalancing changes carried out by insulin resistance [14]. Insulin secretion elicits an increase in blood glucose ratio known as hyperglycaemia. This may slowly but surely start to develop macro (stroke, and heart attack) and micro (neuropathy, retinopathy and nephropathy) vascular pathologies [15]. As per the statistics mentioned in [16], there exists around 382 million humans figured out as diabetic patients and this value is supposed to touch 592 million by 2030. Type-1 Diabetes (T1D) and Type-2 Diabetes (T2D) are the two main categories of DM. Around 90% of di-

abetic patients in the world have T2D, which is due to insulin resistance. One of the significant impact of DM is diabetic retinopathy. It develops a progressive vision loss, especially in the elder population, due to the downfall of tiny retinal vessels [17, 18, 19]. Even so, testing and treatment at the initial stage via CAD techniques can help candidates to prevent complete vision impairment.

The pathognomonic signs of DR are the appearance of microaneurysms (MAs), soft/hard exudates (EXs), and hemorrhages (HMs) in the fundus image. Bulges of this vessels which come off as petite and sharp boundaries of red papules retinal surface are MAs. EXs are formed because of the leakage of proteins from vessels. They look like small white/yellowish-white spots. Leaky capillaries cause HMs and they appear as red deposits with jagged margins. On the basis of vessel deterioration and ischemic change, DR is broadly grouped into non-proliferative diabetic retinopathy (NPDR) and proliferative diabetic retinopathy (PDR). NPDR is again divided into mild (existance of MAs), moderate (exalt than mid-level), and severe (venous edging in at least two quadrants, MAs, HMs in four retina quadrants) stages. Top-level stage of DR is PDR. Clinically NPDR is suggested for the determination of the severity level of DR [20, 21, 22, 23].

CAD programs are employed to gracefully analyse and extract basic retinal components (Blood vessels, Optic disc, fovea, cup, and macula) as well as abnormal lesions (EXs, MAs, and HMs) contained by the retinal image for the early detection of DR. A clinically followed protocol for DR screening is given in Table 2.1. This table [24] exhibits the DR classes along with their clinical definitions.

Table 2.1: A typical scale for DR screening [24]

DR Types	**Clinical Features**
Normal	No abnormal lineaments
Mild NPDR	Found MAs
Moderate NPDR	Maximum number of MAs, EXs, and HMs
Severe NPDR	All abnormal features in four quadrants
PDR	All abnormal features with new blood vessel formation

Progress in the area of science and engineering has built human life more harmonious by making it secure and healthier. Say, modernistic medical image analysis is a unique field of research that calls attention to life threatening diseases by means of imaging technology. Such modernistic diagnosis systems also known as CADs extend services for making our life easier. The capacity of CADs has been established in different fields of medical diagnoses, like glaucoma detection,

DR detection, tumor detection, alzheimer's as well as parkinson's identification, gastrointestinal assessment, cardiac grading, macular edema and a lot more [24]. The results rendered by these CAD systems are very similar to that obtained from human inspection. The success of CAD devices banks on the features separated out from images with the help of computational methods [25]. Manual observation of retinal anatomical structures (such as vessels, optic disc, fovea, cup, and macula) and lesions of DR is a tiresome and repetitive one for clinical staff. In addition, manual analysis is highly subjective and demands very good technical domain expertise to inspect intra- or inter- variations in retinal elements. Hence, CAD methods are necessary to carry out early DR screening utilizing fundus images. These CAD techniques may save cost, time, and effort of medical practitioners during the manual observations of retinal images [26, 27].

In bygone days a number of authors have surveyed and studied various retinal image analysis techniques along with their applications [28, 29, 30]. An exhaustive scrutiny of the image segmentation approaches for cup, optic disc, and DR identification was demoed in [28]. A different work [29] emphasized image processing, extraction of normal and odd retinal traits, and DR diagnosis approaches. In [30] Patton *et al.* came up with a review on the image preprocessing, cellular feature extraction, image registration and various imaging modalities for DR detection. But, none of them reviewed and correlated advanced machine learning methods. Ergo, in this chapter an exhaustive assessment of the state-of-the art CAD methods for the pinpointing of normal and anomalous retinal traits are divulged. Particularly, image processing, machine learning, advanced deep learning, and computer-vision based approaches are pinned down for the timely detection of DR from color fundus photography.

2.1.1 Digital Fundus Imaging

Fundus imaging has empowered automated screening methods to handle and block out various retinal disorders devoid of the involvement of clinical specialists. Generally, the acquisition of a fundus image is accomplished by the fundus camera. It inhold a microscope (low power) which is able to capture the inner part of the retinal structure, namely the posterior pole, macula, optic disc, and cup. Figure 2.1 is a portrayal of a common fundus image, which exhibits the basic fundus quiddity and NPDR levels with lesions. Fundus imaging had proved to be an easy and lucrative technique aiding ophthalmologists to rapidly analyse and sort images collected from various locations, e.g., urban or rural areas, and then come

up with expedient clinical recommendations. At this juncture it is significant to note that fundus arteriography accomplishes DR diagnosis utilizing three kinds of imaging modalities: (i) An RGB (ii) A red exempted channel and (iii) fluorescent images [31]. Specimens of these channels can be found in the DRIVE, DIARETDB, MESSIDOR, STARE, and HRF databases [32, 33]. These clinical resources have usually been selected by R & D people to design DR-based CAD systems.

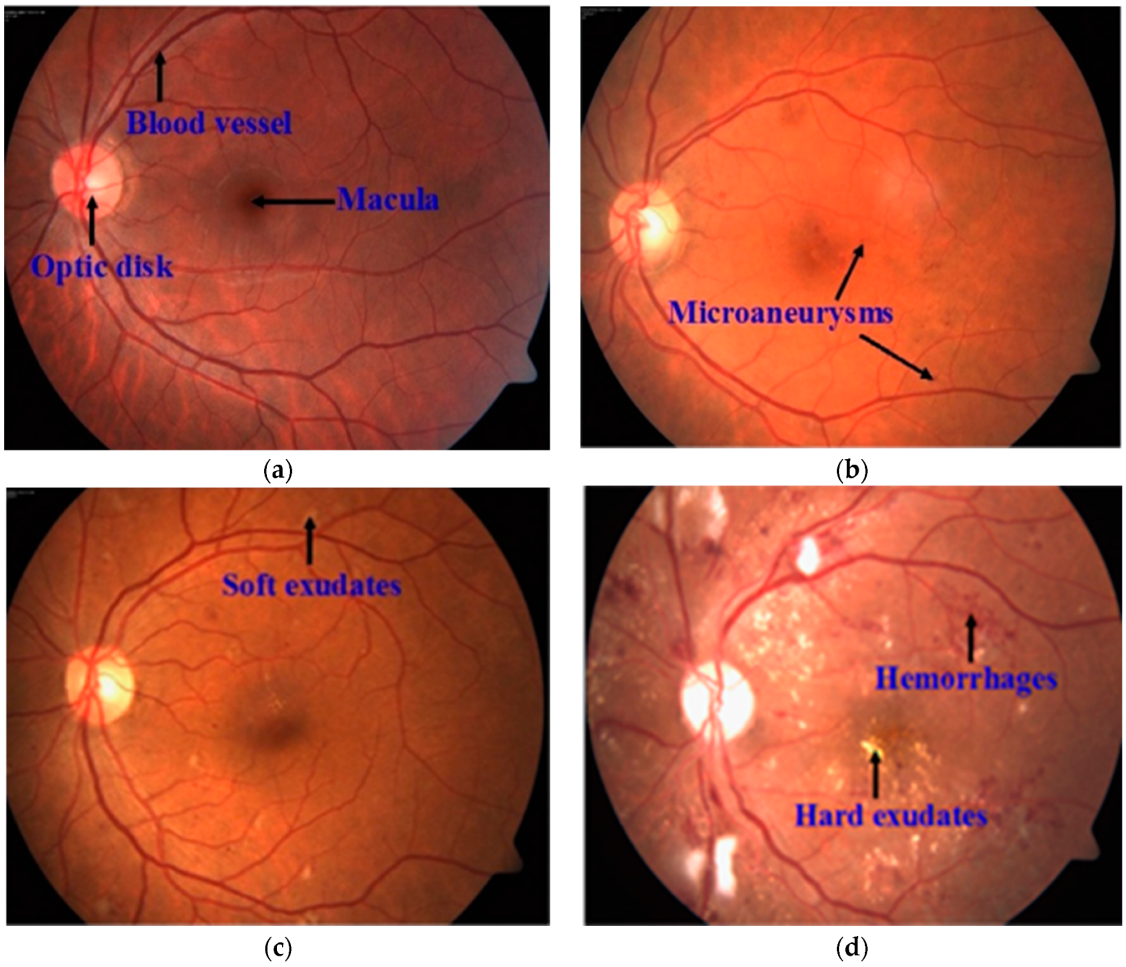

Figure 2.1: Example of a fundus images.(a) Retinal anatomic features (b) Mild NPDR (c) Moderate NPDR (d) Severe NPDR [34]

2.1.2 Performance Measure

The most desirable feature of DR-based CAD systems is that they can engender a real-time DR filtering mechanism which produces accurate and reliable results in nominal time. To test and assess the effectiveness of those CAD techniques against the ground truth (i.e. manual abstraction of features provided by ophthalmologists) labels, different statistical parameters/measures, like sensitivity (SE),

accuracy (ACC), specificity (SP), precision (PR), area-under the curve (AUC), and F1-Score are used to give an objective assessment of these methods. The parameters are based on true positives (TP), true negatives (TN), false positives (FP), and false negatives (FN).

- TP (True Positives), signals exact classification of a patient.
- TN (True Negatives), imply a normal person is correctly classified.
- FP (False Positives), shows an incorrect classification of a disease unaffected person as a patient.
- FN (False Negatives), denotes incorrect classification of a patient as normal person.

The formulas intended for SE, ACC, SP, PR and F1-Score are given in (2.1) to (2.5).

$$SE = \frac{TP}{(TP + FN)} \tag{2.1}$$

$$ACC = \frac{TP + TN}{(TP + FP + TN + FN)} \tag{2.2}$$

$$SP = \frac{TN}{(TN + FP)} \tag{2.3}$$

$$PR = \frac{TP}{(TP + FP)} \tag{2.4}$$

$$F1 - Score = \frac{2TP}{(2TP + FP + FN)} \tag{2.5}$$

An AUC value of 1 confirms good performance of the technique while an AUC value of 0.5 establishes a moderate performance [35].

The goal of this chapter is to explore and illustrate the state-of-the-art self-acting scientific systems, i.e., deep learning, and conventional methods for DR-dependent CAD systems. An examination into the construction, datasets, and experimental outcomes, along with pivotal gaps in these approaches are furnished comprehensively. Lastly, the review is wrapped-up with some panaceas to the examined algorithm's flaws and aspiring directions in the development and training of more effective DR detection methods based on deep learning.

This chapter is organised as follows. Section 2.2 presents segmentation and extraction techniques of retinal blood vessels, optic disc & optic cup, microaneurysms & hemorrhages, and Exudates. Section 2.3 concisely explain the recent developments in popular CAD based methods for DR detection. Section 2.4 put

forth a survey on the contemporary DR-based screening systems. Section 2.5 provides an insight into the challenges of the discussed methods along with some solutions. This section also gives a comparison between traditional hand-crafted and deep learning methods used to screen DR. Finally, the chapter is concluded in Section 2.6.

2.2 Identification Methods of DR

The subsequent sections furnish a sweeping survey of topological segmentation and grading systems brought forth for the identification of anatomic signs of retina with DR lesions employing fundus photographs. Figure 2.2 shows a vivid illustration of these identification techniques.

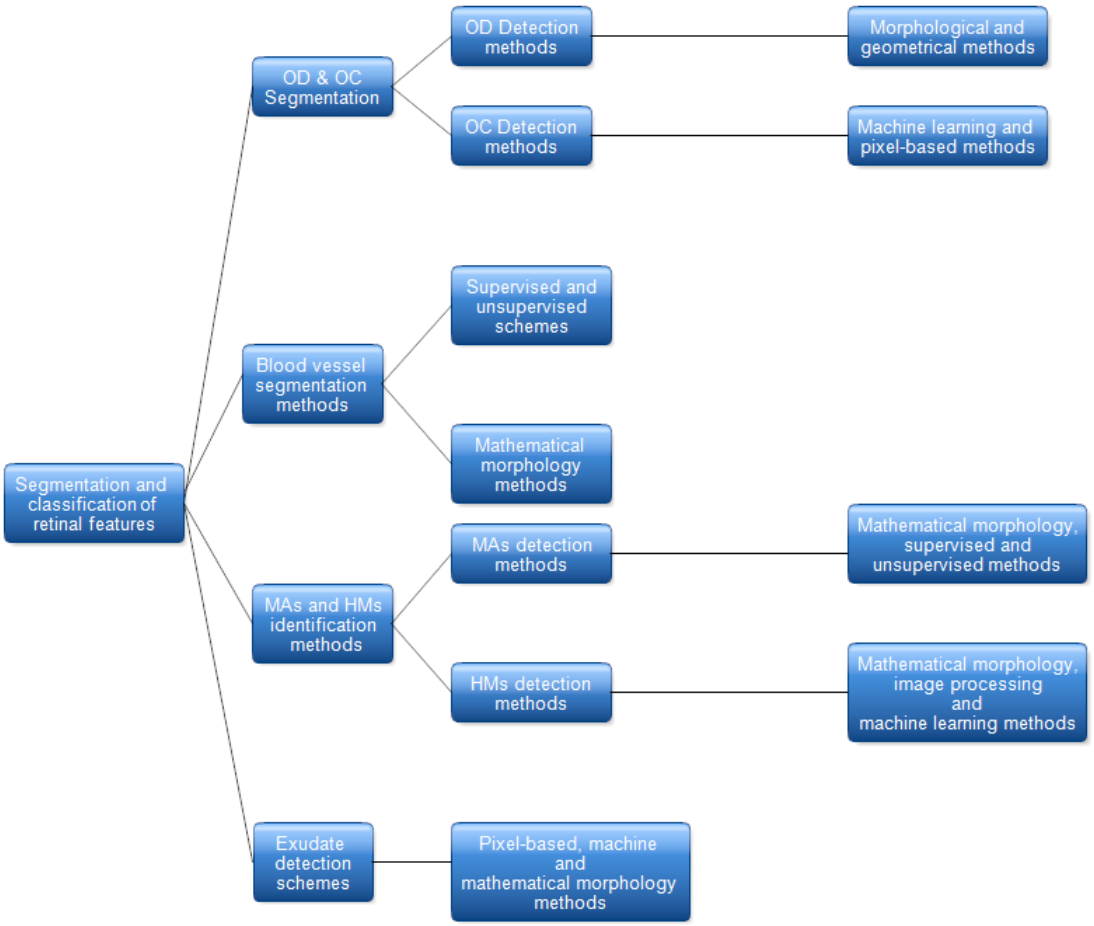

Figure 2.2: DR detection methods

2.2.1 Blood Vessel Extraction

The task of confirmation of structural variations of the retinal vascularization in color fundus photography is a judicious and ceaseless one for clinicians. The reliability of the DR-CAD system highly depends on the accuracy of vessel segmentation. Further, identification of vessel features that are based on geometry and secular changes of vessels -depicted in Figure 2.3- helps inexperienced doctors in the exact diagnosis of DR.

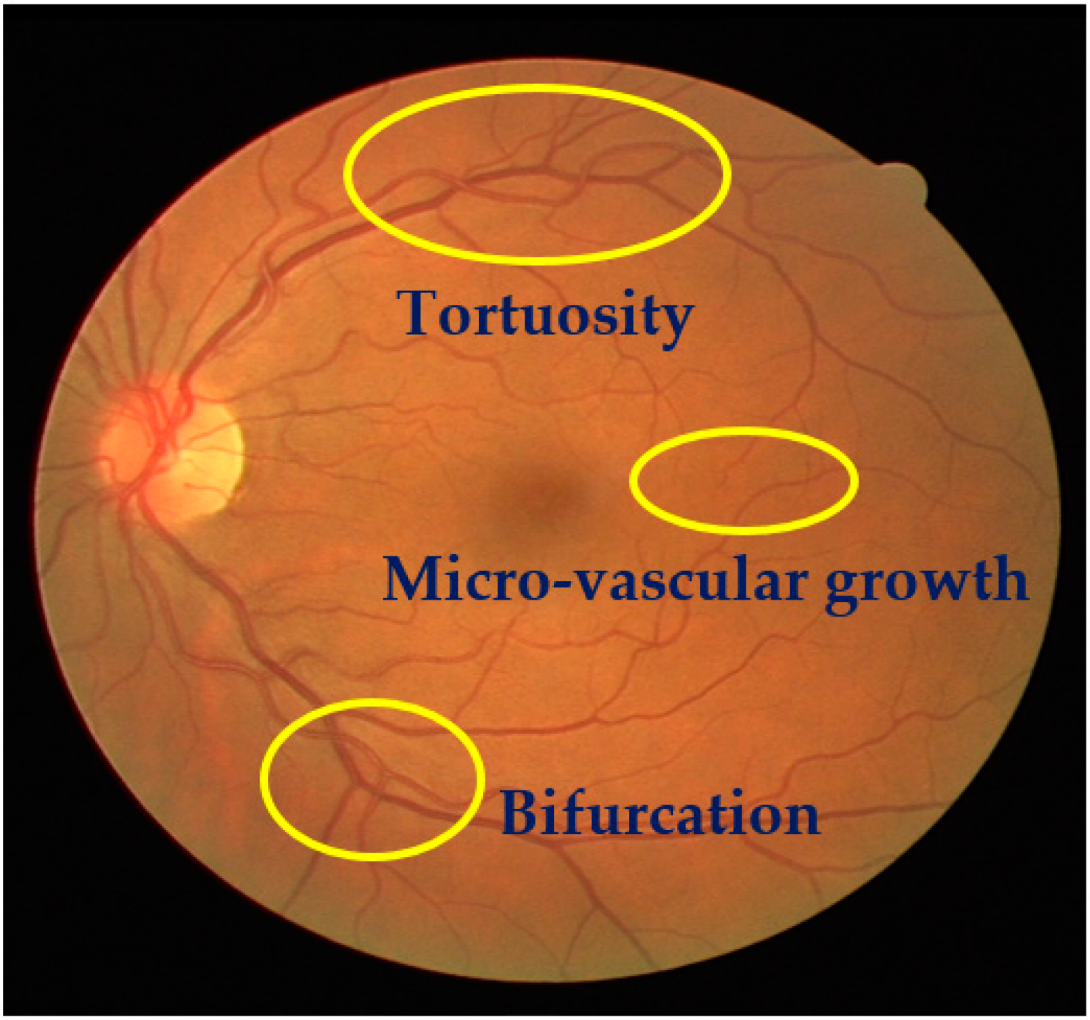

Figure 2.3: A fundus image displaying secular variations of vessels [34]

The available methods in the literature for segmentation of retinal vessels can be categorized into supervised-, unsupervised-, and mathematical morphology-based methods.

Kaur and Mittal in [36] proposed a vascular structure detection method from

pathological retinal images. Initially preprocessing is carried out to nullify the effects of low-contrast and non-uniform illumination. A matched filter is used to extract the intensity of pixels and geometric features. These features are then passed to a neural network which separate vessel from non-vessel region. The authors claimed an accuracy of 95.45%. The results obtained are given in Figure 2.4. But, the method had less impact in the identification of lesions that bring about a false vascular structure.

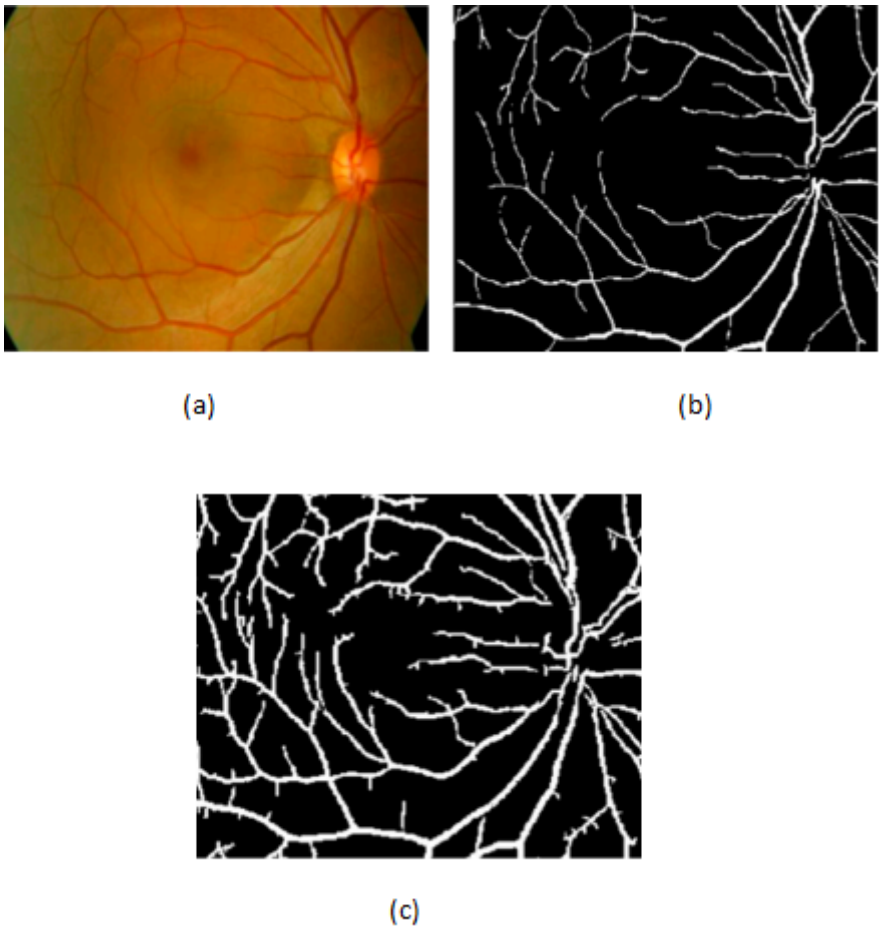

Figure 2.4: Results of blood vessel extraction [36]

(a) Original image (b) Ground truth (c) Extracted vessels

An unsupervised coarse extraction approach for vessel identification is presented in [37]. They combined multiple concepts like mathematical morphology, spatial dependency, and curvature with coarse-to-fine technique to exactly describe thin and elongated vessels from vessel pixels. Meanwhile, the technique failed in determining the vessel diameter and also rated as inefficient in extracting vessel structures from low contrast images. Variations in the structural and

micro-pattern of vessels were identified by extracting vascular features using textural descriptors. A random forest classifier then distinguish true vessel points from non-vessel one [38]. The authors reported 96.1% and 92.2% sensitivity and specificity values respectively. A compendious review of vessel segmentation algorithms are provided in [39, 40, 41].

The work in [40] assorted common and uncommon retinal features with inhabitant's contextual information at varying coarseness levels via data mining techniques to segment vessels from fundus images. This work utilized a larger dataset and the obtained results were more significant than that obtained with the then existing methods. But, the system execution time was exorbitant. A different work [41] used the consecutive execution of image pre-\post- processing and data mining techniques for vessel extraction. They obtained an accuracy of 95.36%. The downside of this method is its elongated processing time. The specificity score obtained was also unsatisfactory for vessel extraction. In [42] Zhang *et al.* recommended an unsupervised approach for vessel extraction in which labelling conflicts from ground truth labels were rectified. A texton dictionary was generated using key point descriptors to discriminate vessel pels from on-vessel pixels. Even though this method yielded an accuracy of 95.05%, it struggled with false positive results on the left part of the peripheral region and around the disc. These drawbacks can be tackled with some pre-processing methods. Tan *et al.* [43] achieved a classification accuracy of 94.54% for the segmentation of retinal vessels by utilizing a seven layer convolutional neural network. Wang *et al.* [44] segmented retinal vessel by using a CNN model with ensemble learning. After image normalization they used CNN and random forest classifier to separate vessel from non-vessel. They yielded an accuracy of 97.5% at the expense of considerable training time. A few machine learning methods have proved to have an exceptional potential in vessel extraction using retinal angiography, e.g., gumbel probability distribution (GPD) [45], hybrid feature vector and random forest classifier [46], and direction map [47]. The method in [46] combined robust features from different methods into a 17-dimensional space for vessel pixel description. The random forest classifier process these feature vectors to identify vessel and non-vessel pixels. This method yielded 96% accuracy with increased computational cost due to the use of thirteen gabor filters to filter vessel features.

A unique matched filter termed GPD was brought into play after enhancing image sharpness using Principal Component Analysis (PCA) gray-scale conversion and dynamic local sharpness enhancement techniques [45]. A cycle of examines were conducted to find out an appropriate parameter. A GPD filter was then de-

signed using this selected parameter. Lastly, lucider vessel structures were filtered after post-processing followed by thresholding and length filtering. The authors reported an AUC of 0.91. The stringers in [47] endorsed a direction map blueprint called SEVERE (segmenting vessels in retina images) for vessel extraction. The method was void of preprocessing steps. Using the green component image from the RGB color image and direction map the blood vessel patterns were segmented. The accuracy obtained was 97%. Hassan *et al.* [48] utilized mathematical morphology along with a smoothing operation to segment retinal vessels accurately. K-means algorithm was used for the classification of vessels. The classification accuracy obtained was 96.25%. An unsupervised method was put forth by Eysteinn *et al.* [49] for retinal vessel assortment. The model obtained a assortment accuracy of 94% by using morphological approach and fuzzy classification. The main limitation of this method was that it depended on human labelled data. Moreover, the method was computationally expensive.

Delineation between slender and chunky retinal vessels has turned into a grueling task because of low contrast and non-uniform illumination of images as well as the presence of bright lesion. So, hybrid techniques such as fuzzy conditional entropy techniques, the phase-preserving denoising approches, and saliency with active contour modes were presented in [50, 51, 52] to identify slender and chunky vessels. The work in [53] was a multimodel mechanism for segmentation of thin and thick vessels. A phase-conservating line detection technique after the removal of image noise was used to identify thin vessels. A maximum entropy thresholding method was employed for identifying thick vessels. This method recorded an AUC value of 0.95 in the demarcation of slender and chunky vessels in retinal images. In a previous work [51] an integrated system was developed for the automated filtration of different structures of blood vessels from retinal fundus images. Normalization of the original images were carried out employing curvelet transform denoising. To filter the image noise and to enhance the image contrast a band pass filter (BPF) was used. The fuzzy conditional entropy algorithm identified the best threshold by using a matched filter response. Various vessel structures, like slender, medium, and chunky were identified with an average accuracy of 96.22% using the differential evolution technique on the best thresholds. The idea of retinex theory-multiplication of reflection and illumination attributes-was employed to stabilize thin vessel contrast as well as global image quality. After that, an image was split into super-pels and fed to the saliency method to locate unique vessel regions. The result obtained was refined using an infinite active contour model. The AUC value reported for this method was a 0.8 [52].

Line detection as well as pictel-based methods were employed in [54] for the extraction of tiny vessels. Image pre-processing followed by line detection technique was employed for image segmentation. In order to localize long and medium size vessels adaptive thresholding method was utilized. Finally, small vessels were extracted with the pixel-based tensor voting procedure. Farokhian *et al.* in [55] put forward a bunch of 180 Gabor filters followed by an imperialism competitive algorithm-an optimization method- for vessel extraction and achieved a precision score of 93%. A Gabor filter is defined on the turning degree of 1 scale to identify image and vessel borders. An optimization technique was then applied for exact vessel identification. Likewise, a template matching method utilizing a Gabor function was put forward in [56] for the identification of center vessel lines (after specifying the region of interest) as well as filtration of low contrast thin vessel structure. The method presented a 96% accuracy value. A binary segmented image was obtained utilizing the template matching technique. Then the contours of the binary image were reproduced to match the attributes of the image with that of the manually marked up contours in the training dataset. Finally, slender vessels with low contrast were segmented using a large dataset. Each of these mathematical morphology-based techniques were believed as being unsatisfactory because of the following reasons: (i) methods were evaluated on a small dataset and had restricted cover of the varied-sized locations of an image (ii) plenty of pre-/post-processing steps were employed to segment the vessel tree (iii) reported a longer running time during the extraction of vessel structure.

Kar and Maity in [57] presented a blood vessel segmentation algorithm derived from the matched filter followed by curvelet transform and fuzzy c-mean algorithm. To begin with, a curvelet transform was employed to identify edges and lines. Then a vessel tree was extracted utilizing a fuzzy c-mean algorithm. Even though their method reported an accuracy of 96.75% it failed to attain a better true positive rate. Zhao *et al.* in [58] presented a level set and region growing technique for the extraction of retinal vessels. They obtained 94.93% accuracy. A compact and low power hardware architecture was proposed in [59] by Koukounis *et al.* for the exact segmentation of retinal blood vessels. Their technique include three steps. First, the green channel of an RGB color image was taken during the preprocessing phase to enhance the quality of image. Second, a matched filter was employed on the normalized image to feature the vessel points. Lastly, various thresholds were utilized for exact vessel identification. However, the method was costlier with respect to the acquiring and loading of images. A morphological component analysis was put forward in [60] for the segmentation of retinal vessels. Vessel contrast was improved before applying morphological component

analysis. However, the method was restricted to the identification of complex image attributes such as lesions and vessel tortuosity. A recap of important blood vessel identification methods are displayed in Table 2.2, accentuating the employed methods and datasets.

2.2.2 Optic Disc and Cup Segmentation

The optic disc (OD), or optic nerve head is the locus of departure for ganglion cell axons exiting the eye. Due to the absence of rods or cones in the optic disc, it corresponds to a tiny blind spot in each eye. It is treated as initial indicator of optic cup (OC), retinal vessel, fovea, and macula identification in fundus images. Locating and extracting the OD periphery indicates a disc contour and centre. Predominant OD segmentation methods in the study are established on geometrical- and morphological- based approaches, as outlined in the coming paragraphs.

Taking into account the importance of OD segmentation for dependable glaucoma and DR identification, Bharkad S. in [61] counted morphological features to filter out the OD edge. The finite impulse response filter (FIR) was employed to filter out retinal vessels as well as to bring out morphological attributes for disc segmentation. The method recorded a mean accuracy of 98.95%. However, he used a small dataset and the method was futile on low contrast color images. In a similar way, Alshayeji *et al.* in [62] used a boundary detection procedure derived from a gravitational law followed by pre- and post- processing processes for OD extraction. The method achieved 95.912% accuracy with a price of increased execution time. A contemporaneous technique was devised in [63] for OD extraction. In this approach the disc edge was segmented following the elimination of vessel utilizing a region growing dynamic threshold and ellipse fitting approach. The accuracy achieved for this method was 91%. Singh *et al.* in [64] utilized the green component of a fundus image that provide much higher information for OD detection. They claimed an accuracy of 94.7%. Abed *et al.* in [65] put forward a nature-inspired hybrid model termed swarm intelligence with pre-processing step for OD separation. The mean accuracy reported by the authors was 98.45% with fewer execution time than other lithographed approaches. Contradictorily this method is greatly based on pre-processing steps and inclined to algorithm parameters.

Various other CAD procedures have been accomplished utilizing the geometrical attributes for OD extraction with greater accuracy. Examples of these

Table 2.2: Blood vessel extraction methods - A recap

Classification Technique	**Database**	**Size**	**Color Space**	**Accuracy(%)**
Morphological component analysis[60]	DRIVE, STARE	60	8 bits	95
Level set and region growing [58]	DRIVE, STARE	60	8 bits	94.93
Matched filter and fuzzy c-means [57]	DRIVE, STARE, DIARETDB1	149	8 bits	96.75
Fuzzy classification [56]	DRIVE	40	24 bits	96
Mathematical morphology, k-means [55]	DRIVE	40	8 bits	93
Gumbel probability distribution [52]	DRIVE, STARE	60	8 bits	AUC:0.9287
Hybrid feature and forest classifier [51]	DRIVE, STARE	60	8 bits	96.22
Template matching [53]	DRIVE, STARE	60	8 bits	96
Gabor filter [49]	DRIVE	40	24 bits	94
Saliency and contour model [47]	DRIVE, STARE	60	8 bits	97
Fuzzy conditional entropy [45]	DRIVE, STARE	60	8 bits	-
Phase-preserving method [46]	DRIVE, STARE, HRF, CHASE_DB1	133	8 bits	96
CNN and RF [44]	DRIVE, STARE	60	8 bits	97.5
CNN [43]	DRIVE	40	24 bits	94.54
Segmentation [42]	DRIVE	40	24 bits	95.05
Classification [38]	MESSIDOR, HRF, STARE, Local dataset	779	24 bits	AUC:0.922
Local coarse segmentation [37]	DRIVE, STARE	60	8 bits	87
Geometrical features [36]	DRIVE, STARE, ARIA, HRF	785	24 bits	95.45

methods include the sliding filter [66], the Hough circle cloud [67], active contour model [68, 69], and ensemble of probability models [70]. In an earlier work [67], a fully automated program named Hough circle cloud was built for OD localization. The method offered an accuracy of 99.6%. But, the model requires a powerful

graphical processing unit (GPU) and was tested on a relatively smaller dataset. The system suggested in [70] dealt with the strength of various object identification techniques for OD extraction. The authors claimed an accuracy of 98.91%. Natheless, the procedure was analytically expensive. i.e., centered on pre-/post-processing steps and vulnerability of every algorithm member existed. To pinpoint the OD area a multi-resolution sliding band filter (SBF) was exploited in [66]. A low resolution/precision SBF was utilized after the removal of the blood vessels to achieve an early detection of the disc. High precision SBF was then used on the obtained disc points to attain a final OD abstraction. The final disc area was chosen by taking the maximum number of respopnses from a high precision SBF and smoothing technique. The reported average overlapping area is 85.66%. But, this procedure was seriously non-competitive on an intricate pattern of a couple of retinal samples. The works presented in [68, 69] reported a performance appraisal of ten region-dependent active contour models for OD extraction. Out of these procedures, the gradient vector flow (GVF)-ACM was discovered to be the winner with an accuracy of 97%. Despite this, both of these techniques were tested on tiny datasets accompanied by pre-/post-processing steps.

In [71] the authors utilized the vessel direction, intensity and bright area of the disc to detect the disc area. Geometric methods were combined with the confidence score method to extract these features. Accurate segmentation of OD is indicated by the highest confidence value. Even though the algorithm was registered as robust in the existence of other bright lesions with 98.2% accuracy, the evaluation was carried out on a comparatively smaller number of images.

Optic cup periphery filtering is a monotonous task due to the amalgamation of blood vessels nearby the cup region. Besides, OC-a brightest yellowish characteristic region of the fundus image-remains inside the disc region and initial signs of glaucoma retinopathy are visible in the OC [72, 73]. OC screening procedures in the collected works can be divided into pixel-based classification methods and machine learning based methods as outlined in the following paragraphs.

Tan *et al.* in [74] proposed a completely self-acting OC recognition procedure derived from a multi-scale super-pixel classification model. The authors utilized various ranges of multi-scale pixel methods and means for retinal image standardization and vessel extraction. At the end, the cup region was localized by sparsity based multi-scale super-pixel models. Even though 7.12% better rate than other OC localization procedures were obtained, the computational cost of the scheme was more. The method proposed in [75] put forward entropy sampling

and a convolutional neural network (CNN) for segmenting optic cup and disc. The yielded classification accuracy was 94.1%. But the method used a small amount of images and was futile in rendering the sampling data points to achieve more dependable results.In [76] Chakravarty and Sivaswamy put forward a combined segmentation scheme for disc and cup boundary. Using coupled and sparse dictionary approaches textural characteristics of the disc and cup were extracted. Finally these chosen features were applied for cup detection. The area under the receiver operating curve value obtained for this method was 0.85. Neverthless, their suggested method was less powerful in calculating the cup-to-disc ratio. Ant Colony Optimization method was utilized in [77] for segmentation of OC. The reported AUC was 0.79. This scheme was not successful on a few instances to point out the cup edge. Compatible attributes of disc as well as cup from fundus and spectral domain optical coherence tomography (SD-OCT) techniques have offered great potential for OC segmentation [78]. In [79] Issac *et al.* applied an adaptive threshold approach to segment disc and cup from fundus images. Features of fundus images like mean and standard deviation (std) were utilized for the removal of background parts of OD and OC. Lastly, the boundaries of OD and OC were segmented from green and red channels, as demonstrated in Figure 2.5 and Figure 2.6. The authors yielded 92% accuracy. However, the method was evaluated on a tiny dataset. Also it was ineffective on low contrast images. A recapitulation of the aforesaid disc and cup extraction algorithms/methods are shown in Table 2.3, illuminating the method, dataset used, and the number of images.

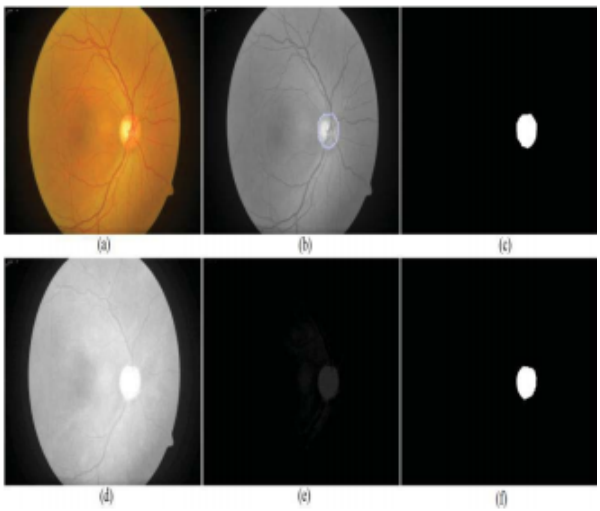

Figure 2.5: (a) Color fundus image (b) Gray scale ground truth (c) Extracted ground truth (d) Red channel image (e) Pre-processed image (f) Extracted OD [79]

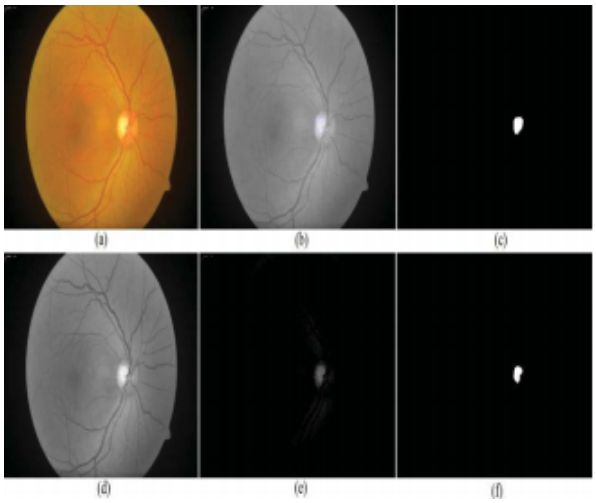

Figure 2.6: (a) Color fundus image (b) Gray scale ground truth (c) Extracted ground truth (d) Green channel image (e) Pre-processed image (f) Extracted OD [79]

2.2.3 DR-Connected Lesion (MAs and HMs) Identification Techniques.

MAs and HMs identification and extraction are tough tasks because of the varied size, textural features, and color of the fundus images. Hence, the design of swift and dependable automated DR lesion identification systems are still a promising area for researchers. A couple of studies considering exact MAs and HMs identification were observed in the literature. Microaneurysm analysis methods were categorized into supervised-, unsupervised-, and mathematical morphology- based methods, while hemorrhage extraction methods were divided into image processing, mathematical morphology, and machine learning-based approaches as outlined in the coming subsections.

In [80] Habib *et al.* described a smart MAs identification scheme utilizing color fundus photographs. Gaussion matched filter was employed to extract MAs attributes. These attributes were then given as input to a classifier- the tree ensemble classifier- to separate true and false MAs pixels. The receiver operating curve score (ROC) obtained was 0.415. But this method did not bypass the overfitting problem. Also it was unable to describe a standard feature selection principle. Kumar *et al.* in [81] utilized greenchannel image of RGB retinal image to extract MAs regions. Watershed transformation was used to remove blood vessels and

Table 2.3: OD and OC extraction methods - A recap

Method	Database Used	Size	Color Space	ACC(%)
Optic Disc Segmentation Methods				
Active contour model [71]	Private dataset, RIM-ONE, DIARETDB0	59	8 bits	98.2
Active contour models [69]	RIM-ONE	169	8 bits	97
Sliding band filter [66]	ONHSD, MESSIDOR, INSPIRE-AVR	1339	8 bits	-
Ensemble models [70]	DIARETDB0&1, DRIVE, MESSIDOR	1459	24 bits	98.91
Hough transform [67]	DRIVE, DIARETDB1, DIARETDB0, DRIVE	129	8 bits	99.6
Swarm intelligence [65]	DRIVE, DiaRet, DMED, STARE	318	8 bits	98.45
Wavelet features [64]	Local dataset	63	24 bits	94.7
Region growing [63]	MESSIDOR, DRIVE, Local dataset	1384	8 bits	91
Edge detection [62]	DRIVE, DiaRet, DMED, STARE	303	8 bits	95.91
FIR [61]	DRIVE, DIRATEDB0, DIRATEDB1, DRIONS	369	24 and 8 bits	98.95
Optic Cup Segmentation Methods				
An adaptive threshold [79]	Private dataset	63	8 bits	92
Ant colony optimization [77]	RIM-ONE	159	8 bits	-
Sparse dictionary [76]	RIM-ONEv2, DRIONS-DB, MESSIDOR, DATASET-1	1577	8 bits	-
CNN [75]	DRISHTI-GS	50	24 bits	94.1
Super pixel classification [74]	ORIGA		65024 bits	-

optic disc. A Gaussian matched filter was used to extract MAs. The authors reported 93.41% accuracy. Sreng *et al.* in [82] segmented MAs with the help of canny edge and maximum entropy-based methods. The image was normalized to remove vessel and disc area. Then MAs regions were extracted by employing canny edge and entropy methods along with morphological operation. The method reported 90% accuracy. Both methods described in [81, 82] were not successful in beating spurious signal during the detection of MAs. The authors in [83] employed three filters namely Gaussian, median and krich filters to the green component of an RGB retinal image to filter MAs characteristics. These characteristics were then applied as input to a multi-agent model to classify MAs pictels from non-MAs pictels. The method yielded an ROC of only 0.24. Also the authors did not evaluate all possible image locations for optimizing the detection process.

In an earlier work [84] a sequence of image processing methods like contrast improvement and feature extraction were employed to put forward some original hypothesis for enhancement of MAs detection programmes. Wu *et al.* [85] has taken some local and profile characteristics for MAs detection. After applying some image denoising techniques a k-mean based neural network classifier was employed on the image attributes to divide MAs pixel from non-MAs ones. The ROC value obtained for this method was 0.202. This method failed to localize MAs pels in very noisy images. In [86] Romero *et al.* presented a bottom-hat and hit-or-miss transform techniques for MAs segmentation succeeding a normalization process of image. Bottom-hat transformation was used to achieve a faithful reddish area with a bright part. Hit-miss transformation was applied to remove blood vessels. Finally, true MAs pixels were detected with an accuracy of 95.93% using principal component analysis and radon transform. Likewise, a top hat trasformation and an average-based filter was utilized in [87] for the detection and removal of retinal anatomic features with a 100% specificity. Subsequently, Radon trasform (RT) and multi-overlapping window were applied for the bifurcation of anoptic nerve head and MAs. This method reported a SE of 94%. Both methods in [86, 87] were analytically costiler and could not track down MAs points in the low sharpness images. For the detection of poor and small MAs features, a naïve Bayes classifier and position-based sharpness improvement approaches were applied in [88, 89], with considerable MAs results.

In [88] initially a loutish segmentation technique was used to ascribe the MAs candidate pixel. In addition, naïve Bayes classifier was employed to segment MAs pictels and separate actual and fake MAs points, resulting a classification accuracy of 99.99% with 82.64% sensitivity. But despite that, the naïve Bayes

classifier was computationally costiler and was also unsuccessful on obscure and blur MAs pictels. A contrast limited adaptive histogram equalization (CLAHE) technique was employed in [89] to solve the above mentioned draw backs. Here the input image was split into tiny and associated tiles in order to figure out tiny and low sharpness MAs pixels. The authors reported a sensitivity of 85.68%. But this approach was tested only on 47 images. This limits the method's generalizability. A sparse representation classifier followed by dictionary learning was applied in [90] to identify MAs pixels. Localization of the MAs region was carried out with a Gaussian correlation filter. Then, these MAs characteristics were fed into the sparse representation classifier to separate true and false MAs pixels. The reported sensitivity value was 0.8%. However, in this method the dictionaries were created faithlessly, thus missing the discriminative power during the detection process. Akram *et al.* in [91] furnished a model with 99.4% accuracy to classify MAs. Even though, the method was computationally overpriced, it provided better attributes for enhancing the differential power of the classifier. In order to reduce false positives during the MAs detection and overcome the class unbalance problem in color photographs, sparse principal component analysis (SPCA) and ensemble-based dynamic over-sampling methods were used in [92, 93]. The methods reported an average AUC score of 0.9. Javidi *et al.* in [94] segmented MAs from fundus images using morphological analysis and discriminative dictionary learning along with sparse representation. Localization of MAs candidate pixels were carried out with the help of morelet-based wavelet transform. Then binary dictionaries were used to identify MAs and non-MAs points. The authors acquired 0.267 ROC score. The results obtained with this method were depicted in Figure 2.7. However, the method takes a long execution time. Also it was incapable of detecting MAs pixels on unclear and poor contrast images.

Figure 2.7: MAs detection result [94]

In [95] Shan *et al.* suggested a deep learning approach namely stacked sparse auto encoder (SSAE) for the detection of MAs. At first, images were split into image tiles. These tiles were then fed to SSAE model which outputs high-level

features. Lastly, a soft max classifier was employed in the output layer to distinguish true and false MAs. The authors yielded an AUC of 96.2%. A different work [96] achieved MAs and HMs extraction using multiple kernel filtering. It was a two-layer approach. Here in order to handle the varied size lesions the image is split into small patches. Finally, a support vector machine (SVM) was used to separate true MAs and HMs points. They obtained an AUC of 0.97. Another machine learning algorithm to detect MAs was presented by Adal *et al.* in [97]. Here various scale-based descriptors were employed on normalized image for feature extraction. A semi-supervised learning procedure was trained with the filtered candidate attributes to separate MAs and non-MAs pixels, achieving an AUC of 0.36. The works in [95, 96, 97] failed to manage the over-fitting problem associated with much larger datasets. Also those methods yielded low distinctive capability. A overview of the MAs detection techniques mentioned so far is presented in Table 2.4.

Kaur *et al.* in [98] proposed a supervised algorithm for the identification of hemorrhages. The method used a dataset of size 50 images. Initially, fovea and vessels were removed using morphological closing operation. Then by adopting Otsu's thresholding HMs points were extracted. Finally a random forest classifier was employed to discriminate HMs and non-HMs pixels. The method yielded 90.4% SE and 93.53% SP. the results obtained are furnished in Figure 2.8.

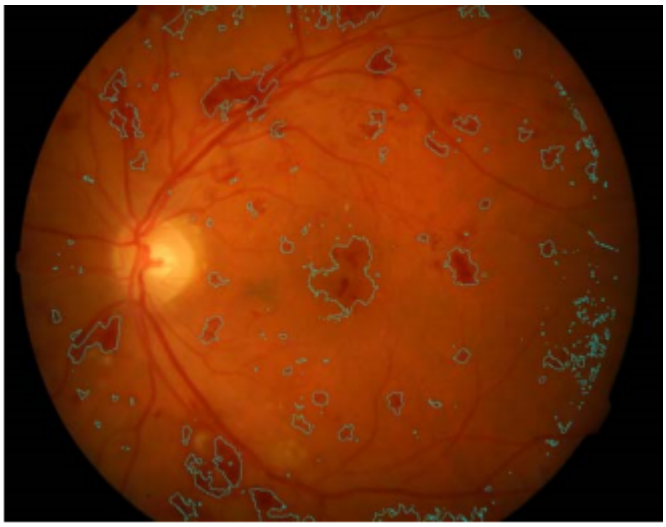

Figure 2.8: HMs detection result [98]

The method put forward in [99] also utilized Otsu's method to remove the vascular structure prior to HMs detection. The authors used 219 fundus images and achieved 92.6% SE and 94% SP. Both methods [98, 99] failed to identify hemorrhages closer to the border of the image aperture. In order to deal with the main

Table 2.4: MAs extraction methods - A recap

Classification Technique	**Data-set used**	**Size**	**Color Space**	**Accuracy(%)**
semi-supervised learning [97]	ROC, Private	400	8 bits	-
Multiple kernel learning [96]	DIARETDB1, MESSIDOR	143	8 bits	ROC:0.97
SSAE [95]	DIARETDB	89	24 and 8 bits RGB	AUC:96.2
Sparse and dictionary learning [94]	ROC	1008 bits-		
Ensemble learning [93]	e-optha	148	8 bits	AUC:0.844
SPCA [92]	ROC	100	8 bits	-
Hybrid classifiers [91]	DIARETDB0&1	219	8 bits	99.40
SRC [90]	ROC	100	8 bits	-
Contrast enhancement [89]	Private	47	8 bits	-
Naïve Bayes classifier [88]	Private	80	8 bits	99.99
RT [87]	Mashhad, local, ROC	192	8 bits	-
PCA and RT [86]	DIARETDB1, ROC	189	16 bit	95.93
Local & profile features [85]	ROC & e-optha	198	8 bits	-
Multi-agent model [83]	LaTIM	36	8 bits	-
Canny edge, threshold [82]	DIARETDB1	89	24 bits	90
Gaussian filtering [81]	DIARETD1	89	8 bits	93.41
Tree ensemble [80]	MESSIDOR, DIARETDB1v2.1	256	8 bits	ROC:0.415

difficulty during HMs detection-i.e. detecting HMs that are closer to the blood vessels- rule based mask detection [100], splat feature extraction [101, 102, 103] and fundamental information of inter-/intra-retinal structures [104] were employed and produced notable quantitative results.

The work reported in [100] removed blood vessels, disc, and fovea after performing image contrast enhancement and image normalization. Three Gaussian templates were applied to detect HMs region. This method yielded 93.3% SE and 88% SP. As mentioned above the schemes presented in [101, 102, 103] applied splat-based HMs extraction but with varied configurations. These methods pro-

vided better visual results. But they did not provide better numerical results while using so many number of tested images. Using mathematical morphology as well as template matching techniques the authors in [104] detected HMs with an exactness value of 97.7%. Machine learning and pixel-based methods for the extraction of HMs were outlined in [84, 105, 106]. In an earlier work [84], a great deal of unmanned DR screening and monitoring approaches for HMs identification were considered regarding their basic configuration, issues, datasets, and solutions. This work provided the importance of self-acting screening systems in DR classification. The computerized HMs identification schemes in [105] applied an brightness equalization approach on the green component of the RGB image to narrow down white and HMs pels. Support vector machine was then utilized onto the narrow downed region and HMs pictels were separated from normal pixels. Another technique for HMs identification that used 89 retinal images was presented in [106]. Here adaptive thresholding and morphological operations were applied to locate the HMs affected regions. The accuracy reported for this method was 90%. Nonetheless, the schemes [105, 106] were analytically complex and were restricted to covering whole likely areas of an image. Identically, in a previous work [107] a three steps HMs identification scheme using 108 images was presented. Based on the different intensities of fundus components bright features were localized. After extracting four texture forms a classifier was trained with the help of textural attributes to discriminate HMs and non-HMs pixels with 100% accuracy.

2.2.4 Exudate Extraction Schemes

Exudate- a key indication of DR- appear as vivid white/yellowish blot on the retinal surface. In the published writings, EXs filtering methods were brought into three groups: (i) pictel-based (ii) mathematical morphology based and (iii) machine learning based. The succeeding paragraphs discuss such EXs extraction methods.

Anatomical retinal marks, like a drawn out nervous system and optic disc bring about the generation of false positives in the computerized detection of EXs. So morphological matched filter and saliency techniques were applied by Liu *et al.* in [108] to remove vessels and the OD prior to EXs detection. To begin with, input RGB retinal image was pre-processed to note anatomical features and to improve the image sharpness. Then, employing a matched filter and saliency methods vessel and disc components were pulled out to exactly find the EXs area. Lastly, a random forest classifier was employed on the derived attributes-i.e. color, size,

and sharpness of EXs. Accuracy of 79% and an SE of 83% were yielded using 136 fundus images. Imani *et al.* [109] separated blood vessels from the exudate region by considering morphological component analysis (MCA) model. To distinguish EXs from normal features, mathematical morphology and dynamic thresholding techniques were employed. The method reported an AUC value of 0.961 using 340 images.

In an earlier study [110] EXs were detected using 83 retnal images by employing a multiprocessing scheme. First, gray morphology was applied to extract an exudate candidate area. Then Active Contour Model (ACM) model was used to segment boundaries of these extracted EXs candidates. Finally, the ACM component features were given to the naïve Bayes classifier to classify exudate characteristics. The method reported 85% accuracy and 86% sensitivity. Zhang *et al.* in [111] introduced an EXs extraction scheme derived from mathematical morphology using 47 images. At first images were normalized. EXs traits were extracted with an AUC score of 0.95 by employing classical and textural characteristics along with mathematical morphology. The authors in [112] also extracted exudates using mathematical morphology and the SVM classifier. They obtained 90.54% accuracy. An average-variance method for vessel and disc extraction was proposed in [113]. EXs points were selected using filter bank. Classification of EXs and non-EXs pictels were achieved by employing a Gaussian mixture with an association of the m-mediods model. The reported AUC score for this method was 0.97 using 1410 images.

In [114] Omar *et al.* put forward a region based multi-scale local binary pattern texture approach for the identification and classification of EXs. The method was varified using 130 images and achieved 96.73% accuracy. Morphological operations such as normalized cut, meanshift, and cannys had produced better results in EXs detection [115]. A variety of machine learning approaches had exhibited superior sensitivity results for EXs extraction [116, 117, 118, 119, 120, 121, 122, 123]. In [116] Fraz *et al.* utilized morphological reconstruction along with a Gabor filter to pull out EXs pixels. This procedure was checked using 498 images. At first, contextual cues were used to cut down false positives in chosen candidates. Region based attributes were derived from the candidate area. These features were then given to an ensemble classifier that detect actual and false EXs with a ROC value of 0.99. Prentasic *et al.* in [124] recommended an exudate extraction method using a deep CNN. Probability maps of various methods and Frangi filter were used to pull out the OD and blood vessels respectively. Finally, the output of deep CNN was merged with the disc and vessel extraction end results to filter actual

EXs pixels achieving a 0.78 F-score. Likewise SVM classifier with sparse coded features, visual dictionaries, K-means and scale invariant feature transform were utilized in [125, 118, 119] to discriminate true and false EXs points. Hard exudates were successfully extracted from fundus images in [120] using logistic regression. Then a multilayer perceptron and radial basis function classifier were employed to classify hard exudates. This method was tested in a database that contains 130 images and the method yielded a 96% sensitivity. The final classification results of any method largely depends on the accuracy of ground truth data. Usually these ground truth data have an inaccuracy problem. This unfaithfulness was eliminated in a previous study [121] by considering image features. ACO method was applied in [122] to extract edges of EXs using 169 numbers of low sharpness images. The green component was preferred due to its better intensity of EXs pixels with respect to the background image part. A 50×50 kernel sized median filter was applied to standardize and restraint the intensity space. EXs points were extracted using a double threshold. Lastly ACO was applied to identify the edges of bruise, resulting a 97% accuracy. In [123], Figueiredo *et al.* carried out wavelet band analysis on the green component of RGB image to identify the entire image's features. Hybrid methods, such as cartoon with texture decomposition, variation, and Hessian multiscale analysis were employed on the identified traits to distinguish EXs from other yellow bruise. Their method resulted an SP value of 97% and an SE value of 90% utilizing $45,770$ fundus images.Figure 2.9 shows the result of the method. A overview of the EXs detection techniques mentioned so far is presented in Table 2.5.

2.3 DR Detection Systems

CAD systems had been employed to detect the five levels of DR. The basic objective of CAD systems in DR identification is to sort anatomic pictels from DR affected lesions. To look after this, some recent DR-based CAD tools were featured in the coming passages along with their results and draw backs.

Kaur *et al.* [126] suggested a DR diagnosis approach to pull out exudates with the help of 1307 images. The method filtered out EXs with an average accuracy of 93.46%. Bander *et al.* in [127] brought about a CAD system to subdivide OD and fovea. The authors used MESSIDOR and Kaggle datasets which together contains about $11,200$ retinal images. The OD and fovea were subdivided by applying multiscale deep learning approach yielding an accuracy of 97% and 96.7% on the MESSIDOR dataset and 96.6% and 95.6% on the Kaggle database

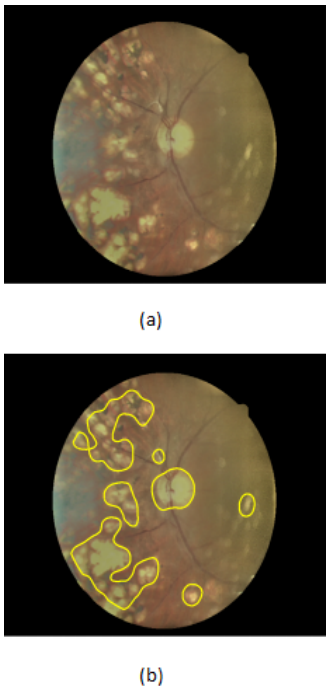

Figure 2.9: Exudates detection result [123] (a) Original image (b) Detected exudates

respectively. Gargeya *et al.* [128] as well put forward a deep learning scheme for the categorization of DR from no-DR cases. They used the MESSIDOR2 and e-OPTHA datasets and judged the color features of 75137 images. They yielded an AUC of 0.94 for MESSIDOR2 dataset and 0.95 AUC for e-OPTHA dataset. In [129] Silva *et al.* assessed 126 fundus photographs obtained from 69 patients for the early diagnosis of DR. Their algorithm resulted a kappa value of 0.1 ratio while detecting MAs and HMs characteristics. Dash *et al.* in [130] put forward a DR assessment tool based upon the extraction of blood vessels. Their method utilized DRIVE and CHASE_DB1 datasets. They reported a 0.955 accuracy for DRIVE dataset and 0.954 accuracy for CHASE_DB1 dataset.

Lenontidis in [131] revealed an automatic vessel classification system yielding an accuracy of 0.968. This method was centered on geometric vessel features. Koh *et al.* [132] considered energy and entropies to figure out normal and pathological images. The specificity and sensitivity values obtained for their method were 95.58% and 89.37%, respectively. A compendious study about the causes and computerized screening of various retinal abnormalities, such as DR, glaucoma, and cataract, in adolescent and adult population were outlined in [133]. Their summary may be helpful in turning up a novel idea for the retinopathy screening. Barua *et al.* [134] established a DR detecting tool to segment retinal vessel from HRF dataset which contains 45 images. A classification accuracy of 97% was

Table 2.5: Exudates detection methods - A recap

SI No	Author(s)	Method	Year	Data	ACC(%)
1	Liu *et al.* [108]	Morphological Matched Filter and Saliency technique with Random Forest classifier	2017	136	79%
2	Imani *et al.* [109]	Morphological component analysis. Mathematical morphology and dynamic thresholding	2016	340	AUC:0.961
3	Harangi & Hajdu [110]	Active contour model, naïve Bayes classifier	2014	83	85%
4	Zhang *et al.* [111]	Mathematical Morphology	2014	47	AUC:0.95
5	Tjandras *et al.* [112]	Mathematical Morphology&SVM Classifier	2013	-	90.54%
6	Akram *et al.* [113]	Gaussian mixture with m-mediods model	2014	1410	AUC:0.97
7	Omar *et al.* [114]	Region-based multi-scale local binary pattern texture approach	2016	130	96.73%
8	Fraz *et al.* [116]	Morphological reconstruction and Gabor Filter	2017	498	ROC:0.99
9	Prentašic, Pavle [117]	Deep CNN	2016	-	F-Score:0.78
10	García *et al.* [120]	Logistic regression&Neural network	2013	130	SE:96
11	Pereira *et al.* [122]	Ant Colony Optimization	2015	169	97%
12	Figueiredo *et al.* [123]	Wavelet Band Analysis	2015	45,770	SP:97% SE:90%

reported while classifying the image features with an ANN. In [135] Santhakumar *et al.* exhibited a machine learning approach for the screening of DR. They located EXs and HMs with an accuracy of 96% and 85% respectively using 767 images. A handful of machine learning, deep learning, and data mining schemes were briefed in [136, 137] for the extraction and catagorization of anatomical and DR lesions,

image registration, and image quality judgement. Devarakonda *et al.* [138] also employed ANN and SVM classifiers to filter characteristics for the bifurcation of normal and abnormal parts. Their method utilized 338 images acquired from a local dataset to produce an accuracy of 99%.

Vo *et al.* in [139] adopted two deep neural nets for DR screening. They utilized hybrid-color space features extracted from 91, 402 images from EyePACS and MESSIDOR databases. Their learning model achieved 0.891 AUC value in EyePACS dataset and 0.887 AUC value in MESSIDOR dataset. The deep networks presented in [140] by Lahiri *et al.* utilized the 40 images from DRIVE database. Their model detected blood vessels with a mean accuracy of 95.33%. Using the 90, 200 images obtained from EyePACS and MESSIDOR datasets Wang *et al.* in [141] extracted lesions and classified the DR severity stages employing a deep CNN. Their model recognized the severity stages of DR with AUC value of 0.865 and 0.957, for EyePACS and MESSIDOR data sources respectively. Another study [142] applied the AlexNet deep CNN to catogorize the five classes of DR. The authors of this work utilized the 35, 126 images from Kaggle datasets to result a classification accuracy of 97.93%. To extract MAs and EXs regions from color fundus photographs Lachure *et al.* in [143] applied SVM classifiers followed by morphological operations. Their method efficaciously detected MAs and EXs areas with a sensitivity of 90% and a specificity of 100%.

Nijalingappa *et al.* in [144] presented a machine learning scheme to identify EXs features employing 85 images from the DIARETDB0 and MESSIDORdata sources. At first, the green component of the RGB image was separated and sharpness enhancement techniques were carried out on this green channel image. Then image preprocessing steps were applied to this enhanced image. Finally, with the help of K-NN classifier the EXs regions were classified with an accuracy of 87% on DIARETDB0 and 95% on MESSIDOR. The CAD tool proposed by Kunwan *et al.* in [145] applied textural attributes of MAs and EXs along with SVM classifier to separate normal and DR lesions with 91% sensitivity. They utilized only 60 images acquired from the MESSIDOR dataset. A web-based method was presented in [146] for the identification of DR stages. This real time platform achieved a specificity of 91.9% and sensitivity of only 65.2% while detecting NPDR lesions.

On the other hand DR-based CAD systems in [126]-[146] primarily concentrated on the identification of DR coupled lesions and were restricted by the acuteness level of DR. The DR acuteness degree, i.e., PDR, has been considered seldom by the CAD methods. Most of them only presented an improvement in

discriminating PDR and NPDR. Furthermore, these CAD systems failed to classify the five stages of DR effectively.

2.4 Current Trends

Deep learning is an interestingly new concept to machine learning. It is employed in various range of biomedical imaging analysis and computer vision tasks, like semantic segmentation and image classification, with impressive results. Deep learning can be considered as a multi-layered top-down approach that tries to grasp high level conceptions in the data. Accelerated advancement in the processing capability of chips, e.g., graphical processing units (GPUs), reduced cost of computer hardware along with rapid improvement in the machine learning methods are the prime reasons for the admiration of deep learning [147, 148].

As of now, standard organizations such as Microsoft and Google adopt deep learning based systems to crack exciting tasks, like, object identification and classification, speech recognition, etc. The advantages of deep learning approaches are that they can extract low level attributes from data with marginal processing, they have the capability to exploit unlabeled data, they have the ability to specify relationships among attributes and they can as well master feature extraction with selective power. The learning strategy associated with deep learning systems is often adopted in a multi-layered style. It uses diverse ideas to prepare input data and transform it into suitable representations. The first layer takes out pictels from the input image. Then, these pictels are ordered into the second layer to detect edges within an image. The third layer divide these edges into tiny segments. Lastly, some further layers use these segments for recognition/classification of images. All these layers grasp features/characteristics from the input data utilizing learning algorithms devoid of human involvement [148, 149, 150, 151].

It is obvious that deep learning is a dynamic mechanism in contemporary artificial intelligence-dependent approaches. One of the recent deep learning methods, CNN, has rendered promising results in bio-medical imaging and CAD systems, e.g., retinopathy detection, brain tumor, cancer [50, 152]. The fact that DR is a high-risk disease demands early detection to manage its growth in affected persons. Computerized methods have shown to be capable in early DR analysis. However, there exist a gap considering speedy and concurrent solutions for DR identification. To fill this hole, deep learning methods have been currently applied in DR identification and have out performed clinical experts. The most pivotal

deep learning methods in DR identification are outlined in Table 2.6.

Table 2.6: Deep learning algorithms for DR identification - A recap

Method	Dataset	Result	Accuracy
[152]	KAGGLE	Detection of Diabetes	ACC:97.93%
[127]	-	Detection of fovea and OD	ACC:97%
[149]	KAGGLE	Detect Severity level of DR	AUC:0.9687
[150]	MESSIDOR	Detect Normal and DR	AUC:0.957
[153]	EyePACS	Detection of DR	-
[50]	-	Detection of Diabetes	-
[154]	-	Detection of EXs	-
[155]	-	Classify retinal disease	-
[156]	-	Detection of DR	-

The CNN- a feed forward neural network - mainly comprises convolutional, pooling, and fully connected layers. These layers are usually trained in a realistic fashion and handle distinctive roles. CNN has been proven to be efficient in the categorization of DR stages. Each layer of CNN has a group of neurons. These neurons perform a series of actions on the input data to produce centripetal areas. Output of each neuron is combined to retain overlapping among centripetal areas to suitably model the original image details. This step is carried out over all layers until required results are produced. A typical CNN pipeline is shown in Figure 2.10.

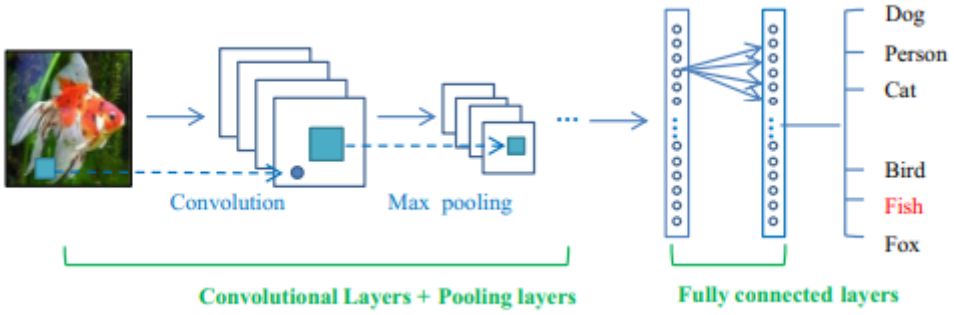

Figure 2.10: A typical CNN pipeline [147]

CNN is broadly favoured by researchers owing to its tremendous potential to utilize a shared weight modus operandi in the convolution layer to pin point each pictel utilizing a unique filter. Since CNN model can learn features by itself it requires only a small number of pre-processing steps. Human interference and preceding knowledge is not needed to develop the model during the training phase of CNN. The CNN can set forth an image in 2-D form followed by shared weights

and the correlation among neurons. The output of the convolution layer is noticed as being invariant to the object locale. CNN is found to be more algorithmically efficient than fully connected netwoks, since it employs lesser number of arguments with the identical number of hidden layers to perform multiple experimentation. Furthermore, it represent neurons in the 3-D form, viz weight, height, and depth. Usually back propagation and gradient descent approaches are employed to train CNNs and to achieve faster convergence [156]. The important shortcoming of CNNs is that it requires a huge amount of memory to keep the output of convolutional layer.

Prentasic in [117] presented a study on the uncomplicated image classifying methods employed to automatically identify DR in retinal images. These approaches only depend on pre-processing, localization, and extraction of normal and abnormal retinal feature steps to grade DR. In [157] DR screening systems were reviewed. Further, in [158] a color equalization and image segmentation scheme was employed to identify blood vessels, EXs, and MAs for DR detection.

2.5 Discussion

Digital fundus imaging is a diagnosis means for diseases like glaucoma and diabetic retinopathy. All diabetic patients demand regular check up to identify DR in the early stage itself. It is reported that yearly 50% of diabetic affected persons in the U.S. and 30% in France are asked for DR checking. As a result of this fact, the accurate check-up of candidates has become a hefty and polemical task for clinical persons. However, automated screening procedures have the capacity to accomplish quick grading of DR levels from retinal fundus images.

The survey performed in this chapter highlights the effectiveness of different deep learning, machine learning, and image processing algorithms for CAD systems to detect DR levels from fundus images. Such CAD systems were established upon the exact segmentation of DR-connected impairments like MAs, HMs, and EXs inside the fundus images.

From the developing perspective of DR-based CAD systems, a few ins and outs are emphasized here. The capability of DR-CAD methods banks on the extraction of typical DR-allied marks inside color fundus photographs, something which is liable to error and is analytically costlier. This step can force the entire system unreliable. Some other techniques have utilized obsolescent image pro-

cessing and machine learning methods devoid of quantitative data, employing an acceptable number of images. Considering DR diagnosis, many DR checking systems were drew on the recognition of DR and Non-DR classes. This in fact are unacceptable for concurrent classification of the five levels of the DR acuteness. Some CAD systems are already developed to assess the five levels of DR seriousness. However, those CAD tools were based on the domain expert intelligence to infer intra-/inter- variations of retinal characteristics. Majority of machine learning based DR-CAD systems do not consider all syndromes of DR.

The effectiveness of the existing DR-CAD systems can be reformed by taking into account of the following point. (i) cater a colossal high resolution image dataset, acquired from a different range of ethnic groups. (ii) exploit an integration of adaptive features such as hand-crafted and non-hand crafted, with dependable classifiers to achieve a much superior classification accuracy. (iii) utilize some advanced color space/appearance models to get superior description of complex image patterns (iv) beat the four stages of the DR data source problem with five DR levels and (v) detect the severity of DR in four quadrants utilizing a larger data source. Since diabetic macular edema (DME) impairs the sight of diabetic patients at a quick pace, it demands an urgent treatment and so its assessment should be examined in the future. Nowadays, ophthalmologist have added two parameters for diagnosis, i.e., diabetic retinopathy risk index (DRRI) and standard index (STARD), acquired from the pathological attributes. It is a real number and it consists of various thresholds employed to figure out the level of the disease. Hence, it can be a practical choice for physicians to apply them in the assessment of DR categorization results [159, 160].

2.5.1 Deep Learning Vs Traditional Methods.

Deep learning (DL) had yielded faithful results in healthcare and computer vision tasks. However, there exists certain significant challenges and underlying trends. Even though deep learning had confirmed to be a comprehensive solution in managing computer vision tasks, the theoretic background of DL stays unclear. For instance, how many layers should be convolution and pooling/recurrent, how many nodes per layer to achieve a particular job, and which structure is more suitable for a certain task? Human vision system is recognized as a more powerful choice than DL. So studies related with the working human brain should be integrated into DL approaches to enhance their performance. Also, the number of layers should be optimized for the extraction of high-level attributes to wangle the structure of

human brain.

The capacity of DL models largely depends on the size of the datasets. It was observed that the paucity of data source restricts and severely influence the training as well as learning accuracy of DL models. Data augmentation method and data collection employing weakly supervised learning schemes are the two common solutions to maximize the training data.

Table 2.7 shows the futuristic contrast between retinal characteristics and lesion identification techniques on identical dataset drew on hand-crafted and deep features. It is evident from Table 2.7 that the deep learning based methods are superior than the conventional methods.

Table 2.7: Comparison among retinal feature identification methods

Extracted Feature	**Method**	**Dataset**	**ACC(%)**
Optic disc	Hough transform [67]	DRIVE, DIARETDB1	99.6
	FIR filter [61]		98.95
Optic cup	CNN [75]	DRISHTI-GS, Private	94.1
	An adaptive threshold [79]		92
Blood vessel	CNN & random forest [44]	DRIVE, STARE	97.5
	Saliency & contour model [47]		97
Microaneurysms	Naïve Bayes classifier [88]	Private	99.99
	Hybrid classifiers [91]	DIARETDB0 & 1	99.4
Hemorrhage	Variation mode decomposition [107]	Private	100
	SVM [161]	STARE	97
Exudate	Morphological operations [115]	DIARETDB0 & 1	98.65
	ACO [122]	HEI-MED	97

Table 2.8 describe a performance analysis between traditional methods and deep learning methods. The Table 2.8 support the supremacy of deep learning based techniques over traditional ones in retinal characteristics extraction. These techniques are presented in [136] for MAs as well as OD extraction and localization, derived from hand-crafted traits and CNN employed methods. The methods were evaluated on identical data sources with the same statistical parameters.

Table 2.8: Comparison between traditional and deep learning methods [136]

Retinal Feature	**Approach**	**Research Study**	**Dataset**	**ACC(%)**
OD segmentation	Traditional	Morphological features	MESSIDOR	86
	Deep learning	CNN		96.40
	Traditional	Active contour	DRIVE	75.56
	Deep learning	Single state-CNN		92.68
Optic disc localization	Traditional	Morphological features	MESSIDOR	99
	Deep learning	R-CNN		99.99
	Traditional	Vessel distribution	DRIVE	100
	Deep learning	CNN		100
	Traditional	ONE-ONE minization	DIARETDB1	100
	Deep learning	CNN		98.98
Micro-aneurysms	Traditional	Ensemble method	MESSIDOR	90
	Deep learning	DCNN		95.4

Former forms of CNNs were found to be inefficient in real-time because of the demand of increased analytical resources. But now, the scenario has changed. For e.g., He *et al.* in [162] described a real-time DL structure by lowering the size of the filters and execution time. To boom the analytical capability of DL model they also introduced an adjustable activation function. Likewise, Li *et al.* [163] suggested a highly efficient CNN for pixel wise classification. The efficiency of DL can be as well increased by fixing the time intricacy and realization through GPUs.

Even though deep learning algorithms had produced better results in image and video processing fields, there exist some gaps that should be tackled for the development of more efficient DL approaches. Actually, deep learning based systems were also employed for the betterment of a computerized screening system for DR. Earlier studies mostly utilized CNN models for the screening of DR from retinal fundus images. But, the examination of these images demands intervention of ophthalmologists, which is a time consuming and is an overpriced task. Hence, DL-dependent techniques that can grasp features from a smaller dataset is necessary. Also it is crucial to address the class disparity issue for the design of DL-dependent systems in the case of learning biases for a specific class.

The design and development of DL-dependent systems in contrast to traditional methods demands the following crucial steps

1. Improving the generalisation capability of the DL networks by multiplying their size, e.g., by increasing the number of layers and nodes in each layer.

2. Providing a layer-wise feature learning scheme in the network. Every layer can learn its successive layer feature and vice versa.

3. Integrating non-hand- and hand- engineered characteristics to achieve better generalization models.

4. The current DL systems depends on shared weights to pin down their options, which is inadequate. There is a high demand for application-oriented deep networks that are independent on the available models.

Furthermore, the performance of available DL models can be improved by combining the dynamic size of deep learning structure with their outputs in the cascaded mode. This can take out the increased computational costs, demanding the training of each DL networks to independently perform their jobs. Ouyang *et al.* in [164] presented a double-stage training scheme. Here the previous stage classifiers were combined with the current stage classifier. Sun *et al.* [165] put forward a three-class CNN model for recognizing facial points. The first class CNN estimates the initial facial points. The remaining two CNN classes were utilized to revamp the initial estimates. Wang *et al.* [141] came up with a cross-breed net for object identification. The second network estimates the object coordinates from the output opf the first network.

2.6 Conclusions

This chapter accomplished a succinct review into computerized diabetic retinopathy testing methods from over 150 research publications, describing their results and limitations in the estimation of structural variations of remarkable fundus features utilizing digital fundus images. From the survey conducted it is found that complete curing of DR is impossible. To some extent photocoagulation (laser surgery) is an effective method to avoid loss of vision provided it is performed prior to disease adversely affecting the retina. Vision can be improved by vitrectomy (vitreous gel elimination through surgery) if the stern destruction of retina has not been started. In proliferative diabetic retinopathy, at times, the new blood vessel contraction process can be helped by some antivascular endothelial growth

factor medication injection or inflammatory medicine. Since diabetic retinopathy stay behind the screen giving no symptoms until it turns into the stern, early identification through regular screening is essential. For detecting and analysing diabetic retinopathy in its early stage non proliferative diabetic retinopathy is extremely critical because it embodies early signs of diabetic retinopathy. We can prevent diabetic retinopathy to cause blindness if a diabetic person is offered with consistent eye examination and treatment, if necessary.

From the literature survey conducted, it is evident that majority of work focus towards detecting blood vessels, optic disc and cup, microaneurysms, hemorrhages and exudates. This may be because these are the main indications of the early stage of diabetic retinopathy in fundus images. The current computerized diabetic retinopathy detecting approaches were found as being encouraging. But, still there exists some gaps in the identification of the acuteness level of diabetic retinopathy. From the exhaustive survey conducted, it is observed that a work which accurately detect DR and classify its severity level is lacking. Hence in this work the following objectives are set.

1. Analyse retinal fundus images
2. Detect diabetic retinopathy with 100% accuracy and
3. Identify the severity level of diabetic retinopathy using digital fundus images.

Chapter 3

Image Contrast Enhancement

3.1 Introduction

The purpose of image preprocessing is to enhance the ability to interpret the minute details available in images for human observers. An image enhancement procedure is one that gives a top notch quality image for the benefit of certain unique program that can be achieved by either removing the noisy pictels or augmenting the picture sharpness. Algorithms for enhancement of image sharpness are used to accent, smooth out or sharpen image attributes for demo and analyticity. Most of the enhancement procedures are application dependent. Often they are developed pragmatically. These procedures concentrates on specific image attributes to enrich the visual quality of an image. Broadly image enhancement methods can be categorised into 1. Spatial and 2. Transform domain procedures.

The spatial domain procedures work directly on pictels. The transform domain procedures run on the transformed image. After certain manipulations in the transformed domain an inverse transformation is carried out to get back to the spatial domain. Rudimentary enhancement methods are histogram-dependent due to their simplicity and fastness. Also they produce dependable results. The method of unsharp masking-acuminates the boundaries by deducting a part of the separated out component from the actual image- has turned into a favoured enhancement technique for diagnosis. The spatial domain method can be generally categorised into three.

1. Point operation-In this method each pixel value is altered by a function that is independent of other pixel values.

2. Mask operation- In this method each pictel is modified in proportion to the values in a tiny neighbourhood of the pixel considered.

3. Global operation- In this method all pictel values in the picture are accommodated. e.g., frequency domain operations.

In image analysis, spatial frequency indicates the changes of image brightness with respect to its position in space. If we transform an image into frequency domain and then immediately compute the corresponding inverse transform we will end up with the original image provided the said transform is perfectly reversible. Example of one of such transforms is Fourier Transform (FT). Now if we multiply the transform coefficients with a duly selected weighting factor, then we can augment certain frequencies and abate certain other frequencies. The associated changes can be visible when we take the inverse transform. This process is known as frequency domain filtering. Frequency domain filtering means multiplication of the spectrum of the image with the frequency response of the filter. Thus in summary frequency domain filtering is nothing but computing the FT of the image and the kernal, multiplying the two FTs point by point and then finding the inverse FT of the product. This demands dimensionality match between the FT of kernal and the image. Since convolution kernals are normally much smaller than the images, it is essential to zero pad the kernal to the dimension of the image to realize this process.

After the advancements in the wavelet decomposition techniques [166] wavelet transforms have been employed considerably in image enhancement applications. The development of threshold method Donoho [167] brings a feasible handling option for the nonlinear processing of wavelet coefficients. As a result the field of image contrast enhancement had advanced significantly. Other viable wavelet-dependent techniques include hard/soft thresholds and Bayesian threshold methods. Currently, different intrascale interdependence coefficient threshold schemes and a different coefficient threshold scheme under large-dimensioned space [168] have equally been evolved. As result of the continuous advancement in threshold methods, wavelet based image enhancement methods have attained better results. These techniques were backed by the fundamental wavelet theory. Also, due to the ardent R & D being performed on the scaling relationship in the transformed space the de-noising/enhancement capability of the wavelet keeps on improving.

Basically, there are two prime challenges in connection with image denoising/contrast enhancement based on wavelets.

1. selection of the wavelet coefficient's prior distribution model and

2. determination of the suitable de-noising/enhancing algorithm in relation to the distribution model

. The objective of the study being performed in wavelet de-noising is to create an exact model of non-Gaussian wavelet coefficients that are dependent to one another.

This chapter details a novel image contrast enhancement technique developed in this work. The technique enhances the image contrast using Normal Inverse Gaussian (NIG) model and fuzzified Non-Subsampled Contourlet Transform (NSCT). The NSCT is a multiscale, completely shift invariant transform that efficiently capture the geometric information in an image. Since both noise and weak edges engender lower valued coefficients in the transformed domain, normal image boosting schemes amplify weak edges as well as noises. Also when image enhancement technique is directly applied to the NSCT coefficients, it results over enhancement of the retinal image. As a solution to this problem, image enhancement method developed in this work interprets "contrast" as qualitative rather than a quantitative measure of the image. The membership values of NSCT coefficients are modified using NIG model to augment the image sharpness by retaining the pathological signs.

The contrast enhancement technique described in this chapter combines present day multiresolution, multiscale analysis to yield a novel fuzzified non-subsampled contourlet transform image contrast enhancement scheme centred on the NIG probability density function (PDF). The suggested procedure employs the NIG distribution to attain the Bayesian maximum *a posteriori* probability of the membership values of the NSCT coefficients. Since the fuzzification process used here is a linear one the membership values are also fat-tailed in behaviour. Initially, the NIG model features are dynamically calculated using a local window. The intrascale correspondance among the coefficients are modeled by this local window. Next, optimal algorithm known as OLI-Shrink [169] is employed. Since NSCT is shift invariant and redundant, the suggested technique can reliably extract orientation information about the image and satisfy human visual needs. Even though this method is a probability dependent one, it nevertheless attains best de-noising results with respect to subjective visual eccentricity and peak signal-to-noise ratio (PSNR).

The remaining part of this chapter is arranged as follows. Section 3.2 briefs the fundamentals of NSCT. Section 3.3 briefly describes the fuzzy set theory. NIG PDF is described in Section 3.4. Bayesian Estimation is briefly introduced in Section 3.5. NSCT coefficient's statistics forecasting is explained in Section 3.6. The concepts of NIG prior, maximum *a posteriori* probability, parameter esti-

mation and OLI-Shrink algorithm which are used in the suggested enhancement algorithm are also included in this section. Section 3.7 summarises the algorithm steps. Results of the algorithm is presented in Section 3.9. Conclusions are given in Section 3.10.

3.2 Non-Subsampled Contourlet Transform (NSCT)

Da Cunha *et al.* [170] put forward the so called Non-Subsampled Contourlet Transform (NSCT). Figure 3.1(a) gives an outline of the NSCT. The structure comprises of filter banks that splits the 2-D frequency plane in the subbands illustrated in Figure 3.1(b). NSCT is centred on Non-subsampled pyramid (NSP) framework and Non-subsampled directional filter banks (NSDFB), that permits it to comprehend and build a shift-invariable, multi-scale, flexible and multi-directional image decomposition that can be successfully developed by use of the *à trous* algorithm given by the convolution formula (3.1) where S represents sampling matrix, $H(z)$ is a $2-D$ filter, $y[n]$ is the output resulting from filtering $x[n]$ with $H(z^S)$.

$$y[n] = \sum_{k \epsilon supp(h)} h[k]x[n - Sk] \tag{3.1}$$

3.2.1 Non-Subsampled Pyramid (NSP)

NSP stipulates the multiscale trait of NSCT. NSP is a shift-invariant filtering structure. Similar to the Laplacian pyramid it performs a subband decomposition through two-channel non-subsampled 2-D filter banks. Figure 3.2(a) depicts the NSP decomposition (Total stages of decomposition, $J = 3$) and Figure 3.2(b) illustrates the corresponding subbands on the $2-D$ frequency plane.

The theoretical pass band of the J^{th} stage low pass filter (LPF) is extending from $[-(\pi/2^j), (\pi/2^j)]^2$.Consequently, the theoretical support of the corresponding high pass filter (HPF) is the antipodal of the LPF. i.e., $[(-\pi/2^{j-1}), (\pi/2^{j-1})]^2 \setminus [(-\pi/2^j), (\pi/2^j)]^2$. The subsequent stage filters are realized by upsampling the I^{st} stage filters. Thus multi-scale trait is introduced without designing extra filters. This architecture is thus distinct from the separable non-subsampled 2-D wavelet transform (NSWT). Here one band pass output image is created at every stage, producing $J + 1$ redundancy. Conversely, the NSWT yields 3 directional images at every level, causing a redundancy of $3J + 1$.

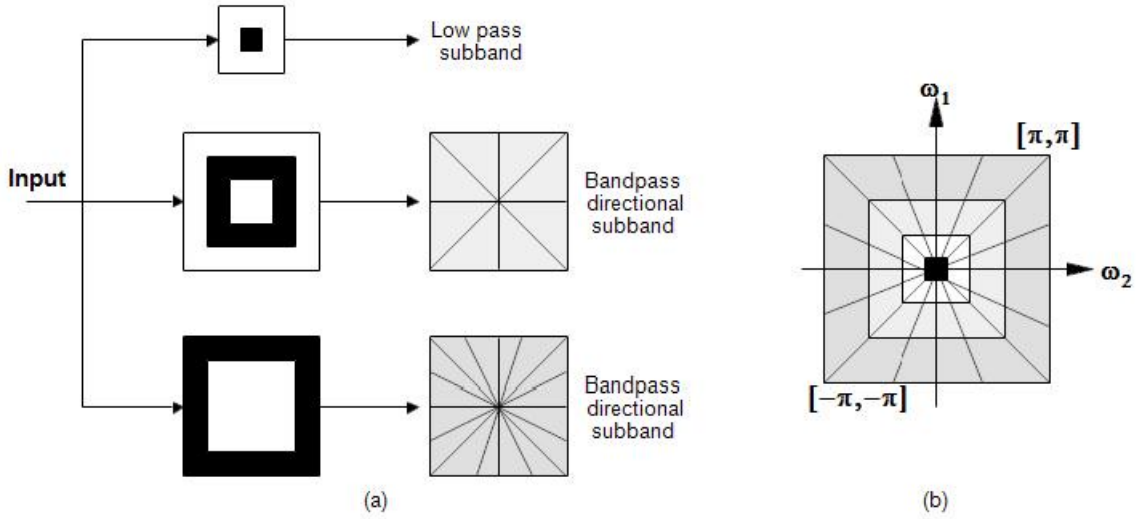

Figure 3.1: Outline of NSCT [170]

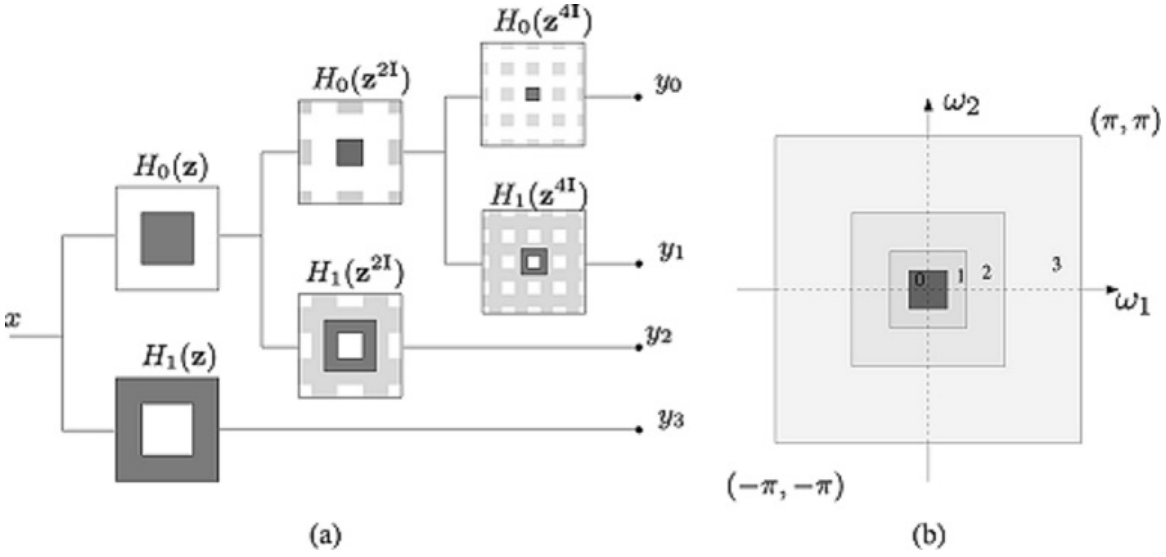

Figure 3.2: Outline of NSP [170]

The suggested $2-D$ pyramid in [171] is constructed from LPF $H_0(Z)$. Consequently $H_1(z)$ is set as $1 - H_0(z)$. Corresponding reciprocal synthesis filters are set as $G_0(z) = G_1(z) = 1$. The benefit of the NSP construction described in the previous paragraph is that it is general and consequently produce superior filters. Specifically, in this construction $G_0(z)$ is LPF and $G_1(z)$ is HPF. So they extract selected region of the noise spectrum in the refined pyramid coefficients.

3.2.2 Non-Subsampled Directional Filter Banks (NSDFB)

Bamberger and Smith [172] developed a directional filter bank. This filter bank is constructed by precisely-sampled filter banks namely, two channel fan filter banks, and exploiting re-sampling process. This produces a tree-shaped filter bank. This tree-shaped filter bank results directional wedges by separating the $2-D$ frequency space. A delay independent directional expansion is achieved by employing a non-subsampled directional filter bank (NSDFB). This NSDFB is concocted by expelling the down and up samplers in the directional filter bank (DFB). This is achieved by shutting down the down/up samplers in every tree-shaped two-channel filter bank and upsampling the filters necessarily. This produces a tree comprising two-channel non-subsampled filter banks (NSFB). Figure 3.3(a) demonstrates four channel decomposition. The upsampled fan filters $U_i(Z^Q), i = 0, 1$ in the second level possess a draft board frequency support. This fan filters together with the first level filters result the frequency decomposition in four direction as depicted in Figure 3.3(b). Likewise, the synthesis filter bank is acquired. Similar to the precisely-sampled DFB, every filter banks in the NSDFB are derived from a single NSFB comprising fan filters. In addition to this, the analytical complexity of every filter bank in the NSDFB tree and that of NSFB from which it is derived is the same. The l stage NSDFB produces 2^l directional subbands.

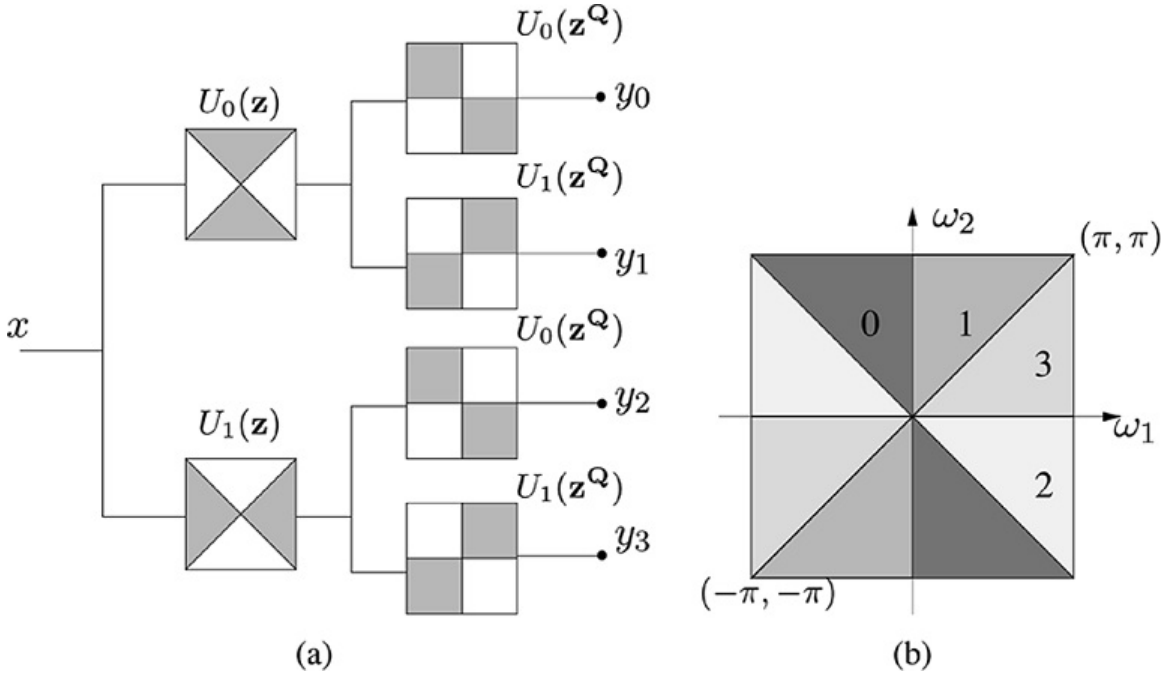

Figure 3.3: 4-Channel NSDFB (a) Filtering structure. (b) Equivalent frequency partitioning [170]

3.2.3 Combining NSP and NSDFB in the NSCT

The NSCT is developed by joining the NSP and the NSDFB as illustrated in Figure 3.4. While building the NSCT, utmost care should be exerted when employing the direction filters to the lumpier scales of the pyramid. The lower and upper frequency directional response of the NSDFB has come down with aliasing because of its tree-structured quiddity. Judiciously upsampling the filters of NSDFB is a solution to this problem. Note that while performing this upsampling the perfect reconstruction quality should be preserved.

At most care must be taken when combining the NSDFB to NSPFB. The lower and upper frequency directional response has gone down with aliasing. Due to the consequent of the tree structure nature of NSDFB the high pass channel is filtered with the bad portion of the directional filter passband. This is illustrated in Figure 3.5. This aliasing produce a significant reduction in directional resolution.

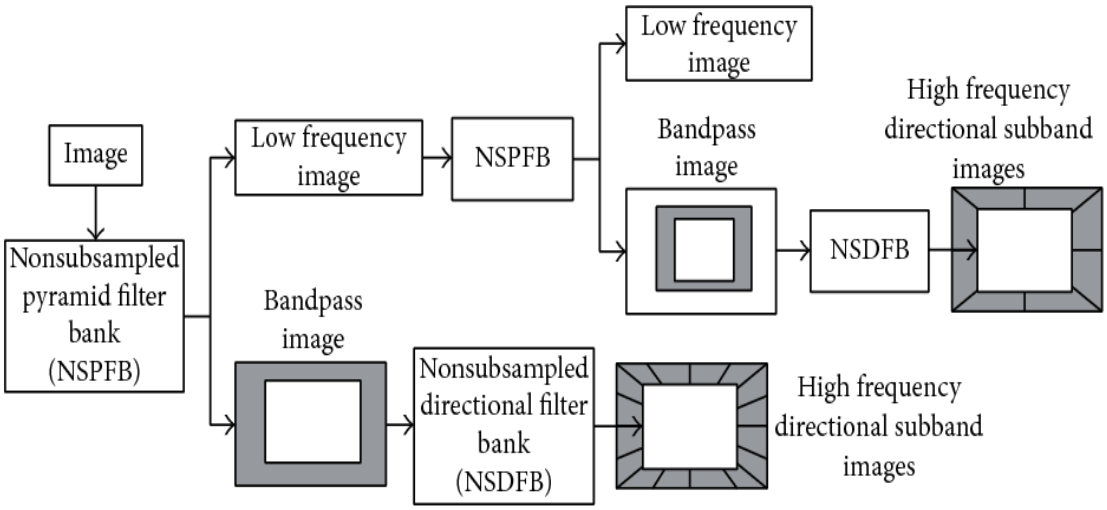

Figure 3.4: NSCT construction [173]

Introducing cautious upsampling in the filters of NSDFB this aliasing effect can be bypassed. If $U_k(\mathbf{z})$ denote the k^{th} directional filter then higher scale filters are obtained by replacing $U_k(\mathbf{z}^{2^m\mathbf{I}})$ for $U_k(\mathbf{z})$. Here m is chosen in such a way that the pyramid passband overlaps with the good part of the response. This is shown in Figure 3.6. This change also guards perfect reconstruction. Typically for five scale decomposition m is chosen as 1. So last stage NSDFB filters are upsampled by $2\mathbf{I}$.

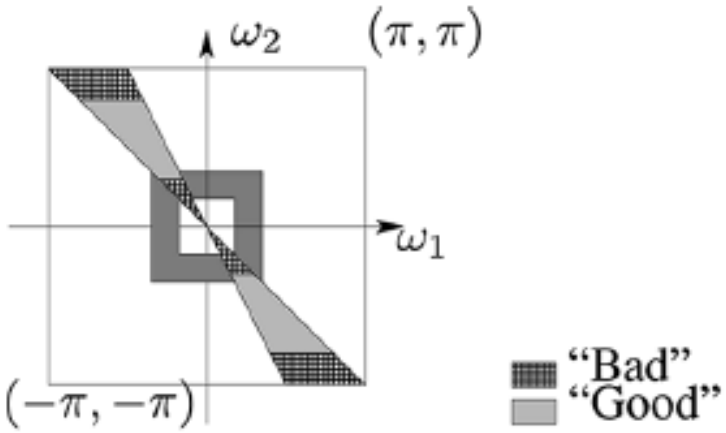

Figure 3.5: Aliasing with no upsampling

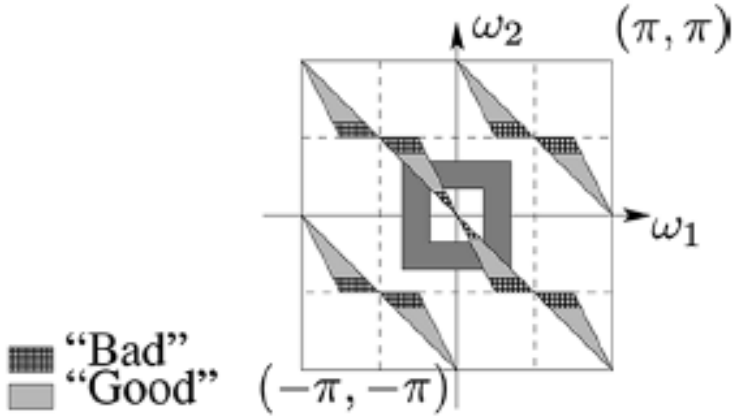

Figure 3.6: No aliasing with upsampling

Use of upsampled filters does not add analytical complexity. Hence, every filter in the NSDFB tree and the constituent fan NSFB has the same computational complexity. Similarly, complexity of each stage filtering of the NSP and that of the first stage are the same. Hence, the computational complexity of NSCT is determined by the elementary fan NSFB complexity. In summary, let us assume that each NSFB in NSP and NSDFB needs L number of operations per output sample, and NSCT requires B number of subbands then for an image containing N pixels NSCT takes about B$*$ N $*$ L operations.

The necessary and sufficient condition for the NSCT to be invertible is that both the 2-channel building block NSFBs present in the NSP and NSDFB must be invertible. Also the flexibility of NSCT permits enough number of 2^l directions in each scale. Conclusively, it can satiate the anisotropic scaling law. This character-

istic is guaranteed by increasing the number of directions in the NSDFB expansion by two fold at each alternate scale. The NSCT having I_j number of levels in the j^{th} scale of NSDFB possesses $1 + \sum_{j=1}^{J} 2^{I_j}$.

3.3 Fuzzy Set Theory

Fuzzy set theory is put forward by L.A. Zadeh. A fuzzy set is an ordered pair comprising of elements and their corresponding membership function that assigns a membership value to each element [174]. A fuzzy set can be mathematically represented by (3.2).

$$A = \{(z, m_A(z)) \,|z \epsilon Z\} \tag{3.2}$$

where Z is the universe of discourse and $m_A(z)$ is the membership value of element z in the fuzzy set A and z can take a value in the interval $[0, 1]$. Let $I(p, q)\,|p, q \,\epsilon\, \mathbb{N}^2$ be an $M \times N$ digital image with 0 to $L-1$ gray levels. Image I can be considered as a bunch of fuzzy singletones. The members of this set is the membership value $m_I(g_{pq})$ of the gray level g_{pq}, belonging to the $(p, q)^{th}$ pixel, relating to an image property such as homogeneity, edginess, brightness, etc. For image enhancement usually the brightness property is considered. In terms of the fuzzy set notation, an image I can be represented (3.3).

$$I = \left\{ \frac{m_I(g_{pq})}{g_{pq}} \Big| p = 0, 1, ...M-1, q = 0, 1, ...N \right\} \tag{3.3}$$

Fuzzy image enhancement consists of three sequential steps

1. Obtain the membership values using (3.15)
2. Modification of membership values using a threshold
   (a) Enhance the membership values of dark and bright pixels.
   (b) Retain the membership values of gray pixels as such.
3. Use this modified membership values to reconstruct the image.

3.4 Normal Inverse Gaussian Distribution

The key attributes of the image statistics in the NSCT domain can be enumerated as follows.

(i) High kurtosis (ii) Heavy tails (iii) They are non-Gaussian and (iv) Sharp central peak. These attributes are anticipated since most of the time images mainly

encompass homogeneous areas with some key characteristics like edges. The coefficients corresponding to these homogeneous regions are close to zero while that corresponding to edges are large valued. As quoted earlier, the key concern in the contrast enhancement problem is the selection of a threshold value which classify the image pixels into dark, gray, and bright pixels. The NIG model derived by Barndroff-Nielsen [175] is utilized to describe the distribution of membership values of NSCT coefficients. In [175] the inverse Gaussian PDF is employed in the role of mixing distribution. The limitations of the traditional models can be solved by the hybrid model. Due to the flexibility offered during the parameter selection, the hybrid model can represent curves of different shapes. Hence, NIG model is chosen.

The probability density function can be expressed as (3.4)

$$f_x(x) = \frac{\alpha\delta}{\pi q(x)}.\exp\left[p(x)\right].K_1\left[\alpha q(x)\right] \tag{3.4}$$

where $q(x) = \sqrt{\delta^2 + (x^2 - \mu^2)}$, $p(x) = \delta\sqrt{\alpha^2 - \beta^2} + \beta(x - \mu)$ and $K_1(.)$ is the modified Bessel function of the second kind with index one. The attributes $(\alpha, \beta, \mu, \delta)$ determines the distribution of NIG. There exists a greater flexibility in selecting the values of these four parameters. This makes the PDF of NIG an appropriate model for different kurtotic, uni-modal, positive data. The feature factor α decides the steepness of density, a lesser value of α shows a slower rate of decay with heavier tails. β is the skewness factor; $\beta < 0$ indicates left skewed density, $\beta = 0$ indicate symmetric density and $\beta > 0$ indicates right skewed density around the translation parameter μ. The parameter δ is scale-like.

The associated decomposition coefficients of images are normally symmetrical distributions and hence the membership values also. So it is assumed that $\beta = \mu = 0$. Hence the corresponding PDF of NIG can be described as (3.5)

$$f_x(x) = \frac{\alpha\delta\,\exp(\alpha\delta)}{\pi}\frac{K_1\left(\alpha\sqrt{x^2 + \delta^2}\right)}{\sqrt{x^2 + \delta^2}} \tag{3.5}$$

3.5 Bayesian Estimation

Nowadays, the Bayes method has developed as a subject of debate in the area of image enhancement. Using Bayesian theory it predicts the original image by setting up a prior probability distribution modal for the boundary coefficients. The key to success of the flexible Bayes algorithm is the fact that it can exactly model the prior marginal distribution of coefficients quickly.

Suppose an original image X has been modified by additive white Gaussian noise N

$$B = X + N \tag{3.6}$$

where B is the noisy image. De-noising strives to get back X as exactly as attainable. Due to the NSCT transformation of the noisy image, the decomposition coefficients are

$$b = x + n \tag{3.7}$$

where b, x, and n are the NSCT coefficients of the noisy image, original noise-free image and noise respectively. The objective of Bayesian denoising is to find the estimation of x, i.e.$\hat{x}(b)$. (3.8) denotes Bayesian maximum *a posteriori* estimation

$$\hat{x}(b) = \arg\max_{a} \left\{ f_{x|b}(x|b) \right\} \tag{3.8}$$

where $f_{x|b}(x|b)$ is the conditional density of the observation b given x. $\hat{x}(b)$ can be found utilizing Bayesian rule (3.9).

$$\begin{aligned} \hat{x}(b) &= \arg\max_{x} \left\{ f_{x|b}(x|b) \right\} \\ &= \arg\max_{x} \left\{ f_{b|x}(b|x) . f_x(x) \right\} \\ &= \arg\max_{x} \left\{ f_n(b-x) . f_x(x) \right\} \end{aligned} \tag{3.9}$$

(3.9) gives us the freedom to express this estimation in relation to the probability distribution of noise coefficients $f_n(.)$ and the prior distribution of the noise-free image coefficient $f_x(.)$.

As per the hypothesis on the noise, $f_n(.)$ is a zero-mean Gaussian function with variance σ_n^2. So

$$f_n(n) = \frac{1}{\sqrt{2\pi}\sigma_n} . \exp\left(\frac{-n^2}{2\sigma_n^2} \right) \tag{3.10}$$

Using (3.10) to solve (3.9) and applying a logarithm on the independent variable, (3.9) can be expressed as

$$\hat{x}(b) = \arg\max_{x} \left[\frac{-(b-x)^2}{2\sigma_n^2} + \zeta(x) \right] \tag{3.11}$$

where $\zeta(x) = ln(f_x(x))$ is a differentiable convex function. Assuming $\frac{-(b-x)^2}{2\sigma_n^2} +$

$\zeta(x) = 0$, then $\hat{x}(b)$ can be calculated to attain the maximum *a posteriori*. So

$$\frac{b - \hat{x}}{\sigma_n^2} + \zeta^{'}(x) = 0 \tag{3.12}$$

Since $\zeta^{'}(x)$ is discontinuous as well as singular in region close to zero and the symbol $\hat{x}(b)$ is different from b, (3.12) cannot be solved in closed form. In [176] Bhuiyan *et al.*, put forward a solution as given in (3.13).

$$\hat{x}(b) = \text{sign}(b) .\max\left(|b| - \sigma_n^2 B_1, 0\right) \tag{3.13}$$

where

$$B_1 = \left| \frac{2b}{\delta^2 + b^2} + \frac{\alpha b}{\sqrt{\delta^2 + b^2}} . \frac{K_0\left(\alpha\sqrt{\delta^2 + b^2}\right)}{K_1\left(\alpha\sqrt{\delta^2 + b^2}\right)} \right| \tag{3.14}$$

(3.13) is adaptive to every subband. So it can adaptively filter noise from all subbands. $\sigma_n^2 B_1$ is the threshold value, λ. It can be altered with respect to the values of the coefficients. The noise coefficients are larger and possess a larger threshold value. The signal coefficient is also high valued but with lower threshold value.

3.6 Marginal Statistical Modelling of the Membership Values of the NSCT Subband Coefficients

The characteristics of NSCT such as anisotropy, high degree of directionality, and shift invariance makes it perfect choice to successfully acquire geometrical and directional details of the image. NSCT coefficients can be altered to enhance the boundaries in an image, thereby improving the image sharpness. Since the attribute contrast is interpreted as a qualitative measure as opposed to a quantitative attribute of the image, fuzzy membership values of the NSCT coefficients are found out by using (3.15) where $C_{j,l}^J(p,q)$ is the NSCT coefficient corresponding to the $(p,q)^{th}$ pixel in the j^{th} scale and on the l^{th} direction and $C_{(j,l)(min)}^J$ and $C_{(j,l)(max)}^J$ are the minimum and maximum values of NSCT coefficients in the j^{th} scale and on the l^{th} direction subband. Here onwards for convenience $C_{j,l}^J(p,q)$ will be represented as b, $C_{(j,l)(min)}^J$ and $C_{(j,l)(max)}^J$ as b_{min} and b_{max} respectively.

$$m_{j,l}^J(p,q) = \frac{C_{j,l}^J(p,q) - C_{(j,l)(min)}^J}{C_{(j,l)(max)}^J - C_{(j,l)(min)}^J} \tag{3.15}$$

The NSCT coefficients corresponding to smooth region of the image are near to zero and those corresponding to boundaries/edges are bigger in magnitude. Thus as in the case of NSCT coefficients, these membership values of NSCT coefficients show relatively high non-Gaussian features such as heavy tail, sharp central peak and high kurtosis. Figure 3.7 shows the histogram distribution of the third layer subband of NSCT coefficients in the first direction. As evident from Figure 3.7 the NIG PDF can accurately model the coefficient distribution. The distribution shows a sharp peak adjacent to zero and long tails to both ways of the peak, which better tightly fit the histogram of the coefficient. Also it fits the degree of coefficient distribution on other subbands as well. The membership values of the NSCT coefficients are obtained by using (3.15) so that the statistical properties of the NSCT coefficients are preserved in the fuzzified domain also.

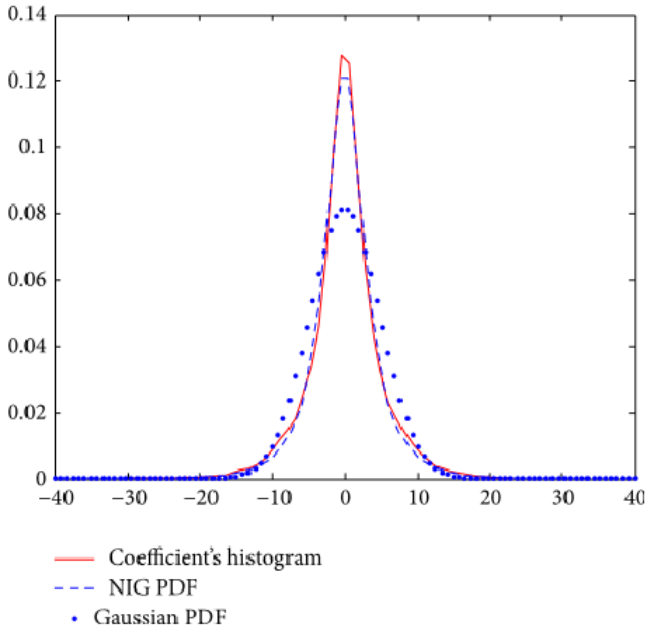

Figure 3.7: Probability density of the NSCT coefficients and the NIG PDF and Gaussian PDF fitted to this density [173]

For easy pick of parameters, the NIG distribution can exactly embodiment the data with various tails [177]. In this work NIG distribution is employed to fit NSCT coefficient's marginal statistical distribution. As illustrated in Figure 3.7 the coefficient distribution particularly, the heavy tail, can be exactly modelled through NIG PDF.

3.6.1 Estimation of Parameters

The parameters utilized to enhance the contrast can be obtained by considering the actual distribution of various subband coefficients. These parameters are effective in obtaining various degrees of threshold processing for various noise levels.

Let $\hat{k_1}, \hat{k_2}, \hat{k_3}$, *and* $\hat{k_4}$ describe the one to four order cumulants of the noise affected image coefficients accordingly. Therefore, the skewness γ_3 is given by (3.16) and the kurtosis γ_4 is given by (3.17)

$$\gamma_3 = \hat{k_3} \Big/ \left(\hat{k_2}\right)^{3/2} \tag{3.16}$$

$$\gamma_4 = \hat{k_4} \Big/ \left(\hat{k_2}\right)^{2} \tag{3.17}$$

Now the parameters δ and α can be calculated utilizing (3.18) and (3.19) respectively

$$\delta = \sqrt{\xi . \hat{k_2} \left(1 - \rho^2\right)} \tag{3.18}$$

$$\alpha = \frac{\xi}{\delta \left(1 - \rho^2\right)} \tag{3.19}$$

where $\xi = 3. \left(\gamma_4 - \frac{4\gamma_3^2}{3}\right)^{-1}$ and $\rho = \gamma_3 \sqrt{\xi}/3$

$\hat{k_1}, \hat{k_2}, \hat{k_3}$, *and* $\hat{k_4}$ vary from subband to subband [173]. Since the parameters γ_3, γ_4, δ, α, ξ, and ρ are calculated from $\hat{k_1}, \hat{k_2}, \hat{k_3}$, *and* $\hat{k_4}$ their values also vary from subband to subband. So, for different subbands our algorithm will dynamically calculate the parameter values.

3.6.2 Thresholding Method

Using optimum linear interpolation between coefficients and their corresponding subband mean Fathi and Naghsh-Nilchi [169] put forward OLI-shrink algorithm. According to this algorithm modified membership value $\bar{m}_{j,l}^{J}(p,q)$ can be obtained by using (3.20).

$$\bar{m}_{j,l}^{J}(p,q) = \begin{cases} 0 & if\ |b| \leq \lambda \\ \min\left((m_{j,l}^{J}(p,q) - \eta_m(m_{j,l}^{J}(p,q) - \mu_m)), 1\right) & if\ |b| > \lambda \end{cases} \tag{3.20}$$

where μ_m is the mean of the membership values of the NSCT coefficients b of the corresponding subband and η_m can be obtained using Equation $\eta_m = \frac{\sigma_{nm}^2}{\sigma_m^2}$ where σ_m^2 is the variance of membership values in the corresponding subband. The algorithm to find parameter σ_{nm}^2 is given below.

1: Accomplish the orthogonal wavelet transform on the image and find out the noise standard deviation, $\hat{\sigma}_n$, by employing the robust median estimator on the HH1 subband's coefficients ($Y_{i,j}^{HH1}$) as outlined by Donoho [167].

$$\hat{\sigma}_n = \frac{median\left(|\, Y_{i,j}^{HH1}|\right)}{0.6745} \tag{3.21}$$

2: Construct a white Gaussian noise image of size same as that of the original image and with zero mean and variance $\hat{\sigma}_n^2$.
3: Accomplish NSCT transformation on the noisy image.
4: Find the membership values of these NSCT coefficients of noisy image using (3.15).
5: Obtain the variance $\hat{\sigma}_{nm}^2(k)$ of membership values corresponding to each high frequency subband.
6: Go to step 2 and repeat the above steps 5 times. The final coefficient variance σ_{nm}^2 is obtained by averaging the $\hat{\sigma}_{nm}^2(k)s$ obtained.

The threshold value λ is obtained by (3.22)

$$\lambda = \sigma_n^2 B_1 \tag{3.22}$$

where σ_n is obtained in a similar way as explained above to find σ_{nm}^2. But here step 4 is not performed and so variance of the NSCT coefficients are calculated.

Different directional subbands in NSCT shows different noise variance because of the nonorthogonal nature of NSCT [170]. Also, λ depends on parameter B_1 whose value is different for different NSCT coefficients. Hence, the λ value is dynamically calculated for different NSCT coefficiens in different directional subbands. After modifying the membership values using (3.20), an inverse transform is carried using (3.23) to obtain modified NSCT coefficients.

$$\bar{C}_{j,l}^J(p,q) = \bar{m}_{j,l}^J(p,q)\left[C_{(j,l)_{max}}^J - C_{j,l}^J(p,q)\right] + C_{(j,l)_{min}}^J \tag{3.23}$$

Using modified NSCT coefficients reconstruct the enhanced image.

3.7 Image Contrast Enhancement Using NSCT

This Section summarises the proposed image contrast improvement method adopted in this work and is pictorially represented in Figure 3.8.

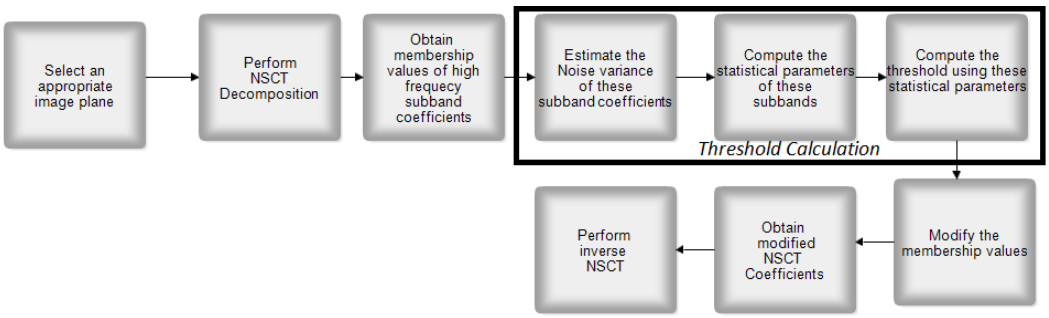

Figure 3.8: Process flow of proposed enhancement method

The green channel image of the original RGB retinal image is chosen to apply the proposed algorithm. The reason for choosing the green channel is that it gives maximum contrast with the image background. The blue channel tends to be empty and the red channel tends to be saturated. If we employ the contrast enhancement algorithm directly to the NSCT coefficients, it may destroy some of the wanted information in the retinal image. As a solution to this issue, an image enhancement algorithm employing fuzzy set theory is utilized here. In this procedure, the membership values of NSCT coefficients are found using (3.15). Then these membership values are modified using probability theory discussed above using E(3.20). As per these modified membership values the NSCT coefficients are modified using (3.23). Finally, inverse NSCT is calculated using these modified coefficients. Since the image brightness is considered as a qualitative rather than quantitative attribute, this enhancement scheme improves the image contrast without affecting the pathological features present in the image.

Another prime concern in threshold enhancing is choosing the value for the threshold. A comparatively small value of threshold may preserve detailed information about the image. But, this may retain noise also. On the other hand, a larger threshold may spoil the high-frequency data of the image. This may cause an erroneous Gibbs phenomenon in the enhanced image. The threshold selection problem is solved by using a Normal Inverse Gaussian model dependent scheme which utilizes the Bayesian probability to perform image enhancement in the fuzzified NSCT domain. First, the NIG model is employed to demonstrate the distributions of the fuzzy membership values of the NSCT coefficients. Then with the help of the theory of Bayesian maximum *a posteriori* probability a threshold

function is obtained. Lastly, to ensure a gentle thresholding OLI-Shrink algorithm given by (3.20) is utilized.

To detect the fundus region the thresholding method proposed by Otsu [178] is applied. Followed by this operation, a morphological closing operation is performed to eliminate unwanted tiny objects left inside the fundus region. Application of NIG model based contrast enhancement in the fuzzified NSCT domain causes some widgets outside the fundus area. This widgets produces false edges during the edge detection phase. The mask that indicate the fundus region aids to remove these widgets and it can also reduce the running time of the algorithm, as our region of interest is now the area inside the fundus region instead of the whole image for applying subsequent algorithm steps.

3.7.1 Enhancement Algorithm

Consequently, the suggested algorithm to augment the retinal image comprises the following steps:

1: Accomplish NSCT decomposition to yield NSCT coefficients.
2: Find out the membership values of each subband coefficients in the fuzzy set contrast using the (3.15)
3: Assess the noise variance of each subband coefficient by employing Monte-Carlo method.
4: For each subband in each level estimate the threshold value and statistical parameters of the coefficients as follows:

(i) the terms δ and α using (3.18) and (3.19) respectively

(ii) the threshold value λ using (3.22)

(iii) the mean μ and variance σ_b^2 of each high frequency subbands.

(iv) the term η using (3.24).

$$\eta \cong \frac{\sigma_n^2}{\sigma_b^2}. \tag{3.24}$$

5: Modify the membership values of all subbands using (3.20)
6: Perform defuzzification using (3.23) to obtain modified NSCT coefficients
7: Perform the inverse NSCT to get back the enhanced image.

3.8 Database

The algorithm summarized in Section 3.7.1 is applied to both DRIVE and HRF image database.

3.8.1 DRIVE Database

The DRIVE database contains 40 colour images of retina with 768×584 pixels and 8 bits per colour channel represented in LZW compressed TIFF format. These images were oroginally captured using cannon CR5 nonmydriatic 3 charge coupled device camera at 45^0 field of view (FOV) and were initially saved in JPEG format. The database also includes masks with the delimitation of FOV of approximately 540 pixels in diameter for each image and binary images with the results of manual segmentation. These binary images have already been used as ground truth for performance evaluation of several vessel segmentation methods. The 40 images were divided into a training set and a test set. For the images of the test set a second independent manual segmentation exists as well.

3.8.2 HRF Image Database

The HRF database was established by a collaborative research group consisting of two European institutions: Brno University of Technology, Faculty of Electrical Engineering and Communication, Department of Biomedical Engineering, Brno, Czech Republic and Pattern Recognition Lab at the University of Erlangen-Nuremberg, Germany. The database can be downloaded from the public website: http://www5.informatik.uni-erlangen.de/research/data/fundus-images'. This database contains three sets of fundus images. The first one is composed of images of 15 healthy patients without any retinal pathology. the second set consists of 15 retinal images of patients with DR and the last one includes 15 images of patients with glaucoma. Thus the second and third group allow evaluation of the algorithm in the case of pathological retinas.

Mydriatic fundus camera CANNON CF-60 UV: equipped with CANNON EOS-20D digital camera with a 60-degree FOV is used to acquire all fundus iamges. The image size is 3504×2336 pixels. All images are stored in JPEG format with low compression rates and 24 bits per pixels (True colour). Also a binary mask determining the FOV is provided for each image. Manual segmentation of the images were done by three experts independently and manual labeling of the images were performed using ADOBE photoshop CS4 image editor.

3.9 Results

MATLAB version R2013b is used to implement the proposed method. The method described above enhances all weak edges in the image which includes edges of thin vessels as well as the weak edges arising from uneven background illumination. Figure 3.9 shows the images before applying the proposed enhancement algorithm and image after applying the proposed enhancement algorithm. From the figure it is clear that the NSCT is well adapted to represent the image containing edges. Hence, it is a good candidate for edge enhancement. Since NSCT coefficients are modified based on their membership values it improves the edges in the image which inturn improves the image contrast. The non linear function used to modify the membership values of the NSCT coefficients helps to retain the minute edge details in the image. The selection of parameters based on the statistical features of the NSCT coefficients and the noise standard deviation helps to calculate appropriate threshold value λ for NSCT each coefficients at different directional subbands dynamically. It is also clear from Figure 3.9 that even though the algorithm improves the image contrast, due to the use of fundus mask the algorithm is not boosting the artifacts/edges outside of the fundus region.

3.9.1 Evaluation

3.9.1.1 Enhancement Assessment

Several methods are available in the literature to assess the image contrast improvement. They fall into two classes. 1. Objective and 2. Subjective. One of the objective measures is Peak Signal to Noise Ratio (PSNR). PSNR evaluates the intensity changes between the original and the enhanced image. Mean Square Error (MSE) and PSNR can be computed using (3.25) and (3.26) respectively.

$$MSE = \frac{1}{mn}\sum_{i=1}^{m}\sum_{j=1}^{n}\|I_0(i,j) - I_e(i,j)\|^2 \tag{3.25}$$

where I_0 and I_e are the green channel and enhanced images respectively.

$$PSNR = 10log_{10}\left(\frac{255^2}{MSE}\right) \tag{3.26}$$

Another objective method to evaluate contrast enhancement is contrast improvement index (CII) [179] that can be defined by (3.27).

$$CII = \frac{C_{en}}{C_{ori}} \tag{3.27}$$

where C_{en} and C_{ori} are the contrast for the enhanced and original images, respectively. The image contrast can be given by (3.28)

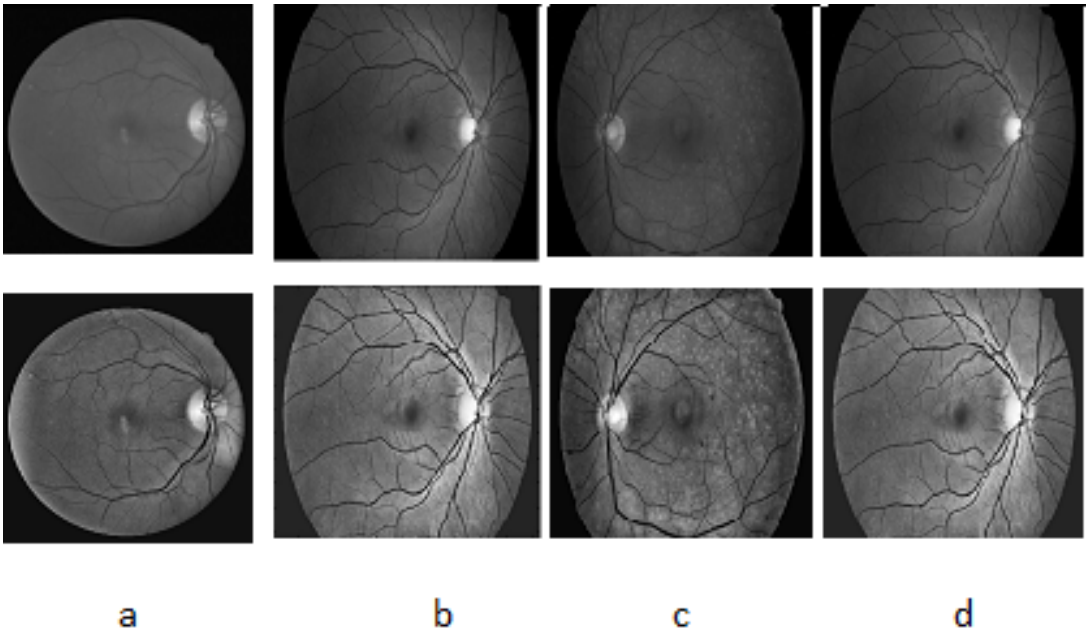

Figure 3.9: Result of proposed enhancement method. (a) Result of proposed method to image 25 of DRIVE database. (b)-(d) Result of proposed method to image 01_h, 01_dr, 01_g of HRF database, respectively. From top to bottom they are the green channel and contrast enhanced image.

$$C = \frac{r—b}{r+b} \tag{3.28}$$

where b and r are the average gray level value of the background and foreground, respectively.

Image Enhancement Metric (IEM) described by (3.29) is also used to evaluate the performance of the proposed contrast enhancement method

$$IEM = \frac{\sum_{m=1}^{k_1}\sum_{l=1}^{k_2}\sum_{n=1}^{8}|I_{e,c}^{l,m} - I_{e,n}^{l,m}|}{\sum_{m=1}^{k_1}\sum_{l=1}^{k_2}\sum_{n=1}^{8}|I_{r,c}^{l,m} - I_{r,n}^{l,m}|} \tag{3.29}$$

Here images are divided into $k_1 k_2$ blocks of size 3×3 and $I_{e,c}^{l,m}$, $I_{r,c}^{l,m}$ are the central pixel intensity in the (l, m) block of the enhanced and reference images respectively. $I_n^{l,m}$, $n = 1, 2, ...8$ is the 8-neighbors of the center pixel [180]. When the image is enhanced $IEM > 1$. Whereas $IEM < 1$ there is deterioration. $IEM = 1$ indicates neither improvement nor deterioration of image. Higher the value of IEM, better the improvement in image contrast and sharpness.

The result of assessment of proposed algorithm using the above mentioned measures is shown in Tables 3.1 and 3.2. Small values of standard deviation of the PSNR, CII, and IEM indicate good robustness of the method.

Table 3.1: Quantitative assessment of proposed contrast enhancement method on DRIVE fatabase

DRIVE Database		
Measure	Average	STD
PSNR (in dB)	34.68	1.13
CII	1.36	0.004
IEM	1.7186	0.109

Table 3.2: Quantitative assessment of proposed contrast enhancement method on HRF database

HRF Database						
	Healthy		DR affected		Glaucoma affected	
Measure	Average	STD	Average	STD	Average	STD
PSNR (in dB)	32.41	1.14	29.16	1.19	31.72	1.16
CII	1.28	0.012	1.27	0.037	1.27	0.016
IEM	1.67	0.112	1.61	0.136	1.66	0.118

In visual subjective measures, help from human observers (such as opthalmologist) are taken. They comment on edge details, presence of artifacts in the enhanced image, similarity between the enhanced image and the original image.

The contrast enhancement technique discussed in this chapter is specifically meant for improving the retinal image contrast while detecting DR. This method enhances the retinal image contrast without removing the noise present in the image. The method is devised so because if de-noising is done, it may also affect/remove the pathological symptoms (especially MAs) present in the images. This will affect the detection and classification stages. But other contrast enhancement methods available in the literature performs de-noising of the images also.

3.10 Conclusion

In this chapter, a novel image contrast enhancement technique derived from Bayesian frame work is discussed. It exactly assess the NSCT coefficient's distribution model by using the prime attributes of the Bayesian de-noising. The proposed technique

utilized a de-noising algorithm depending on the NIG prior model of NSCT. The parameters of the NIG prior model can be choosen flexibly and varied adaptively. The NSCT coefficients have pointed peak at zero and symmetrically distributed heavy-tailed characteristics on both sides. The NIG prior model can exactly describe these characteristics. Hence, Bayesian de-noising can be utilized to successfully enhance the image contrast by modifying the fuzzy membership values of the NSCT coefficients and reconstructing the image based on this modified membership values. The quantitative and visual assessments establishes the fact that it can accomplish remarkably superior results than the modern image enhancement methods.

Chapter 4

Extraction of Normal Retinal Components

4.1 Introduction

The three fundamental structures of our retina are vessel, optic disc, and fovea. These structures are widely employed for a number of applications including abnormality identification within the retina, registration of retinal images, as well as brightness adjustment inside the retinal images. Manual extraction of these crucial structures is time consuming. Also it fully depends on the competency of the person.

This chapter proposes techniques for extracting and localizing normal retinal features like blood vessels, optic disc and fovea. Before applying this technique, the image enhancement technique described in Chapter 3 is applied to retinal images. For extraction of blood vessels green component of the RGB retinal image is utilized whereas for localization of OD and fovea the luma component of retinal image is used.

Contemporary researches in the area of medical imaging have proved that quantitative assessment of microvasculature of retina can foresee various abnormalities/diseases. Digital fundus imaging in optometry plays a key part in medical diagnosis of elementary levels of blood pressure and diabetes as well as cardiovascular disease. A few of the important clinical goals recorded in the literature for retinal blood vessel extraction are the assessment of the retinopathy of prematurity, identification of arteriolar narrowing, detection of hypertension by measuring the diameter of vessels, measurement of cardiovascular abnormalities, identification of macular avascular areas, realization of DR screening programs and computerized

laser surgery.

Other ancillary applications include automatic development of retinal maps, which can be utilized for the therapy of age-dependent macular deterioration, synthesis of retinal image mosaic, filtering out retinal vasculature properties for multimodal or temporal image registration, localization of the optic disc and fovea. Moreover, the retinal vessel network is unique to every individual. So it can be employed for biometric identification.

Extracting blood vessels from fundus images can be challenging due to numerous reasons. A few of the causes that produce error are linked with the type of imagery and its acquisition method as well as the intrinsic attributes of retinal images. The two paramount factors that adversely affects the blood vessel extraction process are the inappropriate image contrast and the irregular illumination of the background. The acquisition process results uneven illumination. The unacceptable contrast is due to the acquisition process and on the grounds that various vessels have different sharpness with respect to background. Specifically, veins have lower sharpness than arteries. Thin vessels also show a lower sharpness with respect to the background than do thick vessels. Furthermore, impact of pathological variations and lesions, presence of optical disc, fovea, and noise as well as vessels with different widths are the other facts to be taken care of. Therefore, an automatic algorithm that segment retinal blood vessels quickly and with greater accuracy is the desire of researchers.

Discernment of the optic disc (OD) and fovea locale in retinal fundus images (RFIs) is one of the key concerns of the computerized detection of retinal abnormalities. The OD and fovea as well as the retinal vasculature are the most pivotal anatomical areas on the rearward of the retina. The OD is the departure place of the optic nerve system. The retinal vasculature ingresses and egresses the eye through OD. The dynamics of the OD is dissimilar from that of the abutting retinal areas, as shown in Figure 4.1. Areas of the OD can effectively be categorized as abnormal and normal by abnormality identification procedures. Identifying and masking the OD is the important inspiration behind this work. Instances of aberrations that can be judged incorrectly with OD are drusens, exudates and cotton-wool spots. Furthermore, the OD locale is beneficial in the computerized screening of glaucoma. It also plays a major role in the identification of neovascularizations on the OD, a very limited but acute disorder. The fovea is situated in the middle of a darker area in RFIs. It is the source of sharp central vision. Due to its crucial role in vision, the distance of the lesions from fovea affects their

clinical significance. i.e lesions that are very close to fovea affects vision seriously and that are away from it less affects the vision.

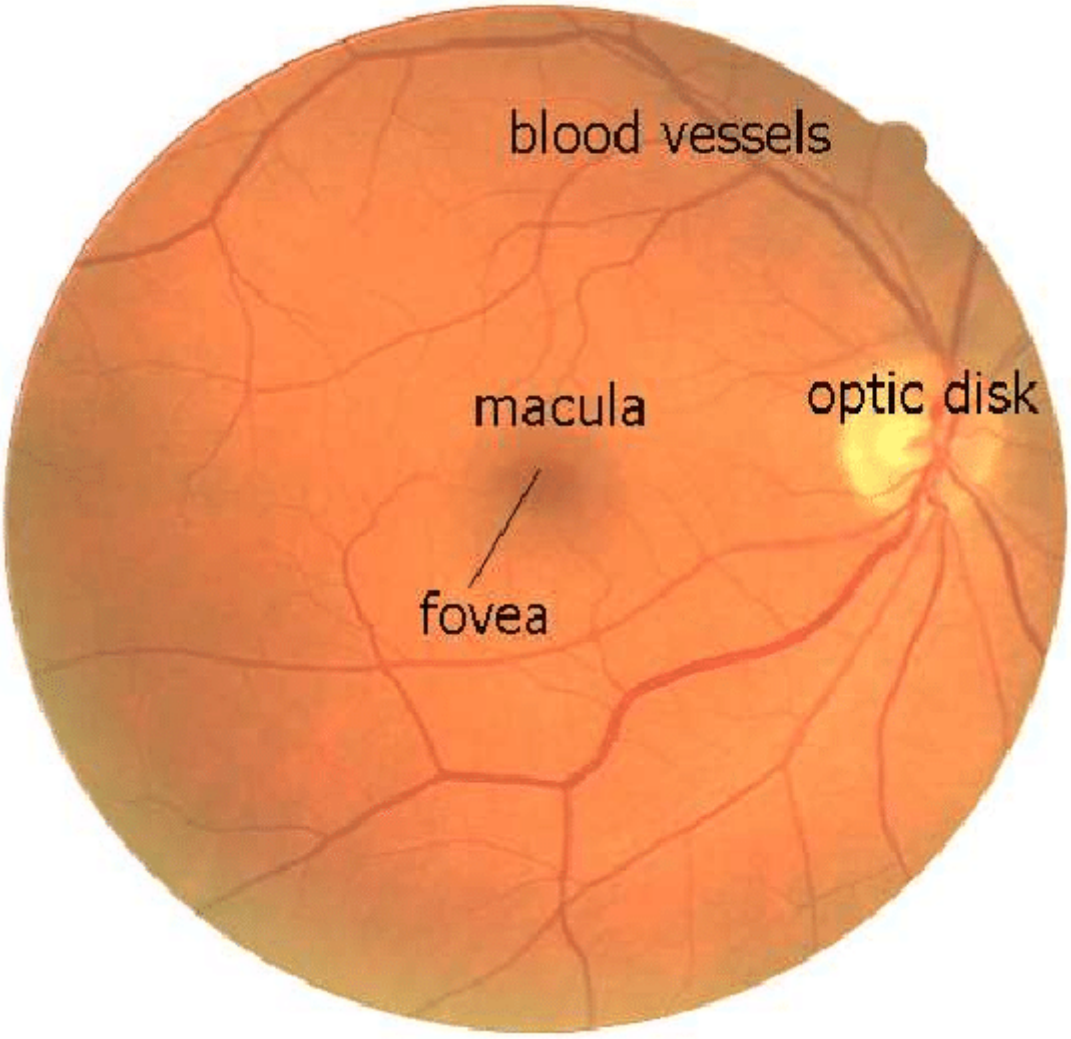

Figure 4.1: Color retinal fundus image with main features marked [181].

Analysis of the outcomes of previously reported evaluations pointed out that localization of OD and in particular localization of the fovea may probably be beneficial in augmenting the identification of feeble cases of DR. A respectable number of literature have addressed the identification of the locale of the OD. The modern OD detection schemes employ the relative position of the vasculature to identify the OD position. Identification of the fovea has obtained a very little attention. This may be due to the fact that fovea is more arduous to identify and does not introduce a high contrast structure.

The rest of this chapter is organized as follows. Section 4.2 deals with mathematical morphology. Region growing algorithm is presented in Section 4.3. Blood

vessel extraction using multistructure elements morphology is described in Section 4.4. Optic disc and fovea region identification steps are explained in Section 4.5. Results of blood vessel extraction are given in Section 4.6. OD and fovea identification results are presented in Section 4.7. Section 4.8 concludes the chapter.

4.2 Morphological Operation

Mathematical morphology is a tool for digging out image attributes that are helpful in the representation as well as description of edges, skeletons etc.

4.2.1 Erosion and Dilation

Erosion and dilation are the two primitive operations which act as the foundation of morphological operations.

4.2.1.1 Erosion

Let $f(x, y)$ is a contrast enhanced luma-image and $b(x, y)$ is a structuring element. (x, y) is the Cartesian co-ordinates. The erosion of f by b at any location (x, y) is described as the minimum value of the image in the area coextensive with b when the origin of b is placed at (x, y) and is described mathematically as shown in (4.1).

$$[f \ominus b](x, y) = \min_{(s,t)\varepsilon b}\{f(x + s, y + t)\} \tag{4.1}$$

where x and y are incremented such that the origin of b traverses every pictels in f.

4.2.1.2 Dilation

In a similar manner, dilation of f by b at an arbitrary location (x, y) is described as the maximum value of the image in the window outlined by $b(-x, -y)$ and is illustrated in (4.2).

$$[f \oplus b](x, y) = \max_{(s,t)\varepsilon b}\{f(x - s, y - t)\} \tag{4.2}$$

Here the structuring element is reflected about its origin. Dilation is identical to erosion except, instead of minimum value the maximum value is taken.

4.2.2 Opening and Closing

Opening operation, without any elaboration, is the erosion of f by b, followed by a dilation of the result with b. this is indicated in (4.3).

$$f \circ b = (f \ominus b) \oplus b \tag{4.3}$$

Likewise, the closing operation can be defined as the dilation of f by b, followed by an erosion of the result with b. This is shown in (4.4).

$$f \bullet b = (f \oplus b) \ominus b \tag{4.4}$$

4.2.3 Modified Top-Hat Transformation

Mathematical morphology, a useful technique for handling a variety of problems in image processing, is a group of morphological algebraic operations. Results of morphological operation largely based on the size as well as shape of structuring elements and are, therefore, selected as per the requirement of the allied application.

In 2-dimensional Euclidean space $\mathbb{R}^2$, let $I(p, q)$ represents a gray scale image. Let Se be a defined Structure Element (SEs) . The top-hat transformation described in (4.5) can be used to find edges of an image.

$$top - hat(I) = I - (I \circ Se) \tag{4.5}$$

where $\circ$ denote the opening operator. The issue with the top-hat operator is that it contains all the tiny ordinary intensity variations. Moreover, this problem severely aggravates due to irregular background illumination of the fundus image. The modified top-hat can be used to solve this problem [179]. In modified top-hat, the initial image is first subjected to morphological closing operation, and then a morphological opening operation is performed on the result. By using a minimum operator, the effect of the morphological opening operation is compared to the original image to obtain an image identical to the initial image excluding the boundaries. The revised top-hat transformation [179] is defined by (4.6).

$$top - hat(I) = I - min((I \bullet Se_c) \circ Se_\circ, ; I) \tag{4.6}$$

where $Se_\circ$ and Se_c stands for the SEs for opening ($\circ$) and closing ($\bullet$) operators, respectively.

4.2.4 Multistructure Elements Morphology

In an effort to detect simple, ordinary, and straight boundaries of an image single as well as symmetrical SEs are chosen. But as the complexity of the edges increases they fail to detect complex edges. For detecting such complex edges, we require more advanced SEs. In multistructure element morphology we gather many SEs in a single square window. Therefore, such SEs are competent enough for detecting various types of edges with different directions successfully.

Let $I(p,q) \mid p,q \in \mathbb{R}^2$ be a digital image. (4.7) define an SE in $(2N+1) \times (2N+1)$ square window.

$$Se_i = \{I(p+p_0, q+q_0), \phi_i = i \times \frac{180^0}{4N} \mid -N \leq p_0, q_0 \leq N\} \tag{4.7}$$

where $i = 0, 1, ...4N-1$ and ϕ_i represents the direction angles of Se_i. The size of the SE window is selected based on the required directional resolution. Figure 4.2 represents several Se_i for directional resolution $= 15^0$ and the 7×7 SE constructed by the synthesis of all Se_i of all directions.

4.2.5 Morphological Operations by Reconstruction

Even though morphological opening and closing operations allow the traits greater than SE unaltered, the important limitation of these operations is that they do not keep edge information safely and clearly. A new operator namely M- and N- sieves introduced by Bangham *et al.* [182] address this defect by emphasizing only on the size of the traits but without considering the shape. This problem is addressed by Morphological operators by reconstruction by considering both size as well as shape of the features [183].

If v and u symbolize marker and mask images, respectively, the geodesic dilation of size 1 of v with respect to u is represented by $\delta_u^{(1)}(v)$ as shown in (4.8) and is stated as the point-wise minimum amongst u and the element dilation $\delta^{(1)}$ of v.

$$\delta_u^{(1)}(v) = \delta^{(1)}(v) \wedge u \tag{4.8}$$

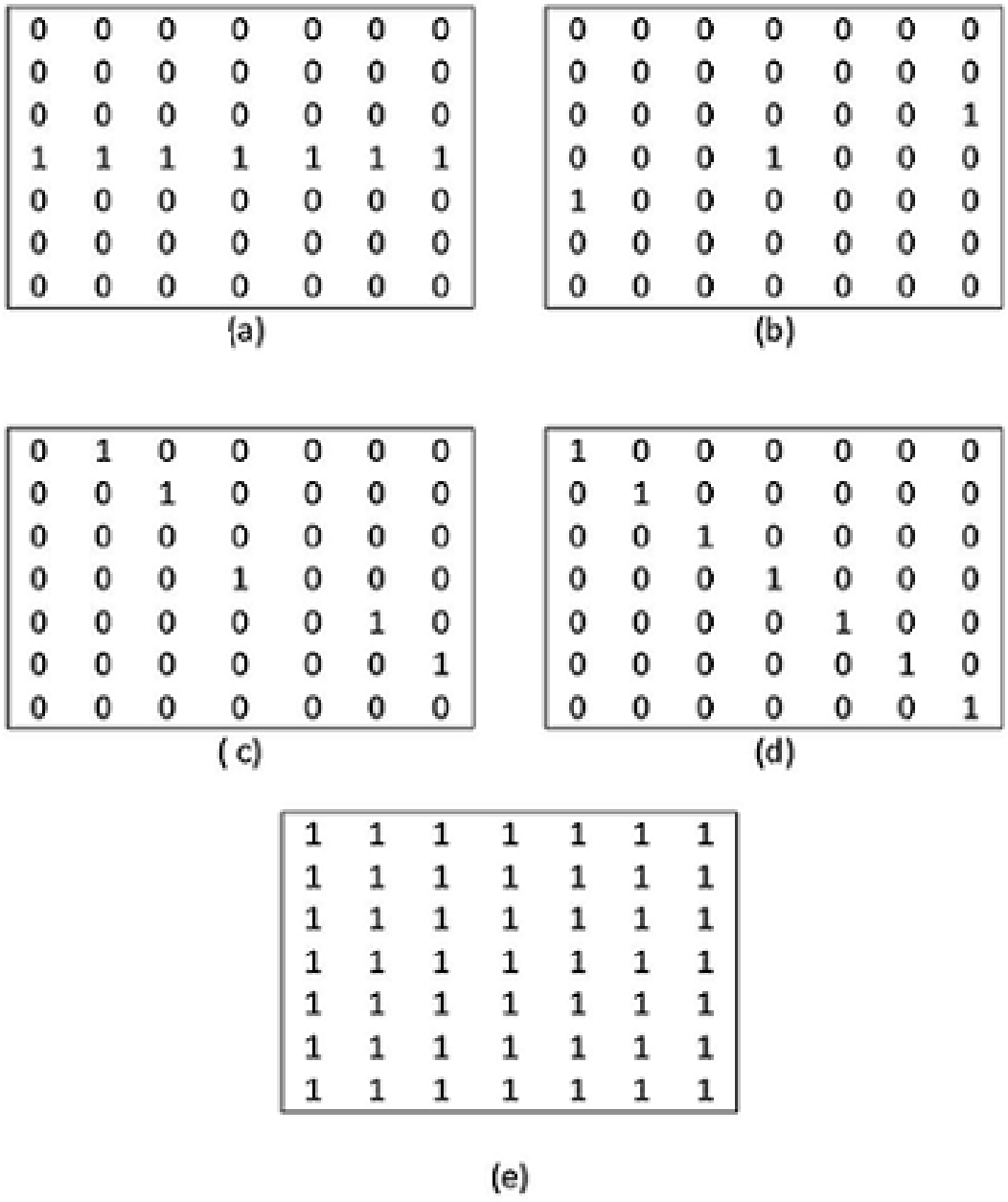

Figure 4.2: (a)-(d) Some of Se_i for *directional resolution* $= 15^0$ and $N = 3$. (e) 7×7 SE

Similarly, the geodesic erosion $\varepsilon_u^{(1)}(v)$ as shown in (4.9) can be described as the point wise maximum between u and the element erosion $\varepsilon^{(1)}$ of v.

$$\varepsilon_u^{(1)}(v) = \varepsilon^{(1)}(v) \vee u \tag{4.9}$$

Hence, the geodesic dilation(erosion) of any size is got by employing continuous geodesic dilation(erosion) of v in relation to u as illustrated in (4.10) and (4.11).

$$\delta_u^{(1)}(v) = \delta_u^{(1)}[\delta_u^{(i-1)}(v)] \tag{4.10}$$

$$\varepsilon_u^{(1)}(v) = \varepsilon_u^{(1)}[\varepsilon_u^{(i-1)}(v)] \tag{4.11}$$

for $i = 1, 2, 3..., \delta_u^{(0)}(v) = v$ and $\varepsilon_u^{(0)}(v) = v$. Both (4.10) and (4.11) converge after so many iterations and remain unchanged after that. This constant result is the reconstruction by dilation and is indicated by (4.12)

$$\delta_u^{rec}(v) = \delta_u^n(v) \tag{4.12}$$

where n is such that $\delta_u^n(v) = \delta_u^{(n+1)}(v)$. Similarly for reconstruction by erosion is denoted by $\varepsilon_u^{rec}(v) = \varepsilon_u^n(v)$ where n is such that $\varepsilon_u^n(v) = \varepsilon_u^{n+1}(v)$. So closing by reconstruction and opening by reconstruction represented by $v \bar{\bullet} Se$ and $v \bar{\circ} Se$ respectively, and described as shown in (4.13) and (4.14).

$$v \bar{\bullet} Se = \varepsilon_u^{(rec)}(v \bullet Se) \tag{4.13}$$

$$v \bar{\circ} Se = \delta_u^{(rec)}(v \circ Se) \tag{4.14}$$

In summery, in its first step morphological opening by reconstruction removes bright attributes smaller in size than the SE. In the following move, it revamp the contours of components that have not been fully eliminated by opening operation by performing dilation operation iteratively. While performing this operation the original image is treated as the reference. Closing by reconstruction is accomplished in case of dark features. Therefore the limitations of conventional morphological opening and closing operations such as deforming the contours, producing edge drift as well as new edges are restricted by utilizing opening and closing by reconstruction operations.

4.3 Region Growing

As implied by the name itself, region growing algorithm is a method that brings together pictels or tiny regions into bigger regions established on pre-established rules for growth. The fundamental strategy is to commence with a couple of "seed" points. Then from these seed points mount up regions by adding to each seed those near by pictels that have pre-established characteristics akin to the seed.

Criteria for choosing a group of one or more starting points usually can be derived from the nature of the problem. When deducible information is missing,

the method is to calculate at every pixel the corresponding set of characteristics that positively will be utilized to assort pixels to regions over the course of the growing process. If the outcome of these calculations displays clusters of values, the pictel whose characteristics puts them close to the centroid of these clusters can be utilized as seeds.

The choice of similarity rules relies not only on the issue under consideration, but also on the nature and type of the image data in hand. Without the intrinsic details available in images, descriptors are derived from the knowledge of spatial properties. Intensity levels are employed to carry out region analysis.

Segmentation based only on descriptors alone may produce misleading results. So in order to tackle this problem connectivity properties are also taken care of. Another important issue associated with region growing algorithm is the setting up of a stopping criteria. Region growth should cease when no other pictels fulfil the inclusion criteria. Local criteria like texture, intensity values and color do not take into account the history of region growth. The knowledge of size, similarity among selected pixels and the pixels grown up to now, and the geometry of the area being grown are some of the extra criteria that boost the capability of the region growing technique. The assumption made at this point is that a model of anticipated output is at least partly available.

Let a seed array is denoted by $S(x, y)$. This seed array contains 1s at the places of the seed points and 0s else-where. If both input image array $f(x, y)$ and seed array $S(x, y)$ are supposed to be of identical size and predicate to be employed at each position (x, y) is denoted as Q, then the region growing algorithm centred on 8 connectivity can be summarized in Algorithm 1.

4.4 Blood Vessel Detection Using Multistructure Elements Morphology

The block diagram of the proposed blood vessel extraction method is illustrated in Figure 4.3.

The multistructure elements procedure posses directionality property. Due to this property multistructure elements procedure has become very effective for edge detection applications. Therefore, mathematical morphology utilizing the

Algorithm 1 8 connectivity region growing

1: Obtain the entire connected components in $S(x, y)$.
2: Erode the connected component to one pixel and label every such pixels obtained as 1. Label all other pixels in S with 0.
3: Create an image f_Q using the following rule

$$f_Q(x,y) = \begin{cases} 1 & \text{if f(x,y) satisfies the given predicate Q at location(x,y)} \\ 0 & \text{Other wise} \end{cases}$$

4: Every 1-valued points in f_Q which are 8-connected to a particular seed point in S are appended to that seed point. Let the image obtained in this step is denoted by g.
5: Every connected components in g are labelled with another region label. This represents the segmented image.

multistructure elements are employed to identify the ridges of the retinal images.

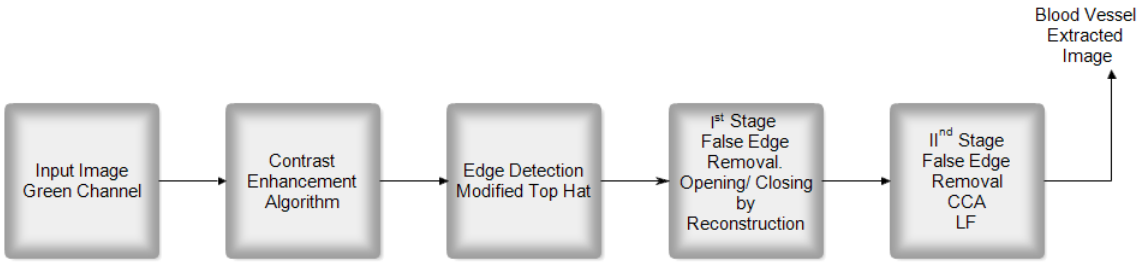

Figure 4.3: Block diagram of blood vessel extraction steps

The identified ridges not associated with the blood vessel tree are removed by morphological opening by reconstruction operation. This operation preserves the thin vessel edges. Employing the multistructure elements aids to enhance the performance of morphological opening by reconstruction step. The size of the structure elements (SEs) are chosen as 7×7 which are restricted by the diameter of the blood vessels [179]. Therefore, connected component analysis (CCA) together with length filtering is used to eliminate the remaining erroneous edges. So as to perform locally, the image is split into small tiles and connected component analysis, and length filtering is employed to each tile.

The steps involved to identify retinal blood vessels can be summarized in Algorithm 2 [179].

The blood vessel edges obtained by this method include some false edges due to uneven background. These false edges is eliminated in subsequent sections.

Algorithm 2 Detecting Blood vessel Edges

1: For the required directional resolution produce the SEs Se_i
2: Using the produced SEs in step 1 apply the selected edge detector function F on the original image and obtain the subedge image $F(I)_i$
3: Using the subedge image $F(I)_i$ procure the whole of the determined edges using (4.15)

$$F(I) = \sum_{i=0}^{M\text{-}1} W_i F(I)_i \tag{4.15}$$

where $F(I)$ represents the total edge image, $M = \frac{180}{\theta}$ and W_i is the assigned weight of each subedge image. Defining the assigned weights as $W_i = \frac{1}{M}$ will result the same effect to each $F(I)_i$. We can also use (4.16) so that the larger $F(I)_i$ has the greater effect.

$$W_i = \frac{F(I)_i}{\sum_{i=0}^{M\text{-}1} F(I)_i} \tag{4.16}$$

4.4.1 False Edge Removal

The morphological opening by reconstruction can be utilized to clear the false edges. Since multi structure elements are extremely sensitive to edges in every orientations, opening using multistructure elements are used to augment the result of the morphological opening by reconstruction. The SE employed in this step is the same as in the edge identification step, but with different weight. Here, in order to construct the $F(I)$, the maximum $F(I)_i$ is chosen rather than assigning weights to each $F(I)_i$. By doing so weak erroneous edges are eliminated. This restrict them from taking part in the construction of $F(I)$. Then, utilizing a flat structure element reconstruction by dilation is performed. Since average width of blood vessel is 5 pictels, a larger SE for opening causes the removal of more objects, and fully removes some small vessels because they cannot be restored with reconstruction by dilation operation. So, to achieve a clear final result void of false edges, length filtering is utilized.

4.4.2 Length Filtering (LF)

In adaptive connected component analysis (ACCA) images are considered in distinct tiles and perform CCA and LF to each tile. In CCA connected component pixels which are identified above a certain threshold and labeled using eight connected neighbourhood are regarded as a single object. After CCA, the components with length less than a the threshold are removed. The specific threshold can be obtained utilizing a thresholding method proposed in [184] and given by (4.17).

$$T = \mu - \alpha\sigma \tag{4.17}$$

where μ and σ are the mean and std. Also, α should be small enough ($\alpha < 1$) for poor sharpness images. Finally all the images are combined to a single image to obtain the ultimate blood vessel extraction result.

Consequently, the proposed blood vessel identification procedure is summarised in Algorithm 3.

Algorithm 3 Blood Vessel Extraction

1: Apply the contrast enhancement algorithm discussed in Chapter 3 to the green channel of the original coloured image and get the enhanced image.
2: Remove the assessed background from the enhanced image
3: Employ the modified top-hat transform utilizing the multistructure elements morphology and obtain the edge image
4: Using multistructure elements employ opening by reconstruction to remove the false edges.
5: Apply length filtering along with adaptive CCA to eliminate the still remaining false edges.

4.5 Optic Disc and Fovea Localization

Figure 4.4 represents the process of OD and fovea extraction.

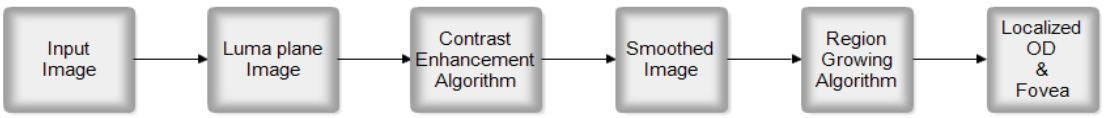

Figure 4.4: Block diagram of OD and Fovea extraction steps

In order to remove variations due to image acquisition method, image pre-processing is used. The image enhancement method discussed in Chapter 3 is employed to nullify the effect of non-uniform illumination and enhance the image contrast. Here the pre-processing algorithm is applied to the luma component of the RFIs because of the following reason. In RFIs, the OD corresponds to the brightest spot in the image. On the other hand fovea is associated with the darkest spot of the image. YCbCr is a family of color models where Y represents the luma component and Cb and Cr are blue-difference and red-difference chroma components respectively. The Y component is defined to have range from 16-235 while Cb and Cr are described to have a range of 16 to 240. Level 128 indicates zero signal. This Y (luma) component gives the highest contrast between OD and the

background. Same is the case for fovea also. So luma component of YCbCr image model is employed for the localization of OD and fovea. The following (4.18) to (4.20) are used in order to convert the RGB image into YCbCr model.

$$Y = 16 + \frac{65.738R}{256} + \frac{129.057G}{256} + \frac{25.064B}{256} \tag{4.18}$$

$$C_b = 128 - \frac{37.945R}{256} - \frac{74.494G}{256} + \frac{112.439B}{256} \tag{4.19}$$

$$C_r = 128 + \frac{112.439R}{256} - \frac{94.154G}{256} - \frac{18.285B}{256} \tag{4.20}$$

After employing the contrast enhancement algorithm introduced in Chapter 3 to the luma component of the RFIs, the OD and fovea in these images become clearly visible. But the algorithm also enhances the blood vessels, which is highly undesirable. Presence of blood vessels clutter the OD and fovea. So it is essential to smooth out the blood vessels in the RFIs keeping the OD and fovea regions unchanged. Several methods exists to smooth out the blood vessels. Out of the different methods available, morphological operations gives better results. So in this method morphological operations are used to smooth out the blood vessel pixels in RFIs. Opening conceals bright details smaller than the specified SEs, whereas closing suppresses dark details. So closing operation is used to eliminate or smooth out the blood vessels in the enhanced image. As mentioned earlier, closing operation conceals dark details smaller than the used SEs, selection of the size of structuring element is very important. So we choose a structuring element whose size is bigger than that of blood vessel (7×7) [179]and smaller than that of fovea whose approximate size is 5.5mm i.e.,18×18 [185, 186]. Hence, a 9×9 size is chosen for structuring element which is greater than the blood vessel size and less than that of the fovea so that the closing operation does not affect the fovea region. Then the region growing algorithm described in Section 4.3 is used to segment out the OD and fovea.

4.6 Results of Blood Vessel Extraction

The algorithm summarized in Section 4.4.2 is applied to both DRIVE and HRF image database. MATLAB version R2013b is used to implement the proposed method. The undesired artefacts exterior to the fundus disc, that are produced

in the enhancement step, are eliminated by multiplying the enhanced image with the disc fundus region. Then by modified top-hat operation utilizing the multi-structure element morphology the edges of the image are detected. We used a 7×7 SE with $directional\,resolution = 15^0$. Then the false edges are removed by morphological opening using multistructure elements by reconstruction. After that the image is divided into several tiles and CCA and LF are locally employed to completely remove the prevailed unwanted edges. The size of each block is determined experimentally and is 61×61. The results of each step is shown in Figure 4.5.

4.6.1 Evaluation

True Positive Rate (TPR) or Sensitivity or Recall, False Positive Rate (FPR) , Accuracy (ACC), Precision, F1-Score and Matthews Correlation Coefficient (MCC) are used to assess the algorithm performance. These measures can be defined as shown in (4.21) to (4.26). It is very important to recognize that none of the performance evaluation metrics can convey the full performance of the algorithm individually. Conclusions derived from analysing a combination of metrics are more reliable than that obtained by analysing only one metric. It is therefore we use a combination of the above metrics when we are working on evaluating the algorithm performance.

$$TPR = \frac{Number\ \ of TP}{Total\ \ number\ \ of\ \ TP\ \ and\ \ FN} \tag{4.21}$$

$$FPR = \frac{Number\ \ of\ \ FP}{Total\ \ number\ \ of\ \ FP\ \ and\ \ TN} \tag{4.22}$$

$$ACC = \frac{Total\ \ number\ \ of TP\ \ and\ \ TN}{Total\ \ number\ \ of\ \ pixels} \tag{4.23}$$

$$Precision = \frac{Total\ \ number\ \ of\ \ TP}{Number\ \ of\ \ TP\ \ and\ \ FP} \tag{4.24}$$

$$F1\text{-}Score = \frac{2(Precision \times Recall)}{(Precision\ +\ Recall)} \tag{4.25}$$

$$MCC = \frac{TP \times TN - FP \times FN}{\sqrt{(TP+FP)(TP+FN)(TN+FP)(TN+FN)}} \tag{4.26}$$

where TP (True Positive) and TN (True Negative) are the blood vessel pictels and background pictels which are correctly detected respectively. FN (False Negative) is the pictels associated with vessel, but is recognized as background pictels mistakenly and FP (False Positive) shows the pictels not associated to a vessel, but is identified as blood vessel pixels.

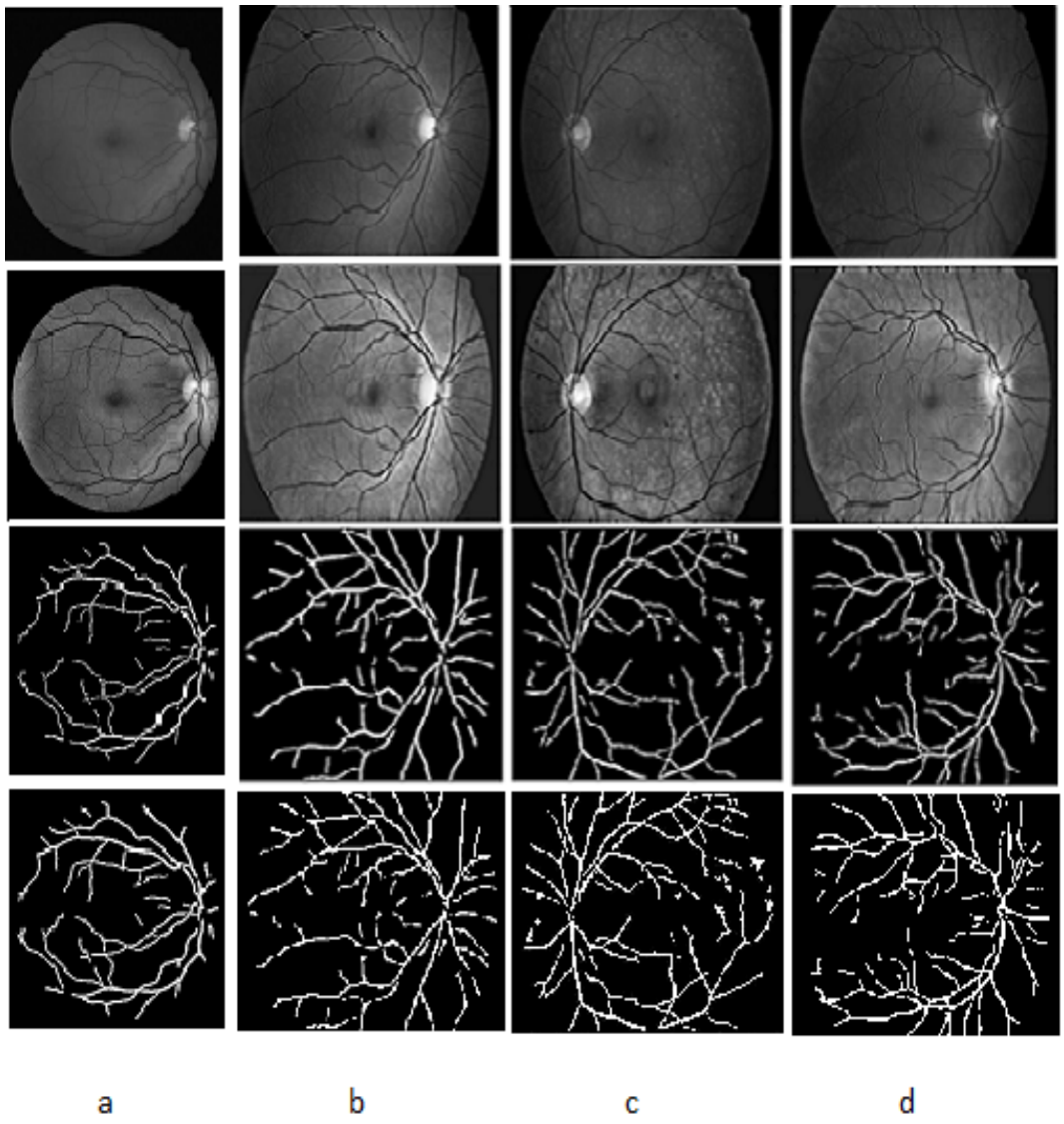

Figure 4.5: Result of blood vessel extraction. (a) Result of proposed method to image 40 of DRIVE database. (b)-(d) Result of proposed method to image 01_h, 01_dr, 01_g of HRF database, respectively. From top to bottom they are the green channel, contrast enhanced image, result before applying length filtering and last row are result after applying length filtering

TPR or recall indicates the capability of the algorithm to accurately detect blood vessel. FPR is the probability of falsely recognizing a pixel as blood vessel pixel. ACC provides a general measure of the ratio of total well-detected pictels as per the gold standard hand-labelled segmentation. When the cost of false positive is high precision is a good measure. When a balance between precision and recall is needed F1-Score is a good option. MCC is more enlightening when compared to F1-Score and ACC in assessing the performance of binary classification problems. F1-Score and ACC never completely consider the size of the four classes of the confusion matrix in their final score computation and hence they can be misleading.

Table 4.1 shows the results obtained when the algorithm is tested using DRIVE database. A comparison of our method with other published results are depicted in Table 4.5. It is evident from Table 4.5 that our method provides more ACC and TPR and lowest FPR.

The proposed method is also assessed with the HRF database. All three types of images, -images of healthy eyes, images with signs of DR and glaucoma- are used. Tables 4.2 to 4.4 show results of the parameters TPR, FPR, ACC, Precision, F1-Score and MCC evaluated on particular datasets. Average values and standard deviations are computed for each parameter as well. The average values indicated at the bottom row reveals the robustness of our algorithm. A quantitative comparison of average values of ACC, show more than 96% of truly classified pixels in the field of vision for all datasets. The average values of F1-Score shows that this algorithm maintains a relatively high balance between precision and recall. It can be observed from Table 4.2-4.4 that the MCC values are close to 1 which reveals that the method discussed here fully considered the four classes of the confusion matrix.

Table 4.5 shows the comparison of performance of the discussed method with other approaches. It is illustrated in the Table 4.5 that our method provides more ACC and TPR and lowest FPR.

Table 4.6 compares the attainment of the method with [187]. Only SE, FPR and ACC are included for comparison in Table 4.6 because [187] has not used F1-Score and MCC for evaluating the method. Table 4.6 clearly shows that the method developed is superior to other methods.

4.7 Results of OD and Fovea Segmentation

The algorithm is applied to the contrast enhanced luma plane image of all images obtained from DRIVE database and from a local eye hospital. Total of 25 images were obtained from the hospital. An expert ophthalmologist helped to mark the regions of OD and fovea in 10 of these 25 images collected. He also helped to mark the severity of DR in these images. For DR screening application, knowledge of only the rough midpoint of both OD and fovea structures are enough because of the fact that, this application do not want to segment optic disc and fovea but only want to mask them.

Table 4.1: Results obtained with DRIVE images.

Image No	TPR	FPR	ACC	PRECESSION	F1-SCORE	MCC
21	0.9429	0.0036	0.9922	0.9576	0.9502	0.9460
22	0.8825	0.0043	0.9854	0.9539	0.9168	0.9097
23	0.9049	0.0532	0.9436	0.5882	0.7130	0.7028
24	0.8861	0.0075	0.9805	0.9368	0.9107	0.9003
25	0.8512	0.0068	0.9805	0.9254	0.8868	0.8771
26	0.9621	0.0039	0.9933	0.9568	0.9594	0.9557
27	0.8622	0.0069	0.9814	0.9237	0.8919	0.8824
28	0.8509	0.0040	0.9817	0.9588	0.9016	0.8935
29	0.9374	0.0076	0.9877	0.9202	0.9287	0.9221
30	0.9551	0.0104	0.9868	0.8875	0.9201	0.9136
31	0.9721	0.0113	0.9876	0.8600	0.9126	0.9080
32	0.9649	0.0073	0.9904	0.9227	0.9433	0.9383
33	0.9484	0.0048	0.9912	0.9486	0.9485	0.9437
34	0.8696	0.0274	0.9625	0.7755	0.8199	0.8006
35	0.9270	0.0076	0.9867	0.9214	0.9242	0.9169
36	0.8802	0.0108	0.9773	0.9087	0.8942	0.8816
37	0.9172	0.0067	0.9867	0.9297	0.9234	0.9161
38	0.9695	0.0182	0.9807	0.8352	0.8974	0.8898
39	0.9616	0.0168	0.9814	0.8450	0.8995	0.8916
40	0.9535	0.0101	0.9870	0.8922	0.9218	0.9154
Average	0.9200	0.0115	0.9822	0.8924	0.9032	0.8953
STD	0.0415	0.01112	0.0110	0.0839	0.0525	0.0547

Table 4.2: Results obtained with HRF HEALTHY images.

Image No	TPR	FPR	ACC	PRECESSION	F1-SCORE	MCC
1	0.8732	0.0183	0.9706	0.8438	0.8582	0.8421
2	0.9409	0.0294	0.9677	0.7802	0.8530	0.8397
3	0.6234	0.0049	0.9556	0.9383	0.7491	0.7441
4	0.7647	0.0133	0.9656	0.8586	0.8089	0.7917
5	0.9430	0.0240	0.9729	0.7980	0.8645	0.8532
6	0.8928	0.0293	0.9627	0.7759	0.8303	0.8119
7	0.9057	0.0206	0.9728	0.8120	0.8563	0.8428
8	0.8446	0.0168	0.9692	0.8492	0.8469	0.8298
9	0.9571	0.0241	0.9744	0.7708	0.8539	0.8460
10	0.8431	0.0230	0.9654	0.7758	0.8081	0.7899
11	0.9480	0.0297	0.9682	0.7681	0.8486	0.8368
12	0.9127	0.0274	0.9663	0.7972	0.8510	0.8346
13	0.8288	0.0157	0.9706	0.8353	0.8320	0.8159
14	0.8180	0.0252	0.9610	0.7579	0.7868	0.7661
15	0.9748	0.0279	0.9723	0.7503	0.8479	0.8417
Average	0.8714	0.0220	0.9677	0.8074	0.8330	0.8191
STD	0.0880	0.0068	0.0049	0.0484	0.03100	0.0313

Table 4.3: Results obtained with HRF DR images.

Image No	TPR	FPR	ACC	PRECESSION	F1-SCORE	MCC
1	0.9472	0.0286	0.9698	0.7031	0.8071	0.8014
2	0.8376	0.0168	0.9718	0.8094	0.8233	0.8081
3	0.8565	0.0473	0.9455	0.5975	0.7039	0.6882
4	0.8544	0.0360	0.9561	0.6485	0.7373	0.7220
5	0.8372	0.0130	0.9755	0.8423	0.8397	0.8265
6	0.6360	0.0012	0.9662	0.9810	0.7717	0.7750
7	0.7745	0.0165	0.9640	0.8280	0.8004	0.7812
8	0.8642	0.0479	0.9441	0.6434	0.7376	0.7168
9	0.7523	0.0071	0.9726	0.9068	0.8224	0.8118
10	0.7125	0.0145	0.9569	0.8518	0.7759	0.7560
11	0.7932	0.0201	0.9610	0.8158	0.8043	0.7828
12	0.8359	0.0218	0.9665	0.7748	0.8042	0.7866
13	0.8446	0.0170	0.9713	0.8208	0.8325	0.8170
14	0.8318	0.0303	0.9572	0.7322	0.7788	0.7571
15	0.8832	0.0287	0.9641	0.7312	0.8000	0.7847
Average	0.8174	0.0231	0.9628	0.7791	0.7893	0.7743
STD	0.0725	0.0130	0.0091	0.1005	0.0374	0.0386

Table 4.4: Results obtained with HRF GLUCOMA images.

Image No	TPR	FPR	ACC	PRECESSION	F1-SCORE	MCC
1	0.9501	0.0252	0.9729	0.7574	0.8429	0.8347
2	0.9097	0.0228	0.9716	0.7853	0.8429	0.8301
3	0.9252	0.0215	0.9748	0.7638	0.8368	0.8277
4	0.9216	0.0209	0.9747	0.7843	0.8474	0.8369
5	0.9368	0.0204	0.9763	0.7922	0.8585	0.8492
6	0.9321	0.0226	0.9738	0.7816	0.8502	0.8399
7	0.8873	0.0187	0.9741	0.7957	0.8390	0.8264
8	0.9095	0.0269	0.9681	0.7422	0.8174	0.8051
9	0.8959	0.0203	0.9733	0.7862	0.8375	0.8251
10	0.8751	0.0169	0.9748	0.8124	0.8426	0.8296
11	0.8384	0.0167	0.9705	0.8288	0.8336	0.8175
12	0.8485	0.0285	0.9600	0.7554	0.7992	0.7787
13	0.8207	0.0172	0.9698	0.8065	0.8135	0.7971
14	0.8448	0.0264	0.9628	0.7463	0.7925	0.7739
15	0.8263	0.0253	0.9621	0.7521	0.7875	0.7678
Average	0.8881	0.0220	0.9706	0.7793	0.8294	0.8160
STD	0.0417	0.0038	0.0050	0.0249	0.0213	0.0247

Table 4.5: Comparison of performance between different methods.

Method	TPR	FPR	ACC
Mendoça and Campilho [188].	0.7344	0.0236	0.9452
Staal *et al.* [189].	0.6780	0.0170	0.9441
Martinez-Perez *et al.* [190].	0.7246	0.0345	0.9344
Niemeier *et al.* [191].	0.6898	0.0304	0.9416
Miri and Mahlooifar [179]	0.7352	0.0205	0.9458
Our Method	0.9200	0.0115	0.9822

Table 4.6: Comparison of the proposed method with other blood vessel segmentation algorithm [187]-evaluation on HRF Database

	TPR	FPR	ACC
proposed method (HRF-healthy images)	0.8714	0.0220	0.9677
Odstrcilik *et al.*(HRF-healthy images) [187]	0.7861	0.025	0.9539
proposed method (HRF-DR images)	0.8174	0.0231	0.9628
Odstrcilik *et al.*(HRF-DR images) [187]	0.7463	0.0381	0.9445
proposed method (HRF-Glaucoma images)	0.8881	0.0220	0.9706
Odstrcilik *et al.*(HRF-Glaucoma images) [187]	0.7900	0.0362	0.9497

Figure 4.6 shows the result obtained with this algorithm at different stages. Figure (a) shows the input image. Figure (b) is the luma component of the input image and Figure (c) is the image obtained after applying the contrast enhancement algorithm. Figure (d) is the result obtained after smoothing out the blood vessels using morphological operation. The last row Figure (e) is the OD and fovea localized results. From this results it is clear that this algorithm estimates the mid points of OD and fovea with 100% accuracy.

The first column of Figure 4.6 shows the results obtained with a normal eye. In this case both OD and fovea are accurately localized. The second column of the figure indicates the results obtained with an eye image in which fovea is not visible. In this case the algorithm localizes only the OD. Since the fovea is not visible in this case, the fovea part is not detected in this case. The advantage of the proposed method is that it is not falsely detecting any other region as fovea if the fovea is not visible. The third column is the result obtained with a DR affected eye. But in this case the severity level is less. In this case also the algorithm detects locus of OD and fovea correctly. The last column shows the result obtained when an eye with severe DR is given as input. In this case also the method succeeded in identifying the mid points of OD and fovea. It can be observed that the proposed method localizes the OD and fovea in all the cases.

In order to assess the performance of the algorithm quantitatively, the ground truth of the images are necessary. Since most of the images utilized in this work is collected from a local eye hospital, the ground truth of these images are not readily available. So with the help of an experienced ophthalmologist the ground truths are marked on only ten original images. Utilizing these ground truth marked images and the obtained results a parameter namely overlapping score (OS) as defined by (4.27) is calculated.

$$OS = \frac{(R1 \cap R2)}{R1 \cup R2} \tag{4.27}$$

where R1 indicates the area under annotated ground truth; R2 represents the area under segmented region. These areas are also directly proportional to the number of pixels. $\cap$ and $\cup$ indicates intersection and union respectively. Ideal value expected for OS is 1.

Figure 4.7 shows the input image, ground truth marked images and final results obtained. Since these images are obtained from a local hospital their aspect ratio is different from that of the previous images.

Table 4.7 shows the overlapping score obtained for ten samples. It is noted that the average overlapping score obtained is 0.9726, which indicates that 97.26% of the segmented area matches with the ground truth. Thus, this method can precisely distinguish the area that have identical traits as that of the defined predicate. This method utilizes a simple concept namely region growing. It makes use of minimum number of seeds.

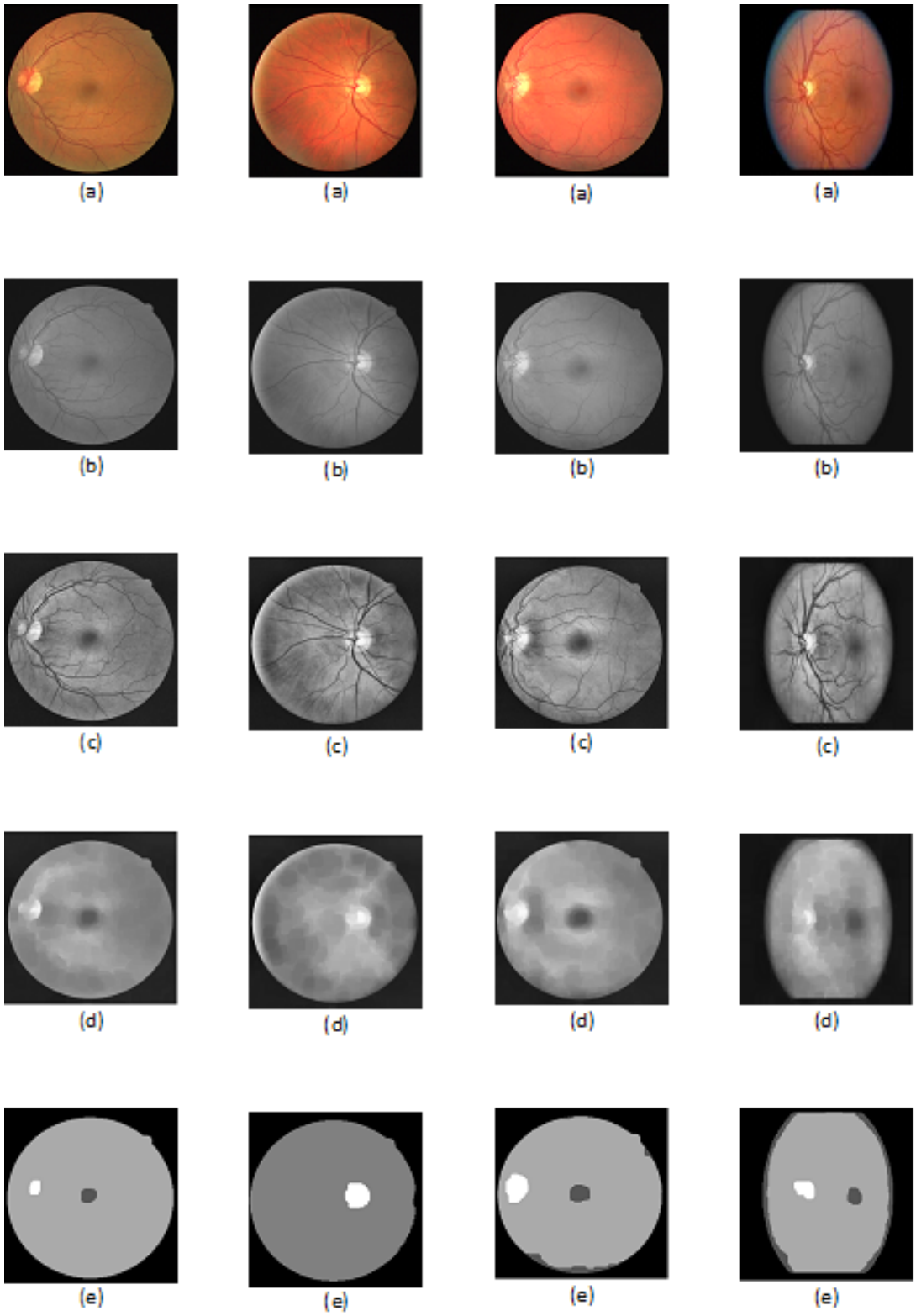

Figure 4.6: Results obtained with the proposed method on DRIVE database. From top to bottom row they are the (a) Input image (b) Luma plane image (c) Contrast enhanced image (d) Blood vessel smoothened image (e) Localized OD and fovea.

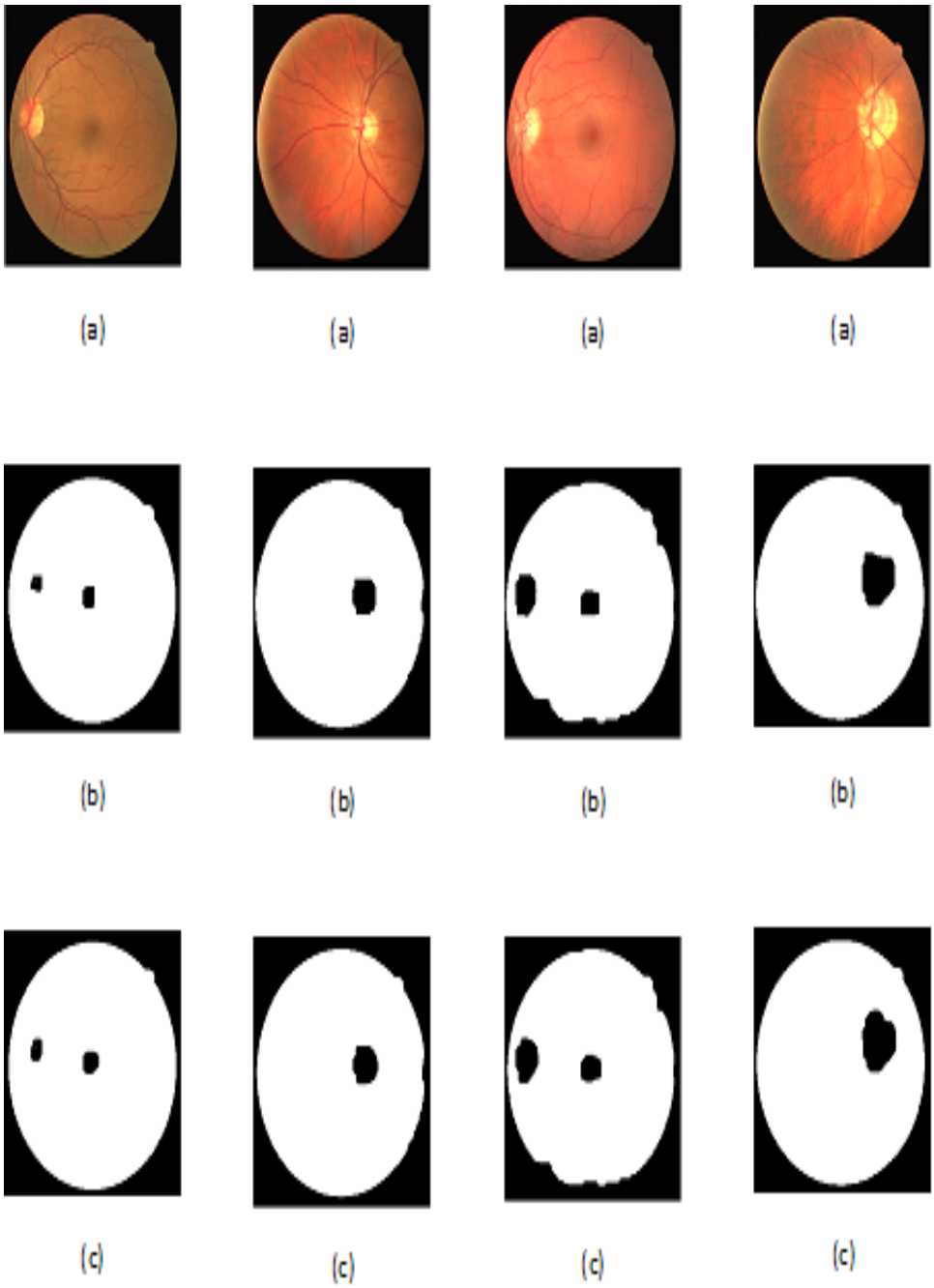

Figure 4.7: Result obtained with proposed method on images collected from local hospital. From top to bottom they are the (a)Input image (RGB) (b) Ground truth given by expert (Binary) and (c) Result obtained with proposed method (Binary)

4.8 Conclusion

Methods to extract retinal blood vessels, Optic Disc and Fovea are described in this chapter. Multistructure elements morphology is used to identify the blood

vessels. Morphological opening by reconstruction using multistructure elements is employed to eliminate unwanted edges. The remained false edges are removed by utilizing CCA and LF locally. The quantitative performance results of segmentation shows that this method successfully identifies the blood vessels with accuracy greater than 96%, F1-Score greater than 0.8 and MCC value greater than 0.77.

Table 4.7: Overlapping Score table

SI.No	OS value
1	0.9777
2	0.9981
3	0.9931
4	0.9971
5	0.9953
6	0.9950
7	0.9143
8	0.9020
9	0.9721
10	0.9813
Average	0.9726

Morphological closing operation and region growing are used to identify and find exactly the OD and fovea in RFIs without making any strong assumptions regarding the positions of OD and fovea. This will aid in detection and labelling of eccentricities in human eye. Moreover, size as well as geometrical shape of these detected traits can be used for computerized classification of different impairments in the human eye. As per the expert opinion, the system found the mid point of the OD and fovea with 100% accuracy. Since the method was evaluated on real data obtained from a nearby hospital, the average value 0.9726 obtained for the quantitative parameter, OS substantiate the robustness of the method.

To summarize, robust algorithms to extract retinal blood vessels and to identify the locus of the OD and fovea in RFIs is presented in this chapter. These algorithms show results as good as the existing methods. This brings the system the capability for employment in a computerized DR screening system.

Chapter 5

Diabetic Retinopathy Detection

5.1 Introduction

As mentioned in Chapter 1 Diabetic retinopathy is characterized by the presence of red lesions (microaneurysms) and bright lesions (exudates) which appear as small white or yellowish white deposits with sharp margins and variable shapes located in the outer layer of the retina. The detection of these lesions are crucial for DR screening systems. The aim of the work described in this chapter is to design and develop a system that will be able to differentiate normal and abnormal RFIs using Bag of Visual Words (BoVW) approach.

The chapter is arranged as follows. Section 5.2 briefly describes the steps involved in image classification tasks using BoVW. The next section 5.3 gives the details about the methodology used. This section contains sub-sections that deals with preprocessing of RFIs, elimination of anatomical structures like blood vessels and optic disc from RFIs, and classification of RFIs. Section 5.4 describes the results obtained while executing the algorithm. Finally Section 5.5 gives the summary of this chapter.

5.2 Bag-of-Visual Words

BoVW model has become one of the popular methods for image classification. Sivic and Zisserman in [192] described the BoVW method as an analogy with text retrieval and analysis where a document is characterized by word counts irrespective of their order in which they appear in the text. Since its introduction in 2003, BoVW received state-of-the art performance in computer vision applications. The common steps involved in image classification tasks using BoVW can be represented as shown in Figure 5.1.

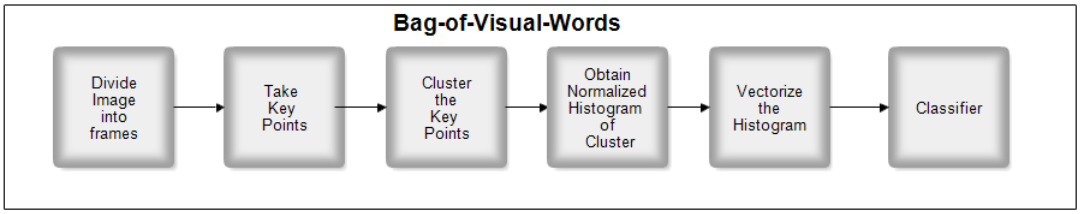

Figure 5.1: Steps in BoVW technique.

It consists of the following steps

1. Key-points localization from the image
2. Key-points description using local descriptors.
3. Vector quantization for the descriptors by clustering them into K-clusters using K-means clustering. This step results a visual words vocabulary which forms the codebook.
4. Accumulate the visual words into a histogram to establish the signature of each image.
5. Normalize the histogram by dividing the count of each visual word over the total number of visual words, and
6. Train a classifier (usually SVM) using the obtained image signature for classification task.

5.2.1 Speeded Up Robust Feature (SURF)

As the name implies SURF is a fast and robust method for local, similarity invariant representation and comparison of images. SURF is composed of feature extraction and feature description steps. The speed is achieved by the use of integral images and box filters.

SURF relies on the determinant of Hessian matrix for selecting the location and the scale. Scale spaces are generally implemented as image pyramids. Due to the use of box filters and integral images, SURF does not have to iteratively apply the same filter to the output of a previously filtered layer, but instead, can apply such filters of any size at exactly the same speed directly on the original image, and even in parallel.

The first step in creating SURF descriptor is fixing an orientation which is reproducible. This step is achieved by collecting information from the circular region around the key point. Then SURF descriptor is extracted by constructing a square region aligned to the chosen orientation. For identifying reproducible orientation Haar-wavelet response along X and Y directions in a circular neighbourhood of radius 6s, where s is the scale, around the keypoint is calculated. The sampling step is chosen as s and so it is scale dependent. So the size of the wavelet is large at high scales. So integral images are used for fast filtering. Thus the sum of horizontal and vertical wavelet responses in a sliding orientation window covering an angle of $\frac{pi}{2}$ are calculated. The largest of this sum value provides principal orientation of feature descriptor.

In order to extract descriptor components, a 20s size square region with center as the key-point is constructed. This square region is oriented along the orientation of feature descriptor obtained earlier. Then the region is split into smaller regions of 4×4. For each sub-region, compute a few simple features. The horizontal and vertical wavelet responses, denoted as dx and dy respectively, are summed up over each sub-region. Sum of absolute value of responses is also calculated to account for the polarity of intensity changes. Hence each sub-region has a 4-dimensional descriptor vector $\mathbf{V} = (\sum dx, \sum dy, \sum |dx|, \sum |dy|)$. This results in a descriptor for all 4×4 sub-regions of length 64.

5.2.2 K-means clustering

K-means clustering tries to minimize the distance between intra cluster data-points while keeping the distance between clusters as far as possible. It calculates the sum of squared distance between the data points and the cluster's centroid- which is the arithmetic mean of all the data points that belong to that cluster. The data point will be assigned to that cluster which gives least distance with that data point. Less intra cluster variation shows homogeneity of data points with in the cluster. K-means algorithm is given below 4.

5.2.3 Support Vector Machine

SVM try out to classify data in a dataset into two groups by the use of a linearly separable hyperplane of any dimension. The optimum hyperplane is the one that maximizes the distance between the hyperplane and a few close points. This distance is known as the margin. Since the close points control the hyperplane they are known as support vectors. Unlike the maximum margin classifier which

Algorithm 4 K-means Clustering

1: Specify number of cluster K
2: Shuffle the dataset.
3: Initialize centroids of clusters randomly.
4: **repeat**
5: Find out the sum of squared distance between data points and all centroids.
6: Assign each data point to the closest centroid cluster.
7: Recalculate the cluster centroids.
8: **until** No change in centroids

demands the classes to be perfectly linearly separable support vector classifier allows misclassification through the use of a soft margin. Tuning parameter will control the amount of misclassification. When the tuning parameter(C) is small, the amount of misclassification is also small. Even though low value of C will give low bias and high variance, it will not generalize the classifier well. Also too low value of C leads to over-fitting. If the tuning parameter is large, the classifier would generalize better but with high amount of bias and misclassification. In order to handle non-linearly separable classes, support vector classifier uses the kernel trick. IT employs a kernel function to map the non-linear data to higher dimensions. The kernel function adds dimensions to the problem for classification so that the data becomes linear and finds the decision boundary in the higher dimensional space.

5.3 DR Identification

The algorithm for automatic discovery of normal and abnormal RFIs is described in this section. Blood vessels are the cause of false positives in detection of microaneurysms and hemorrhages. OD contains the maximum pixel values in the luma plane of RFIs. It is also a source of false positives in bright lesion detection. So the elimination of OD and blood vessels are the necessary steps to extract features of RFIs and classify it into normal and abnormal groups. Also, distance of the lesions from fovea is important in determining the severity of DR. Since the main aim of the work described in this chapter is to only detect DR, and not its severity, fovea does not play an important role here. The pictorial representation of the proposed DR detection method is shown in Figure 5.2.

5.3.1 Preprocessing

Fundus images in the RGB model contains red, green, and blue planes. The image enhancement algorithm discussed in Chapter 3 is used to enhance the image

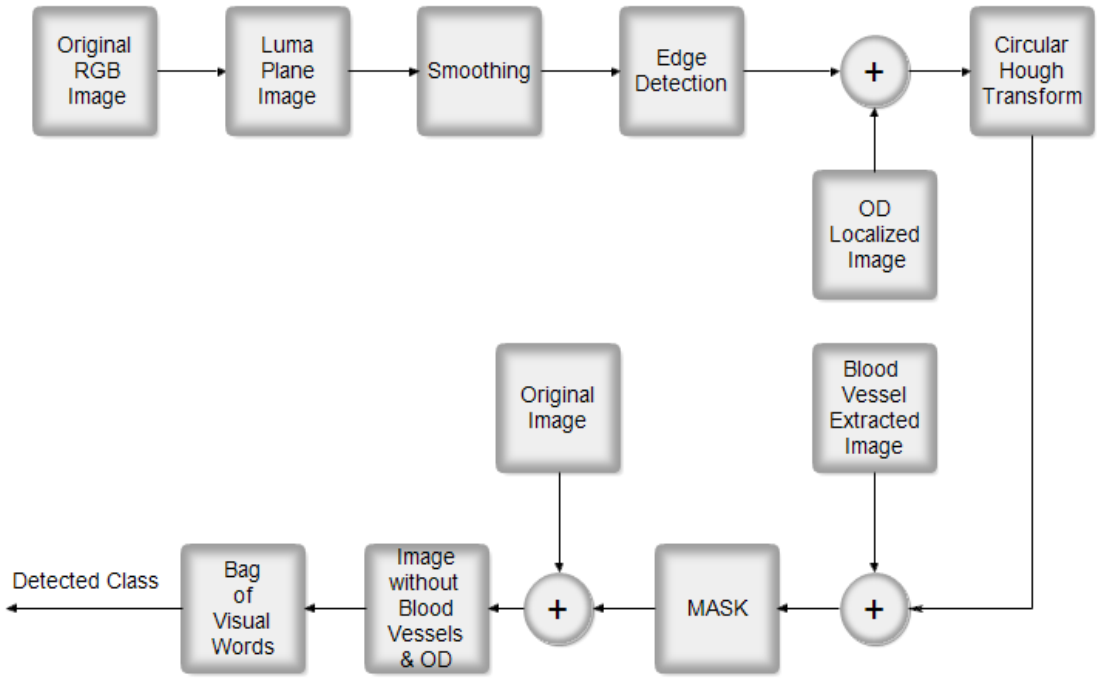

Figure 5.2: Block diagram of proposed DR detection method

contrast. After enhancing the contrast using the method described in Chapter 3, noise reduction technique is applied to all the three components of contrast enhanced RGB image to remove unwanted components present in the image. Different noise removal techniques such as Laplacian filtering, Average filtering, Motion filter and Gaussian filter are tried and their results are given in Figure 5.3. From these results it is found that Gaussian filter gives better results.

The Gaussian filter is lucidly symmetric. So it will not bias edge identification. We know that fourier trasform of a Gaussian function is Gaussian. That means, the fourier transform of a Gaussian function has a single lobe. So the image smoothened by Gaussian filter will not be corrupted by contributions from undesired high frequency signals. On the other-hand it retains most of the desirable image properties. As shown in (5.1), based on Gaussian function, the Gaussian smoothing administers average value of neighbouring pixels and the operator clears the effect of noises. It act by removing components with high frequencies from the image.

$$Img_s(x, y) = Img(x, y) * G_{au}(x, y) \tag{5.1}$$

where $*$ stands for convolution, $Img_s(x, y)$ is Gaussian filtered output, $G_{au}(x, y)$ is Gaussian filter and $Img(x, y)$ is the input image. So in this work Gaussian filter (1.5) is employed to perform smoothing (5.3) operation. Sobel edge detec-

tor is applied to the Gaussian filtered image. This edge detector will detect the boundary of optic disc.

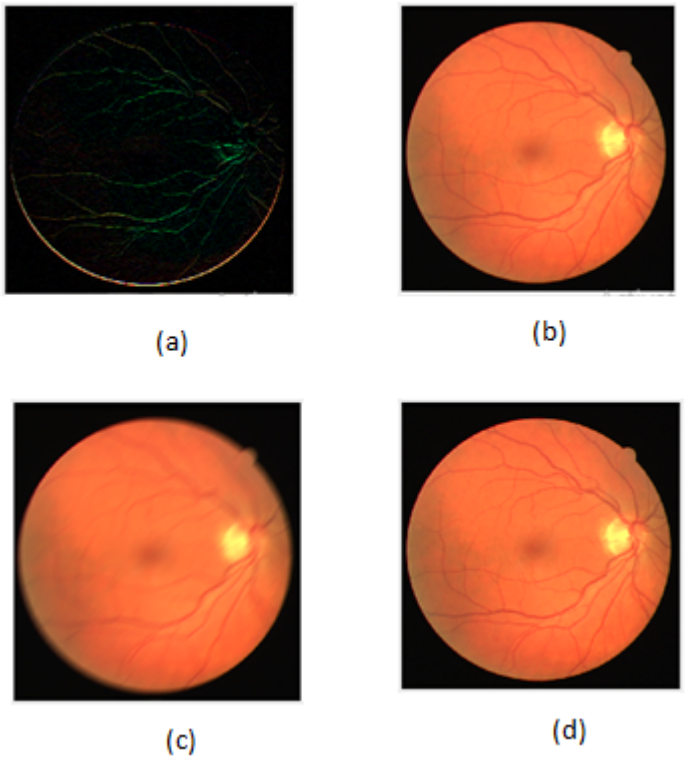

Figure 5.3: Output obtained with different filters.(a) Laplacian (b) Average (c) Motion (d) Gaussian

5.3.2 Elimination of Anatomical Structures

OD and blood vessels are known as anatomical structures of RFIs. The extraction of these two anatomical structures are done differently as described in Chapters 4. The OD detected image obtained by the method described in Chapter 4 is combined with the edge image obtained by employing Sobel edge detector after Gaussian filtering.

In order to completely eliminate OD, a Circular Hough Transform (CHT) is utilized. The CHT estimates the center and radii of the circular objects in the image. For better results before employing CHT, image is dilated with a disc shaped structuring element of size 35. This operation will fill up the gaps or holes of OD portion.

The result obtained in this stage is combined with the blood vessel extracted image obtained by the method described in Chapter 4 to produce a mask. This

mask is then subtracted from all the three planes (R,G,B) of the original image to produce image without blood vessels and optic disc. This image act as the input to the classifier for classifying normal and abnormal RFIs.

The results obtained with a normal RFI is shown in Figure 5.4. Figure 5.4(a) shows the input image. Figure 5.4(b) shows the preprocessed image. Figure 5.4(c) gives the image after removing the blood vessels. Figure 5.4(d), (e) and (f) shows the preprocessed luma plane image, OD edge image and OD image after CHT is applied respectively. By adding the extracted blood vessels and the OD detected image pixel by pixel a mask is generated which is shown in Figure 5.4(g). The image void of blood vessels and OD is shown in Figure 5.4(h).

The corresponding results obtained with an image containing pathological lesions is shown in Figure 5.5. Along with the blood vessels and the OD, the proposed system also detects the edges of the pathological lesions, which is actually an undesirable one. But it is observed that the detection of the edges of the pathological lesions is not affecting the end results. So no further effort is made to suppress the detection of the edges of pathological lesions.

5.3.3 Classification

Bag of Visual Words model is used to classify the RFIs into normal and abnormal ones. An image in this model is represented as a group of self governing local descriptors. Then these descriptors are quantized by histogram vector. The color features have revealed enormous impact in grouping the RFIs. Therefore it is added as a feature for the formation of the BoVW. Usually there are two steps in BoVW. Finding a collection of descriptors from a group of training images is the first step. To obtain the feature set, a retinal image is separated into smaller tiles with dense sampling technique. Every local patch has a descriptor. This descriptor will map a point into a large dimensional feature space. The SURF features interest areas are discovered in this work. The SURF features are acquired from the blood vessel as well as OD removed RFIs.

The second step is construction of a visual vocabulary. It is done by grouping the separated characteristics from the training set. K-means clustering algorithm is used for this purpose. The feature descriptors are obtained and then allocated to the nearest visual vocabulary when an image is given. Hence, each image is represented using a histogram of the occurrences of each possible word from a given vocabulary. This is then employed as the descriptor vector for training the classifier.

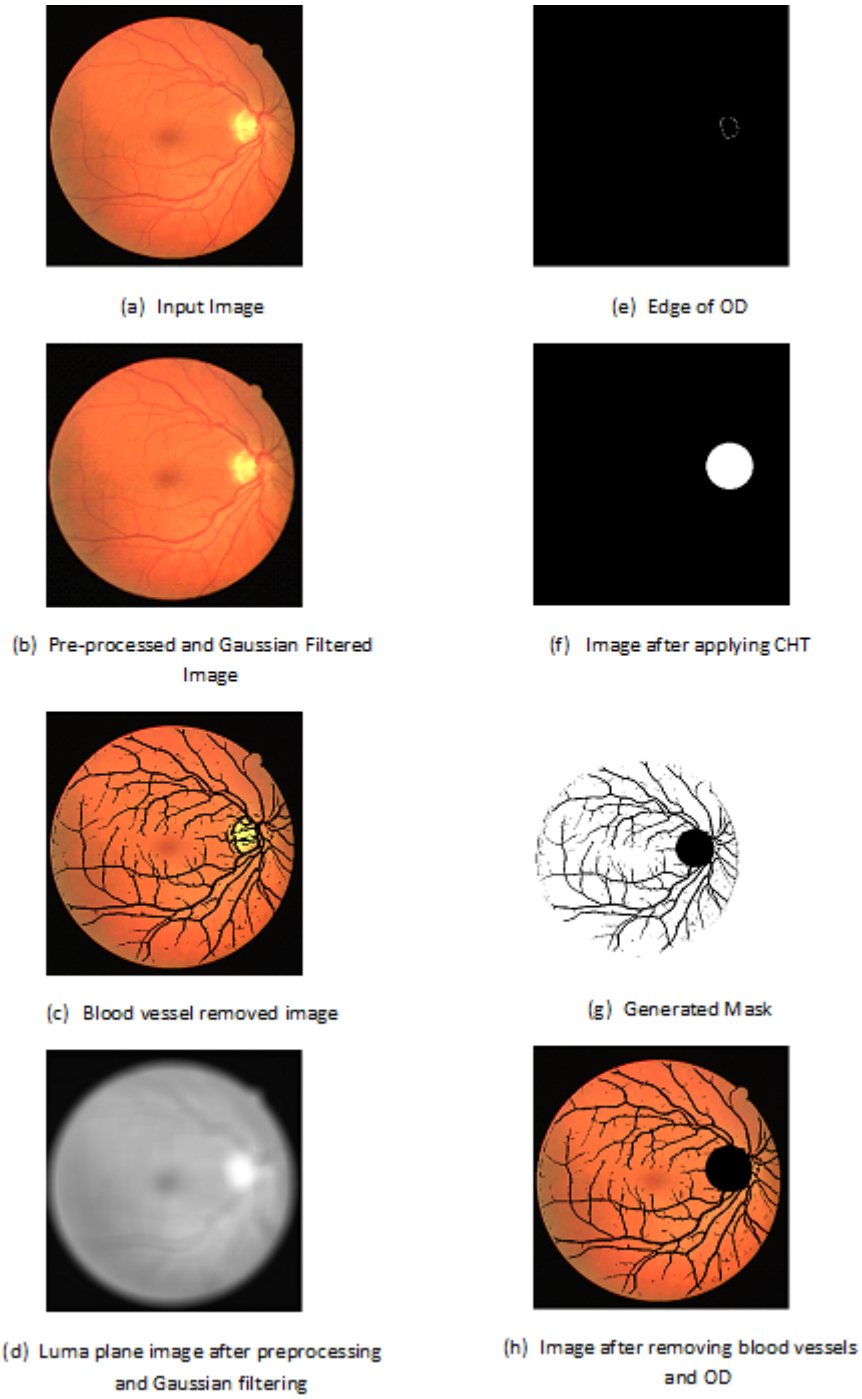

Figure 5.4: Results obtained with a normal RFI as input.

5.4 Results

The performance of the model is established using e-Ophtha database and images collected from a local hospital.

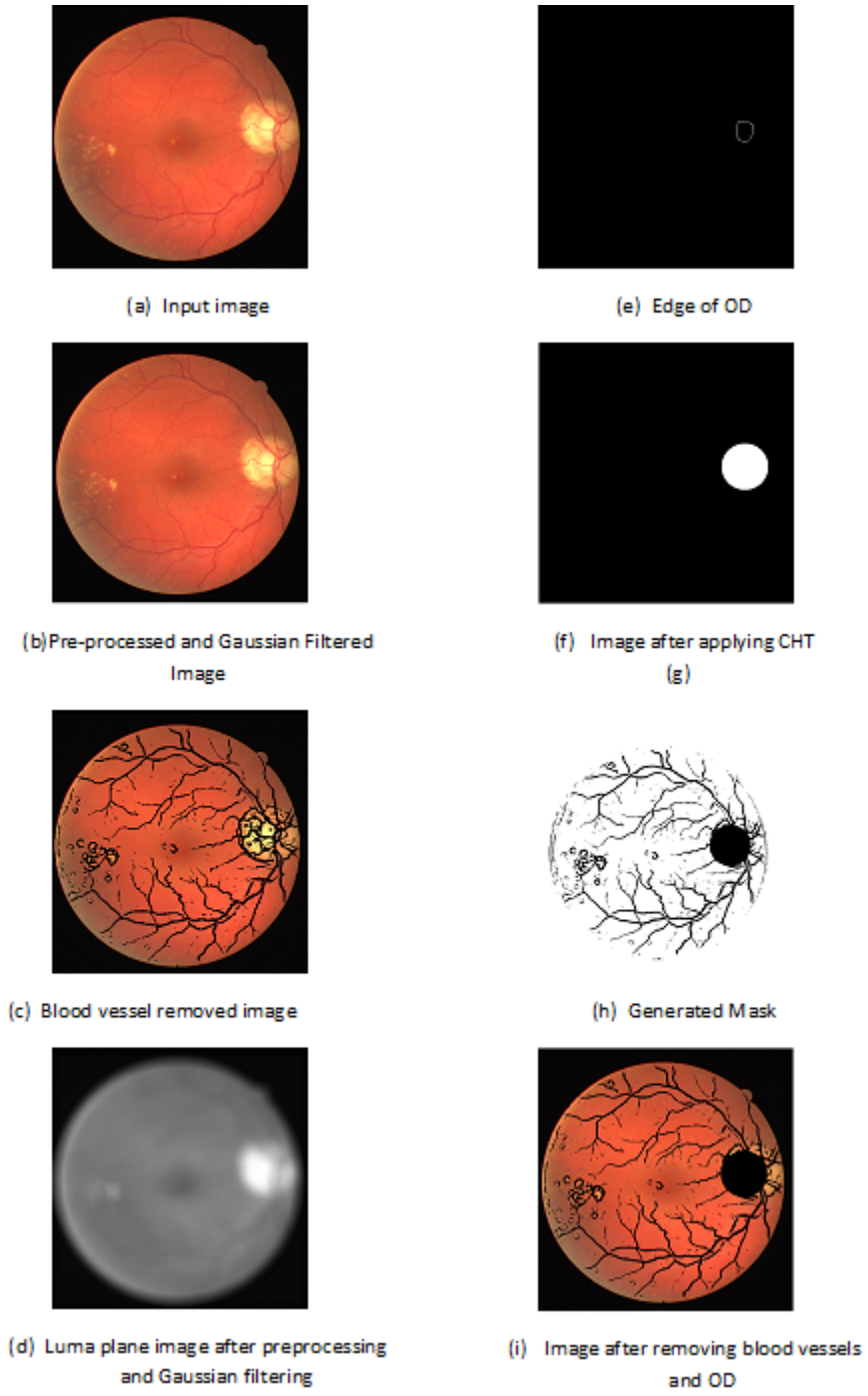

Figure 5.5: Results obtained when a RFI with pathological lesions is used as input.

5.4.1 e-Ophtha

This data base is color fundus images. This database can be utilized for scientific research especially in DR. This database contains 2 folders. One for images with exudates namely e_ophtha_EX and the other namely e_ophtha_MA contains images with microaneurysms. The $e_ophtha_EX$database consists of 82 RFIs

with 35 healthy and 47 pathological retinal images. The e_ophtha_MA data base consists of 381 images. Out of this 381 images, 148 images contains MAs or small hemorrhages and the rest 233 contains no pathological lesions. Images of this database are acquired with different resolutions [193].

5.4.2 Data from Local Hospital

Twenty five images from a local hospital are collected. This images consists of pathological and healthy images. These images are acquired at different illumination conditions and by different persons. An expert ophthalmologist helped to classify the images into 4 categories. First group that contains only healthy images. Second group contains images with micoaneurysms. Third and fourth contains images with exudates and hemorrhages (HMs) respectively.

The distribution of e-Ophtha and local datasets are given in Table 5.1

Table 5.1: Distribution of data

Dataset	Normal	MAs	EXs	HMs
e-Ophtha	268	148	47	-
Local	11	6	4	4

In this work, the database is alienated into two groups for 10 fold cross validation. 1. a training group comprising 90% of images from the database and 2. a validation group having 10% of images from the dataset. The confusion matrix obtained for the proposed approach for different datasets are tabulated in Table 5.2 and 5.3.

Table 5.2: Confusion matrix with e-Ophtha database

e-Ophtha

		Actual		
	-	EXs	MAs	Normal
Predicted	EXs	0.92	0.13	0
	MAs	0.08	0.87	0
	Normal	0	0	1

Table 5.3: Confusion matrix with local data

Local Data

Actual					
Predicted	-	EXs	MAs	HMs	Normal
	EXs	0.89	0.12	0.05	0
	MAs	0.07	0.86	0	0
	HMs	0.04	0.02	0.95	0
	Normal	0	0	0	1

From the confusion matrix we can calculate Sensitivity (SE)/Recall/True Positive Rate (TPR), Accuracy (ACC), Specificity (SP), Precision (PR) and F1-Score using the formulas (2.1) to (2.5) given in Chapter 2. The values obtained for these parameters using e-Ophtha dataset and images collected from local hospital are given in Table 5.4 and Table 5.5.

Table 5.4: PR, SE, ACC, F1-Score, and SP Values obtained with e-Ophtha dataset while classifying EXs, MAs, and Normal eye.

	EXs	MAs	Normal
PR	0.8762	0.9158	1
SE	0.92	0.87	1
ACC	0.93	0.93	1
F1-Score	0.8976	0.8923	1
SP	0.935	0.96	1

Table 5.5: PR, SE, ACC, F1-Score, and SP Values obtained with local dataset while classifying EXs, MAs, and Normal eye.

	EXs	MAs	HMs	Normal
PR	0.8396	0.9247	0.9406	1
SE	0.89	0.86	0.95	1
ACC	0.93	0.9475	0.9725	1
F1-Score	0.8641	0.8912	0.9453	1
SP	0.9433	0.9767	0.98	1

The average values obtained for these evaluation parameters are given in Table 5.6.

Table 5.6: Average Values of PR, SE, ACC, F1-Score and SP

		EXs	MAs	HMs	Normal
Average Values of	PR	0.8579	0.9203	0.9406	1
	SE	0.905	0.865	0.95	1
	ACC	0.93	0.9388	0.9725	1
	F1	0.8809	0.8918	0.9453	1
	SP	0.9392	0.9684	0.98	1

From the parameter values obtained, it is evident that the method produces very promising results. Particularly, precision, recall, accuracy, F1-Score, and specificity values associated with normal case is unity. This means that this classifier correctly detects the normal images.

As far as the average accuracy values are concerned, they are greater than or equal to 0.93, 0.938, 0.972, and 1 for EXs, MAs, HMs, and normal eye respectively. This high values of accuracy indicates that the number of correctly classified cases is pretty good. But, the costs of having a mis-classified actual positive (or false negative) is not considered while calculating the accuracy value. Recall shall be the model metric used to select best model when there is a high cost associated with false negative. The average recall values obtained for our classifier are greater than 0.90, 0.86, 0.95, and 1 for EXs, MAs, HMs, and normal eye respectively. These high values of recall indicates that the cost of false negative is very low. As far as the cost of false positive is concerned, precision is the good measure. The average precision values obtained for our classifier are greater than .85 for EXs, .92 for MAs and 0.94 for HMs. Its value is 1 for normal eye. From these high values of precision we can conclude that the costs of false positive is also low. Accuracy works best if false positives and false negatives have similar cost. But in our case, the cost of false positives and false negatives are different. So it is better to look at both Precision and Recall. F1-score is the measure that takes both false positives and false negatives into account. F1-score values obtained for our classifier are greater than 0.88 for EXs, 0.89 for MAs, 0.94 for HMs and 1 for normal eye. Specificity is a measure of true negative rate. This metric is often used in cases where classification of true negatives is a priority. The average values obtained from our classifier for this metric are greater than 0.93, 0.96, and 0.98 for EXs, MA, and HMs respectively where as it is 1 for normal eye. These values are very close to the best specificity value which is equal to 1.

From the confusion matrix we can observe that mis-classification is only within the abnormal cases. For example, in some cases exudates are misclassified

either as MAs or HMs. Similar is the case for MAs and HMs also. But none of the abnormal cases are classified as normal and vice-versa. Hence this classifier can be used as a binary classifier which classifies normal and abnormal images perfectly. So in that case we are getting 100% classification accuracy.

5.5 Conclusion

Most of the existing algorithms demands surplus pre- and/or post- processing phases for recognizing various features in retinal fundus images. Also, some of the previous algorithms requires manual feature extirpation stages to sort the features in RFIs. In this effort, BoVW model is exploited to develop an easily manageable and automated diagnosis system. This approach can be used to differentiate normal and abnormal RFIs. No manual feature extraction stages are needed. The proposed approach can provide ophthalmologists a feasible, efficient, and time-saving way of DR detection. The BoVW model along with SURF feature descriptor demonstrates excellent discriminating capabilities with an accuracy of 100%. This accuracy is achieved when the method is used to differentiate normal and DR affected RFIs. But when used to classify the abnormalities into MAs, EXs, and HMs cases the F1-Score obtained are 0.88, .89%, and 0.94 respectively. So, in summary, we can conclude that this method can be used to detect DR in RFIs, but cannot be used for detecting the severity level of DR.

Chapter 6

Assessment of Diabetic Retinopathy Severity

6.1 Introduction

Till now the algorithm succeeded in detecting the DR with 100% accuracy. But when the classifier introduced in chapter 5 is applied to classify the DR features, it achieved only 86%, 89%, and 95% accuracies for MAs, EXs, and HMs classification. Furthermore, the demarcation of MAs, EXs, and HMs highly depends on the experience of the ophthalmologist. Also the severity of DR depends on a number of other features such as position of abnormal features, color of the abnormal features etc. So it becomes a very difficulty task to predict the severity of DR with an acceptable level of accuracy using the conventional classification methods.

The prevailing DR screening methods are paralyzed by the lack of trained and experienced clinicians. Additionally, these methods are time-consuming. The time lag in rendering results can bring about postponed or missed treatments, lost follow-ups, and miscommunication- which may double the chance of sight impairment. As per the finding by California Health Care Foundation, among the subjects who were referred to an ophthalmologist by a physician, only 23% are willing to visit an eye specialist. Out of the remaining 77%, 15% were ignorant of the complaint, other 15% did not try for a screening session, another 22% failed to appear for their screening test and 25% refused to take therapy [194]. These statistical facts reveals the necessity for a system to identify and classify the stages of DR quickly and accurately with confidence and direct the patients to ophthalmologist if needed. This will help medical practitioners concentrating on DR cases to make use of their time productively and inevitably treat more number of DR affected cases in a timely manner.

With proceeding development in the field of computing facilities and accessibility of best quality data sets, artificial intelligence (AI) systems based on deep learning (DL) can employ algorithms to yield much reliable and expeditious diagnosis of DR.

The upcoming Sections in this Chapter are organized as follows. Section 6.2 describes the DR severity assessment through the use of the pre-trained EfficientNetB4 network. The results obtained are illustrated in Section 6.3. Conclusions are given in Section 6.4.

6.2 DR Severity Assessment

The mechanism of establishing whether or not the candidate is affected by DR from the given dataset of the candidate's RFIs is known as DR prediction. We achieved 100% prediction accuracy with the conventional BoVW classifier. Now the remaining task is the assessment or grading of DR. i.e., the mechanism of unearthing the severity level of DR from the RFIs. A clinically followed protocol for DR grading is illustrated in Table 6.1. This Table shows the DR grades and its clinical definitions.

Table 6.1: A typical scale for DR grading [21]

Class	DR Types	Clinical Features
0	Normal	No abnormal lineaments
1	Mild NPDR	Found MAs
2	Moderate NPDR	Maximum number of MAs, Exs, and HMs
3	Severe NPDR	All abnormal features in four quadrants
4	PDR	All abnormal features with new blood vessel formation

A sample set of DR images is given in Figure 6.1 which shows all types of DR presented in Table 6.1.

6.2.1 Stages of Diabetic Retinopathy

The different stages of DR as mentioned in Table 6.1 are as follows.

1. *Mild nonproliferative retinopathy:* This is the first stage of DR. At this stage microaneurysms- dilated capillaries that have the appearance of a red dot or balloon- are often detected. The most crucial fact at this stage is that microaneurysms do not disturb vision and as a consequence often go unattended.

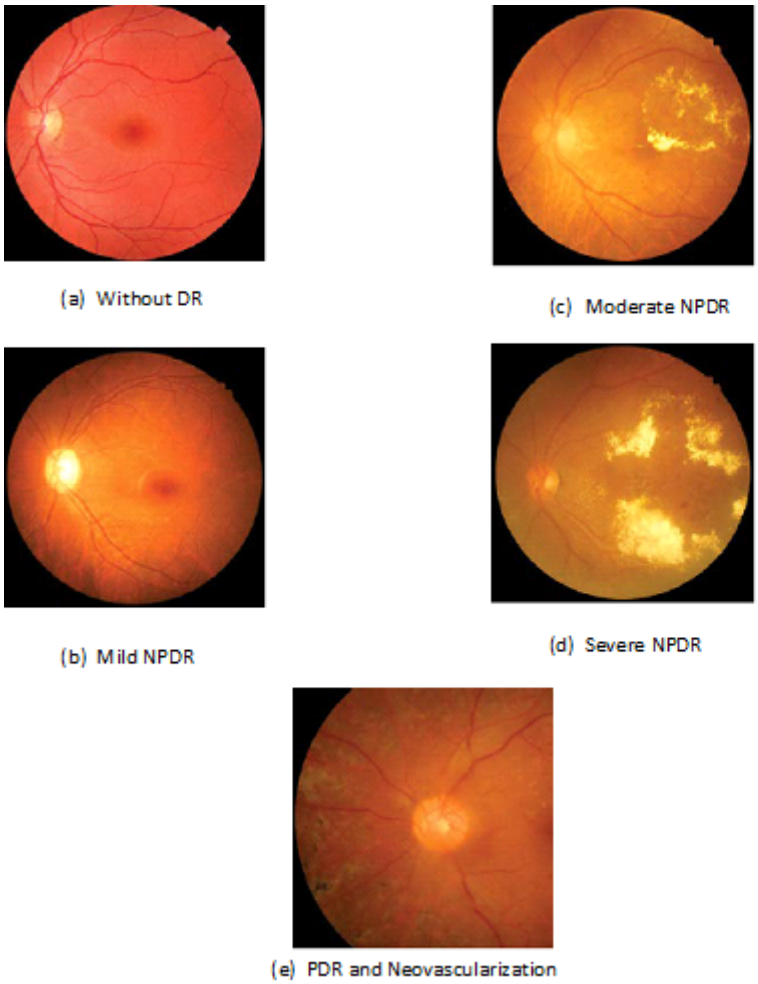

Figure 6.1: Examples of DR affected retinal images

2. *Moderate nonproliferative retinopathy:* When the patient reach this stage maximum number of

   (a) microaneurysms

   (b) exudates - leaked out fluid (made of cells proteins, and solid materials) from blood vessels into neighbouring tissue

   (c) hemorrhages- leakage of blood from tiny blood vessels- appear in the eye.
   At this level the retinal blood veins may bulge and deplete their capability to transport blood.

3. *Severe nonproliferative retinopathy:* At this stage, a substantial number of retinal blood vessels are blocked. Consequently, the necessary blood flow to the retina severely decreases. Eventually, the retina will start to transmit signals, asking the brain to develop new blood vessels.

4. *Proliferative retinopathy:* This stage is the most complicated situation of DR. At this stage new blood vessels start to grow. Unfortunately, these weak and abnormal blood vessels can cause blood leaking into the eye. This may lead to vision problems and potentially blindness.

The core of the DR assessment technique going to be discussed in this Chapter is based on a deep learning approach particularly known as transfer learning. Transfer learning is a widely used and devastating approach to DL on image dataset that uses a pre-trained network. A pre-trained network is a retained network that was already trained on a huge dataset, particularly on a large-scale image classification assignment. Provided this pioneer dataset is huge and general enough, then the spatial hierarchy of parameters acquired by the pre-trained network can productively act as a comprehensive representation of the visual world. Accordingly its parameters are believed to be useful for various computer vision tasks, even though these new assignments may involve entirely different classes than those of the original task. Such transferability of learned parameters across various tasks is a principal advantage of DL as against many decrepit shallow-learning methods and it makes DL very effectual for classification jobs.

6.2.2 Data

The data required for training the model has been taken from Kaggle-one of the biggest and most diversified data analytic communities in the world. The dataset consists of about 10GB of data. The distribution of data in the Kaggle dataset is illustrated in the bar graph shown in Figure 6.2. It contains a total of 3662 retinal fundus images from all classes of DR. Out of this 3662 images 1805 images belongs to class0 case, 370 images belongs to class1 case, 999 images belongs to class2 case, 193 images belongs to class3, and remaining 295 images belongs to class4 case.The images are of different size and collected from rural areas taken under different illumination conditions. So the data requires pre processing before feeding as input to the DL model.

6.2.3 Deep Learning

As mentioned earlier in this chapter transfer learning is used to classify the retinal images as per their severity level.

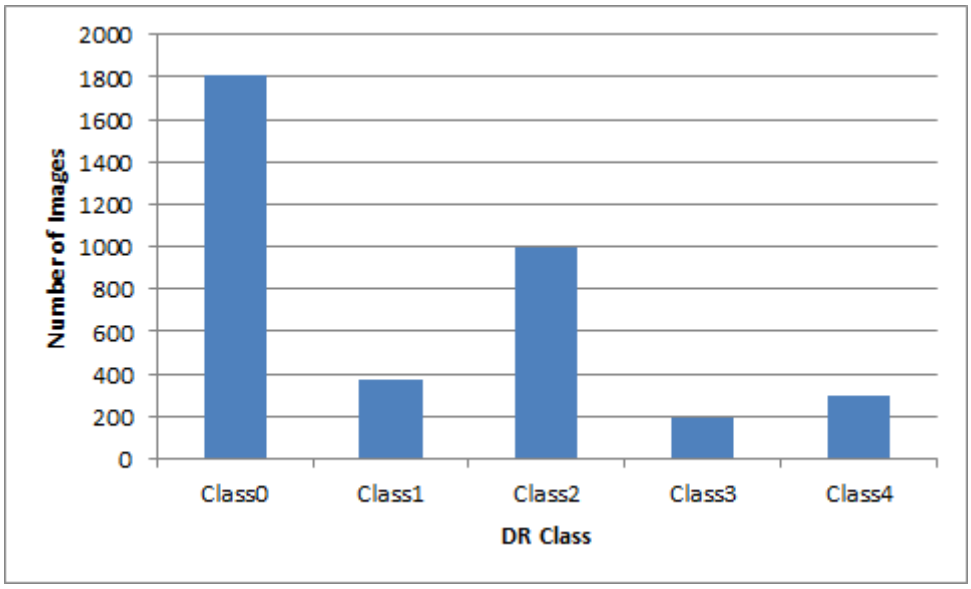

Figure 6.2: Distribution of data obtained from Kaggle dataset.

6.2.3.1 Selection of Network

Various pre-trained networks like Xception, Inception V3, ResNet50, VGG16, VGG19, EfficientNetB0-B7 etc are available for transfer learning. Among the available pre-trained models EfficieentNetB4 is selected in this work because of the following reasons.

Convolutional neural networks are generally designed at a particular resource cost. In order to gain more accuracy, they are scaled up when more resources are made available. Increasing the CNN width, or depth, or employ high resolution input image for training and evaluation are the conventional methods for scaling the models. Even though these conventional practices improve the accuracy of the classifier, they usually demands heavy manual tuning, and even with that frequently return suboptimal performance.

EfficientNet utilize a model scaling technique that employs an uncomplicated but very efficient compound coefficient to scale up CNNs. Different from conventional methods that arbitrarily scale depth, width, and resolution, EfficientNets uniformly scales all dimension with a fixed combination of scaling coefficients as illustrated in Figure 6.3. This scaling method and current development on automated machine learning (AutoML) powered EfficientNets to surpass other networks with up to 10 times better efficiency.

The initial step in the compound model scaling approach is to accomplish a grid search under a fixed resource constraint. Hence, a relation between various

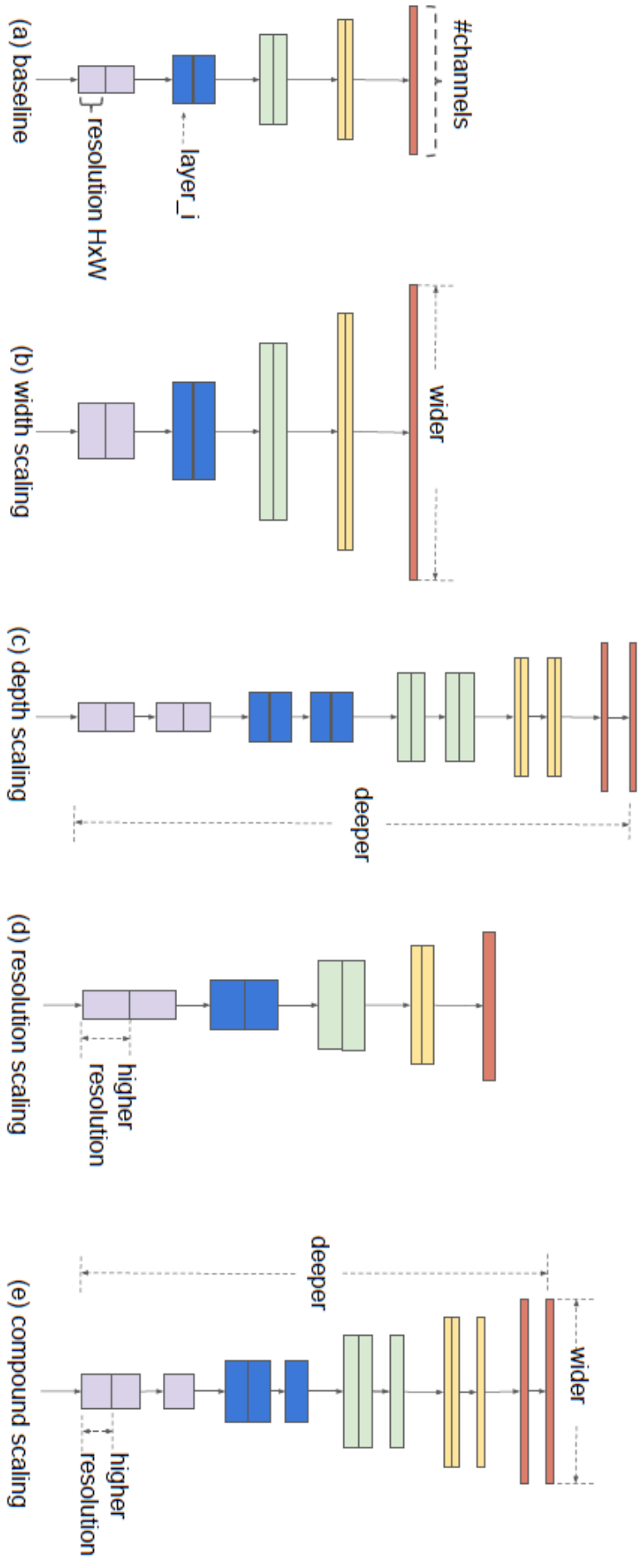

Figure 6.3: Compound scalin [195]

scaling dimensions of the baseline network is explored and the appropriate scaling coefficient for width, depth, and resolution are determined. These coefficients are then applied to scale up the baseline network to the desired computational budget or target model size. A comparison of different scaling methods is shown in Figure 6.3.

The success of model scaling also depends largely on the baseline network. So a baseline network is developed by applying a neural architecture search employing the AutoML mobile neural architecture search framework. This framework optimizes both accuracy and efficiency(FLOPS). The resulting baseline architecture uses Mobile inverted Bottleneck Convolution (MBConv). This baseline network, shown in Figure 6.4, is scaled up to achieve a family of models, known as EfficientNets (B0 - B7).

So the first and foremost reason for the selection of EfficientNet is its much smaller size compared with other models. At the same time EfficientNet provides a higher imagenet accuracy. For example, even if ResNet50 has 23,534,592 parameters in total, it still fails to achieve the accuracy offered by the smallest EfficientNet, i.e. EfficientNetB0, which has only 5,330,564 parameters in total. The second advantage of EfficientNets is that it scales more effectively by meticulously balancing the network width, depth, and resolution there by providing a better performance. Figure 6.5 and 6.6 demonstrates the performance of EfficientNets with various other pre-trained networks in terms of number of parameters (in Millions and number of FLOPS in Billions). From Figure 6.5 and 6.6 we can conclude that a mobile size EfficientNet model can be scaled up very efficiently surpassing the state-of-the-art accuracy with an order of magnitude fewer parameters and FLOPS on commonly used transfer learning datasets [195].

Among the different EfficientNet models available, EfficientNetB4 is found to be a good choice due to its high accuracy and small size. Even though higher models of EfficientNet gives better performance than the selected EfficientNetB4, the number of parameters of these models also increases rapidly. Thus considering the trade-off between complexity and accuracy EfficientNetB4 is selected.

6.2.3.2 Training the Network

Generally there exists two methods to use a pre-trained network. 1. Feature extraction and 2. Fine-tuning

1. Feature extraction

Feature extraction is carried out using the representations acquired by a

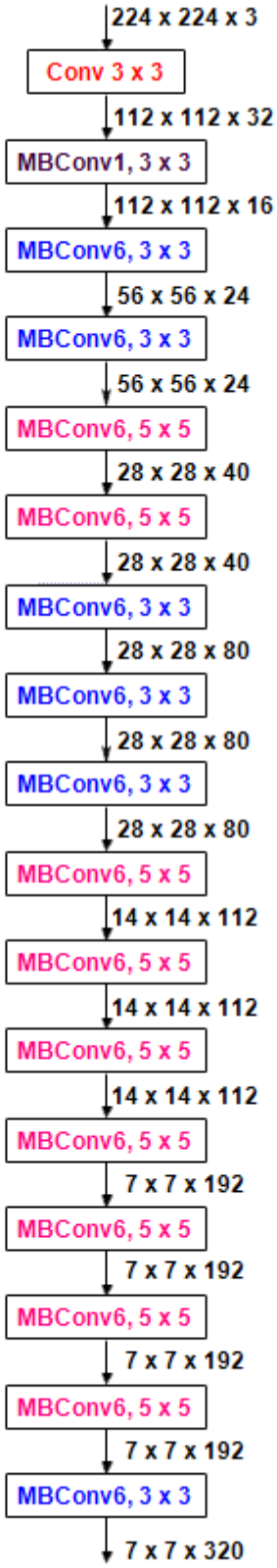

Figure 6.4: Architecture of EfficientNet baseline network

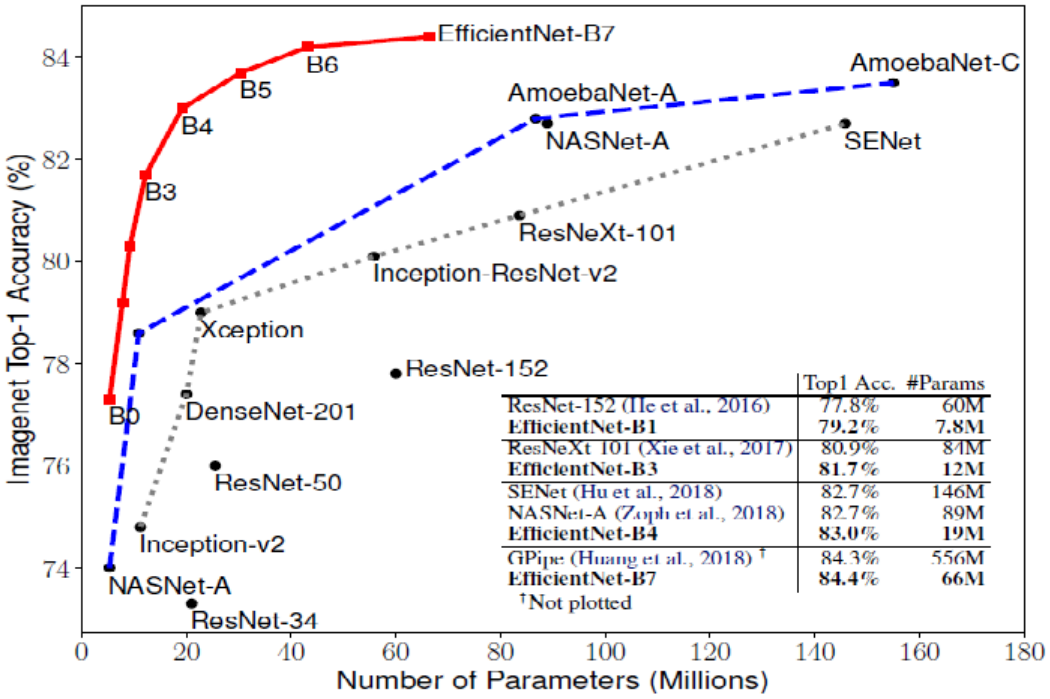

Figure 6.5: Comparison of parameters Vs accuracy of different Network [195]

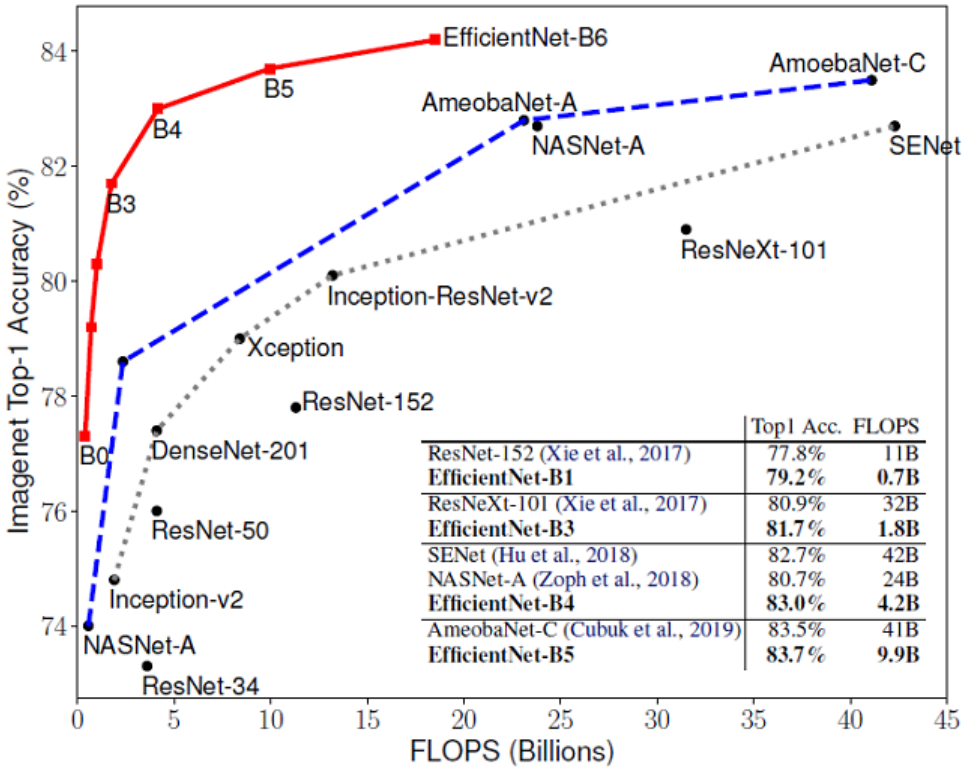

Figure 6.6: Comparison of FLOPS Vs accuracy of different network [195]

previous network to bring out interesting characteristics from current samples. These characteristics are then passed through a new classifier, which is

taught from scratch.

CNNs employed for image categorization include two parts: they commence with a succession of pooling and convolution layers, and they build up to a densely connected classifier. The former part is known as the convolution base (conv_base) of the model. In the case of CNNs, feature extraction consists of getting the conv_base of an formerly trained network, passing the new data through it, and preparing a new classifier atop the conv_base as illustrated in Figure 6.7.

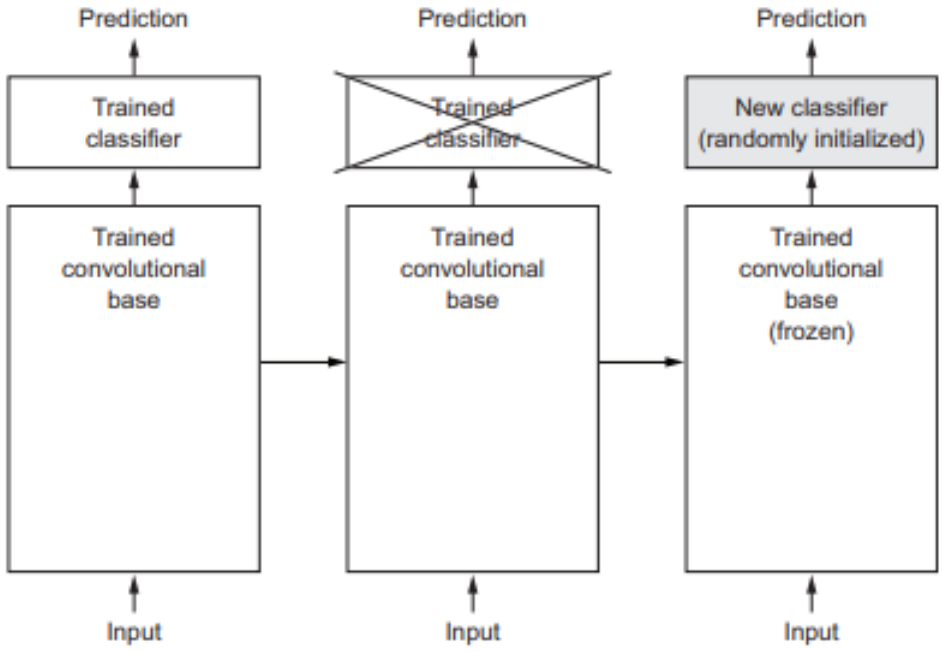

Figure 6.7: Swapping classifiers while keeping the same convolution base [196]

The reason for reusing only the convolution base is that the features acquired by the conv_base are prone to be more common and hence more capable of being used again: the attribute maps of CNNs are existence maps of common notions over a picture, which is useful irrespective of the computer-vision task in place. On the other hand, the features learned by the classifier will definitely be particular to the group of classes on which the model was trained - they will only hold facts about the presence likelihood of this or that class in the whole picture. In addition, representations appearing in densely connected layers bygone contain any information about where objects are positioned in the input image: these layers drop the notion of space, however the object position is still embodied by convolutional feature maps.

After taking the model, i.e. conv_base, add dense layers atop. Now run the entire thing end to end on the input data.

2. Fine-tuning

An alternative popular technique for model re-utilization, contrasting to feature extraction, is fine-tuning. Fine-tuning is performed by relaxing a few of the top layers of a fixed model base used for feature extraction, and collectively training both the freshly introduced part of the model and some of the top layers of the base model. This is termed fine-tuning because it faintly modifies the more abstract features of the model being reused, so as to make them more admissible for the current problem.

It's only practicable to fine-tune the atop layers of the convolutional base once the classifier on top has already been trained. If the classifier is untrained, then the error signal radiating back through the network during training will be too large, and the representations formerly acquired by the layers being fine-tuned will be ruined. Accordingly the algorithm for fine-tuning a network are as follows:

Algorithm 5 Fine-tuning a network

1: Introduce a bespoke network atop of a previously trained base network.
2: Hold the weights of the base network.
3: Coach the bespoke network added.
4: Release some of the top layers in the base network so that their weights can be modified.
5: Collectively train these released layers and the bespoke network.

We could fine-tune the whole convolution base. However, we should take care of the following facts

(a) Starting layers in the convolutional base identify more common and reusable attributes, whereas top layers identify more specific features. It's more convenient to fine-tune the more specific attributes, since these are the ones that ought to be re-purposed on our new task. There would be rapid diminishing returns in fine-tuning bottom layers.

(b) The more parameter we are training, the higher the chance of overfitting.

Since fine-tuning approach not only train the custom network added, but also some of the top layers of the base network, the network will adapt more to the problem at hand giving better results. So fine-tuning approach is adopted in this work to train the pre-trained EfficientNetB4 network.

6.3 Results

The results obtained during training are illustrated in this section.

6.3.1 Results without Data Augmentation

First the training is carried out only with the data available, i.e. without incorporating the data augmentation technique. We plotted the the loss of the model over the training and validation data during training and is shown in Figure 6.8. The blue curve indicates training loss and the yellow curve indicates validation loss.

From the plot we can observe that even though the training loss is decreasing with epochs, the validation loss gets almost saturated after 20 epochs. There is a large difference between training loss curve and validation loss curve. For a perfect classifier the validation loss curve should closely track the training curve. Because we have relatively few training samples($\approx$ 2747 images), over-fitting will be our number one concern. One of the methods to reduce over-fitting is data augmentation.

6.3.2 Result with Data Augmentation

Over-fitting is the result of inadequate amount of samples to learn from. Data augmentation is a technique to generate fresh samples from the samples in-hand, by modifying the samples via various random transformations that produce plausible-looking images. The objective is that during training, model will never come across the exact same picture more than once. This aids to introduce the model to more attributes of the data and conclude better.

If we train a fresh network employing this data augmentation technique, the network will never view the identical input twice. However, the inputs it encounter are still highly inter-correlated, since they originate from a small amount of initial images. So data augmentation could not produce new information, but could only

Figure 6.8: Loss without data augmentation.

rearrange existing information.

Data augmentation is achieved by performing rotation, shift, shear transformations, zooming, or flipping the images. A few samples of the augmented images is given in Figure 6.9.

The model after adding two dense layers at the top looks like as shown in Figure 6.10.

As evident from the model the base network of EfficientNetB4 has 17,673,816 parameters. The classifier added at the top has 460,293 parameters. The first dense layer added has 256 outputs where as the top most dense layer (second dense layer) has only 5 outputs. This five outputs corresponds to the five severity levels of DR. As we can see from the model, the total trainable parameters is 18,008,909 which is very large. But since we are using transfer learning using fine-tuning approach, we first freeze the efficientnet-b4 base network and train only the layers we added. So in that case we need to train only the 460,293 parameters. Now we unfreeze the last layer of efficientnet-b4 base network and jointly train this layer and the added

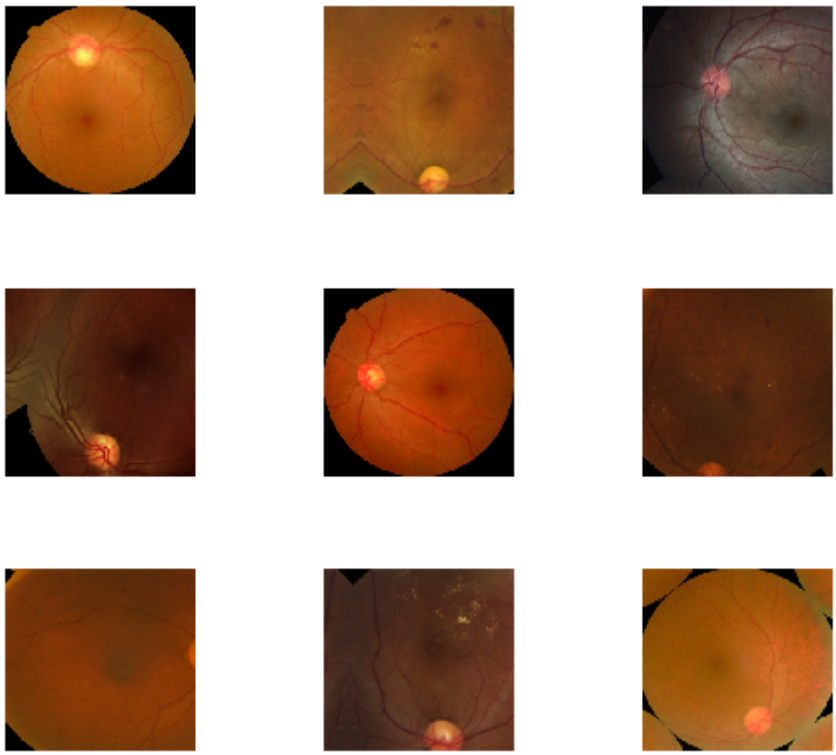

Figure 6.9: Samples of augmented images.

dense layers together. This step requires training of 5,736,697 parameters which is small compared with the 18,134,109 total parameters. The model after unfreezing the top layer of efficientnet-b4 base network looks like as shown in Figure 6.11.

The loss and accuracy plot of the model are given in Figure 6.12 and 6.13 respectively. As evident from the plots we are no longer over-fitting. The training loss curves are closely tracking the validation loss curves.

Similarly, we have plotted the accuracy curves also. It is also observed that the training accuracy curves are closely tracking the validation accuracy curves. Our model produces accuracy value greater than 0.9. It will be difficult to go any higher accuracy just by training our model, because of the limitation in the amount of data to work with.

```
# EfiicientNetB4 Summary with output layers added

Model: "sequential_1"
_________________________________________________________________
Layer (type)                 Output Shape              Param #
=================================================================
efficientnet-b4 (Model)      (None, 1792)              17673816
_________________________________________________________________
dense_1 (Dense)              (None, 256)               459008
_________________________________________________________________
dense_2 (Dense)              (None, 5)                 1285
=================================================================
Total params: 18,134,109
Trainable params: 18,008,909
Non-trainable params: 125,200
_________________________________________________________________
```

Figure 6.10: Model after adding two dense layers at the top of efficientnet-b4 base network

```
### Fine Tuning. Making one layer of base trainable

Model: "sequential_6"
_________________________________________________________________
Layer (type)                 Output Shape              Param #
=================================================================
efficientnet-b4 (Model)      (None, 1792)              17673816
_________________________________________________________________
dense_17 (Dense)             (None, 256)               459008
_________________________________________________________________
dense_18 (Dense)             (None, 5)                 1285
=================================================================
Total params: 18,134,109
Trainable params: 5,736,697
Non-trainable params: 12,397,412
```

Figure 6.11: Model after unfreezing the top layer of efficientnet-b4 base network

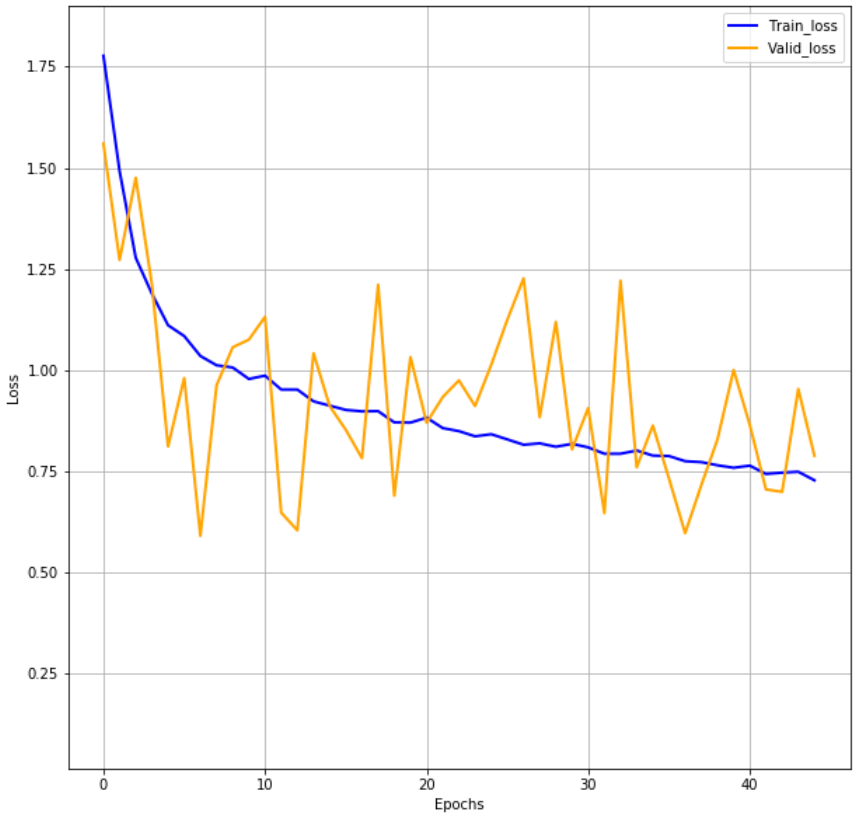

Figure 6.12: Loss curves with data augmentation.

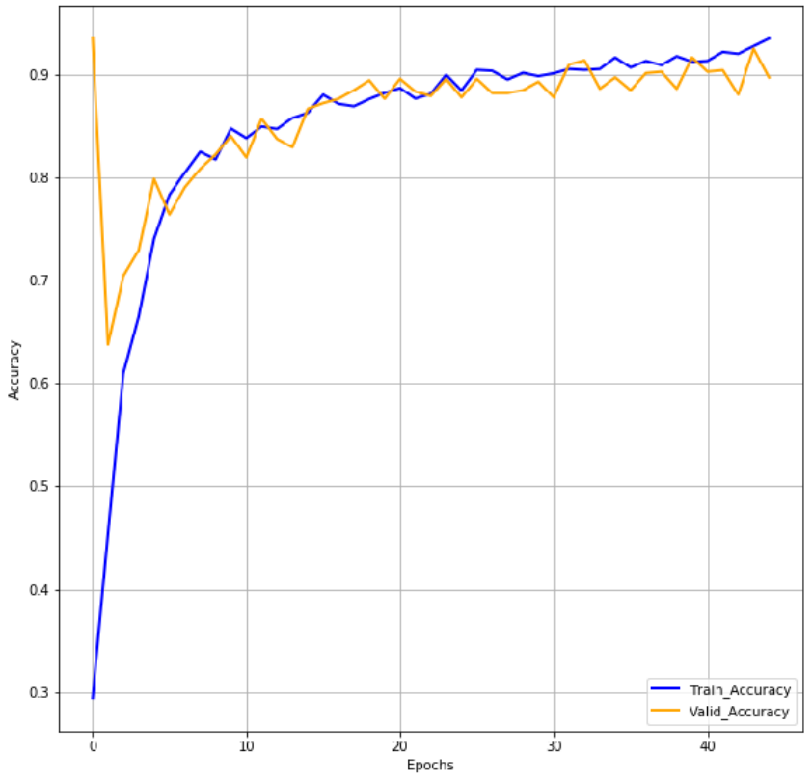

Figure 6.13: Accuracy curves with data augmentation.

```
Confusion Matrix

[[410   2  12   0   0]
 [  8  79   7   2   0]
 [ 18   5 235   9   3]
 [  0   1   6  42   0]
 [  4   3   2   2  65]]

Precision, Recall and F1-Score

              precision    recall  f1-score   support

      Class0       0.932     0.967     0.949       424
      Class1       0.878     0.823     0.849        96
      Class2       0.897     0.870     0.883       270
      Class3       0.764     0.857     0.808        49
      Class4       0.956     0.855     0.903        76


   macro avg       0.885     0.875     0.878       915
weighted avg       0.909     0.908     0.908       915
```

Figure 6.14: Final confusion matrix, precision, recall, and F1-score values obtained

We also obtained the confusion matrix and other parameters such as Precision, Recall and F1-Score. The result obtained for this parameters are given in Figure 6.14.

Precision value gives answer to the question : What proportion of predicted Positives is actually Positive? We can see that maximum precision value (0.956) is achieved for class4 and minimum value (0.764) for class3. The precision values obtained for class0, class1, and class2 are 0.932, 0.878, and 0.897 respectively. The classifier's overall precision (macro average) is 0.885 and weighted average value of precision is 0.909.

Recall, an another very useful parameter, answers the question: What volume of actual Positives is exactly classified? We can see that maximum recall value (0.967) is achieved for class0 and minimum value (0.823) for class1. The recall values obtained for class2, class3, and class4 are 0.870, 0.857 and 0.855 respectively. The macro average and weighted average values of recall is 0.875 and 0.908 respectively.

It is evident that the algorithm gives high values for both precision and recall. To estimate the performance of the classifier F1-Score is also calculated,

which is a function of both precision and recall. Since F1-Score is the harmonic mean of precision and recall it always lies somewhere in between the two, but gives more weight to lower value. We can see that maximum F1-Score (0.949) is achieved for class0, giving higher weight to lower valued precision in this case and minimum value (0.808), giving more weight to lower valued precision for class3. The F1-Score obtained for class1, class2, and class4 are 0.849, 0.883, and 0.903 respectively. The overall F1-Score is 0.878 and weighted average values of F1-Score is 0.908. The overall accuracy obtained for the classifier is 91%, which is very much promising. The accuracy obtained from the classifier for different classes are shown in Table 6.2.

Table 6.2: Accuracy obtained for diffrent classes.

Class 0	Normal	0.952
Class 1	Mild NPDR	0.97
Class 2	Moderate NPDR	0.932
Class 3	Severe NPDR	0.978
Class 4	PDR	0.985

From the accuracy values we can see that the classifier classifies the normal case with 95.2% accuracy. But, we have already achieved 100% accuracy using BoVW classifier to classify normal and abnormal cases. So if that classifier classify an image as normal, there is no need to proceed to this severity assessment. This severity classifier classifies the mild NPDR with 97% accuracy. This is very important because if we are able to detect the DR at its early stage, the treatment becomes more effective. The accuracy achieved for moderate NPDR is 93.2% which is a relatively low value compared with accuracy values obtained for other stages of the disease. For severe NPDR and PDR stages the classifier accuracy obtained were 97.8% and 98.5% respectively. The novelty of the proposed work lies in the fact that it can classify normal and abnormal images with 100% accuracy. Also, the severity level of the abnormal cases are classified with an average substantial accuracy of 96.33%.

In order to confirm the performance of the classifier, the kappa score also known as Cohen's kappa, is also calculated from the confusion matrix using (6.1) [197].

$$\kappa = \frac{A - CA}{1 - CA} \tag{6.1}$$

where A is Agree, CA is Chance Agree.

Cohen's kappa, denoted by κ is a resilient statistic and is appropriate for intra-rater and inter-rater reliability assessment. Alike correlation coefficients, it

can vary from -1 to +1. $\kappa = 0$ indicates the degree of agreement that can be counted on random chance. $\kappa = 1$ reflects excellent agreement between the raters. Negative kappa values are uncommon in real life . Like all correlation statistics, the kappa is a balanced quantity and thus is regarded the same across multiple studies.

Cohen suggested the kappa result be interpreted as follows: values ≤ 0 as indicating no agreement and $0.01 - 0.20$ as none to slight, $0.21 - 0.40$ as fair, $0.41 - 0.60$ as moderate, $0.61 - 0.80$ as substantial, and $0.81 - 1.00$ as almost perfect agreement [197].

The kappa score obtained for the classifier is 0.8636, which shows that the classifier can be considered as a perfect classifier.

6.4 Conclusion

In this chapter a DR severity assessment algorithm is described. The algorithm is based on deep learning and it utilizes the pre-trained EfficientNetB4 network for transfer learning. Data augmentation and fine tuning approaches are employed for performing the transfer learning. The loss curves of the classifier shows that the training loss nicely tracks the validation loss. Same is the case for training accuracy also. The performance of the classifier is also evaluated using different parameters such as precision, recall, F1-Score, Accuracy and kappa score. From the values obtained for these parameters it is evident that the proposed classifier is a perfect classifier for classifying the severity levels of diabetic retinopathy.

Chapter 7

Conclusion and Future Scope

The Chapter presents the summary of the work carried out and the conclusions drawn. Important contributions of the work and the scope for further research in this area are presented in this Chapter.

7.1 Image Contrast Enhancement

Conventional image contrast enhancement techniques usually consider small pathological features present in the image as noise and hence these conventional techniques removes these tiny, but wanted, pathological features. The image contrast enhancement algorithm developed in Chapter 3 overcomes this draw back. Fuzzy based image contrast enhancement is employed where image contrast is treated as a qualitative rather than quantitative measure. Rather than applying the thresholding operation directly to the NSCT coefficients, the developed algorithm uses the threshold value to modified membership values of the coefficients. The new NSCT coefficients are obtained using these modified membership values. Hence this algorithm preserves the tiny pathological features present in the image.

7.2 Extraction of Normal Retinal Features

Algorithm presented in Chapter 4 to extract blood vessels from RFIs is based on the famous mathematical morphology. Modified top hat transformation is used at the edge detection step. The problem of containing all tiny ordinary intensity variations in the top hat transformation is eliminated by the use of modified top hat transformation. Also rather than using simple and ordinary structuring elements multistructure element morphology is used. This multistructure elements are produced by gathering several SEs in a single window and hence can detect complex edges. Opening by reconstruction and Connected Component Analysis

with Length Filtering are employed to remove the false edges produced and refine the result. The well known 8-connectivity region growing algorithm is used to localize the optic disk and Fovea regions.

7.3 DR Detection

DR detection algorithm described in Chapter 5 used Bag of Visual Words technique to classify RFIs into normal and abnormal images. Since blood vessels and optic disk are the sources of false positives in the detection of MAs, HMs, and bright lesions they are removed from the RFIs before it is given as input to the BoVW classifier. This classifier classifies normal and abnormal RFIs with 100% accuracy.

7.4 Severity Assessment

Deep learning is employed to detect the severity level of DR present in the RFIs. Transfer learning approach is used by selecting the pre-trained EfficientNetB4. The main aspects considered while selecting the network were number of parameters, accuracy and complexity. The kappa value obtained indicates that the classifier can be considered as a perfect classifier for classifying the severity levels of DR.

7.5 Research Contributions

1. Developed an appropriate contrast enhancement algorithm for retinal fundus images.
2. Developed algorithms to extract blood vessels and localize optic disc & fovea from retinal fundus images.
3. Accurately detected the presence of diabetic retinopathy in retinal fundus images.
4. Assessed the severity of diabetic retinopathy in retinal fundus images.

7.6 Scope for Future Work

A few possible suggestions for future work are presented.

1. The blood vessel extraction method employed in this work is based on gray scale image and it consists of 3 different stages. Colour image based methods can be developed for further improving the accuracy.

2. The deep learning technique used here is transfer learning approach. Instead of using transfer learning approach employing hyperparameter tuning or similar modern techniques, a dedicated network to assess the severity of DR can be developed.

References

[1] M. Herbert and F. Jelinek, "Automated image detection of retinal pathology," *CRC Press Taylor and Francis Group*, vol. 1, p. 384, 2010.

[2] E. Ng, U. R. Acharya, R. M. Rangayyan, and J. S. Suri, *Ophthalmological Imaging and Applications*. CRC Press, 2014.

[3] I. D. Federation, "Idf Diabetes Atlas Ninth," *Dunia: IDF*, 2019.

[4] J. Kanski, "Diabetic Retinopathy, Clinical Ophthalmology," 1997.

[5] D. E. Singer, D. M. Nathan, H. A. Fogel, and A. P. Schachat, "Screening for diabetic retinopathy," *Annals of Internal Medicine*, vol. 116, no. 8, pp. 660–671, 1992.

[6] R. Working Party, "A rotocol for screening for diabetic retinopathy in Europe," *Diabetic Medicine*, vol. 8, no. 3, pp. 263–267, 1991.

[7] D. R. Lairson, J. A. Pugh, A. S. Kapadia, R. J. Lorimor, J. Jacobson, and R. Velez, "Cost-effectiveness of alternative methods for diabetic retinopathy screening," *Diabetes Care*, vol. 15, no. 10, pp. 1369–1377, 1992.

[8] J. C. Javitt, J. K. Canner, and A. Sommer, "Cost effectiveness of current approaches to the control of retinopathy in type I diabetics," *Ophthalmology*, vol. 96, no. 2, pp. 255–264, 1989.

[9] W. Foulds, A. McCuish, T. Barrie, F. Green, I. Scobie, I. Ghafour, E. McClure, and J. Barber, "Diabetic retinopathy in the west of Scotland: Its detection and prevalence, and the cost-effectiveness of a proposed screening programme." *Health Bulletin*, vol. 41, no. 6, p. 318, 1983.

[10] I. Scobie, A. MacCuish, T. Barrie, F. Green, and W. Foulds, "Serious retinopathy in a diabetic clinic: Prevalence and therapeutic implications," *The Lancet*, vol. 318, no. 8245, pp. 520–521, 1981.

[11] J. A. Pugh, J. M. Jacobson, W. Van Heuven, J. A. Watters, M. R. Tuley, D. R. Lairson, R. J. Lorimor, A. S. Kapadia, and R. Velez, "Screening for

diabetic retinopathy: The wide-angle retinal camera," *Diabetes Care*, vol. 16, no. 6, pp. 889–895, 1993.

[12] R. Williams, S. Nussey, and G. Thompson, "Assessment of non-mydriatic photography in detection of diabetic retinopathy," *British Medical Journal (Clinical Research ed.)*, vol. 293, no. 6561, p. 1571, 1986.

[13] C. Sinthanayothin, "Image Analysis for Automatic Diagnosis of Diabetic Retinopathy," Ph.D. dissertation, University of London, 1999.

[14] I. Kavakiotis, O. Tsave, A. Salifoglou, N. Maglaveras, I. Vlahavas, and I. Chouvarda, "Machine learning and data mining methods in diabetes research," *Computational and Structural Biotechnology Journal*, vol. 15, pp. 104–116, 2017.

[15] M. R. K. Mookiah, U. R. Acharya, C. K. Chua, C. M. Lim, E. Ng, and A. Laude, "Computer-aided diagnosis of diabetic retinopathy: Areview," *Computers in Biology and Medicine*, vol. 43, no. 12, pp. 2136–2155, 2013.

[16] A. W. Stitt, T. M. Curtis, M. Chen, R. J. Medina, G. J. McKay, A. Jenkins, T. A. Gardiner, T. J. Lyons, H.-P. Hammes, R. Simó *et al.*, "The progress in understanding and treatment of diabetic retinopathy," *Progress in Retinal and Eye Research*, vol. 51, pp. 156–186, 2016.

[17] J. Amin, M. Sharif, M. Yasmin, H. Ali, and S. L. Fernandes, "A method for the detection and classification of diabetic retinopathy using structural predictors of bright lesions," *Journal of Computational Science*, vol. 19, pp. 153–164, 2017.

[18] M. M. Fraz, P. Remagnino, A. Hoppe, B. Uyyanonvara, A. R. Rudnicka, C. G. Owen, and S. A. Barman, "Blood vessel segmentation methodologies in retinal images–A survey," *Computer Methods and Programs in Biomedicine*, vol. 108, no. 1, pp. 407–433, 2012.

[19] Q. Abbas, I. Fondon, A. Sarmiento, S. Jiménez, and P. Alemany, "Automatic recognition of severity level for diagnosis of diabetic retinopathy using deep visual features," *Medical & Biological Engineering & Computing*, vol. 55, no. 11, pp. 1959–1974, 2017.

[20] U. R. Acharya, M. R. K. Mookiah, J. E. Koh, J. H. Tan, S. V. Bhandary, A. K. Rao, H. Fujita, Y. Hagiwara, C. K. Chua, and A. Laude, "Automated screening system for retinal health using bi-dimensional empirical mode decomposition and integrated index," *Computers in Biology and Medicine*, vol. 75, pp. 54–62, 2016.

[21] D. S. Ting, W.-C. Wu, and C. Toth, "Deep learning for retinopathy of prematurity screening," 2019.

[22] B. D. Barkana, I. Saricicek, and B. Yildirim, "Performance analysis of descriptive statistical features in retinal vessel segmentation via fuzzy logic, ANN, SVM, and classifier fusion," *Knowledge-Based Systems*, vol. 118, pp. 165–176, 2017.

[23] H. Pratt, F. Coenen, D. M. Broadbent, S. P. Harding, and Y. Zheng, "Convolutional neural networks for diabetic retinopathy," *Procedia Computer Science*, vol. 90, pp. 200–205, 2016.

[24] M. I. Razzak, S. Naz, and A. Zaib, "Deep learning for medical image processing: Overview, challenges and the future," in *Classification in BioApps*. Springer, 2018, pp. 323–350.

[25] K. Xu, D. Feng, and H. Mi, "Deep convolutional neural network-based early automated detection of diabetic retinopathy using fundus image," *Molecules*, vol. 22, no. 12, p. 2054, 2017.

[26] F. Zabihollahy, A. Lochbihler, and E. Ukwatta, "Deep learning based approach for fully automated detection and segmentation of hard exudate from retinal images," in *Medical Imaging 2019: Biomedical Applications in Molecular, Structural, and Functional Imaging*, vol. 10953. International Society for Optics and Photonics, 2019, p. 1095308.

[27] S. Keel, J. Wu, P. Y. Lee, J. Scheetz, and M. He, "Visualizing deep learning models for the detection of referable diabetic retinopathy and glaucoma," *JAMA Ophthalmology*, vol. 137, no. 3, pp. 288–292, 2019.

[28] R. J. Winder, P. J. Morrow, I. N. McRitchie, J. Bailie, and P. M. Hart, "Algorithms for digital image processing in diabetic retinopathy," *Computerized Medical Imaging and Graphics*, vol. 33, no. 8, pp. 608–622, 2009.

[29] T. Teng, M. Lefley, and D. Claremont, "Progress towards automated diabetic ocular screening: A review of image analysis and intelligent systems for diabetic retinopathy," *Medical and Biological Engineering and Computing*, vol. 40, no. 1, pp. 2–13, 2002.

[30] N. Patton, T. M. Aslam, T. MacGillivray, I. J. Deary, B. Dhillon, R. H. Eikelboom, K. Yogesan, and I. J. Constable, "Retinal image analysis: Concepts, applications and potential," *Progress in Retinal and Eye Research*, vol. 25, no. 1, pp. 99–127, 2006.

[31] I. Qureshi, M. Sharif, M. Yasmin, M. Raza, and M. Y Javed, "Computer aided systems for diabetic retinopathy detection using digital fundus images: A survey," *Current Medical Imaging Reviews*, vol. 12, no. 4, pp. 234–241, 2016.

[32] C. I. Sánchez, M. Niemeijer, I. Išgum, A. Dumitrescu, M. S. Suttorp-Schulten, M. D. Abràmoff, and B. van Ginneken, "Contextual computer-aided detection: Improving bright lesion detection in retinal images and coronary calcification identification in CT scans," *Medical Image Analysis*, vol. 16, no. 1, pp. 50–62, 2012.

[33] B. Antal and A. Hajdu, "An ensemble-based system for automatic screening of diabetic retinopathy," *Knowledge-Based Systems*, vol. 60, pp. 20–27, 2014.

[34] I. Qureshi, J. Ma, and Q. Abbas, "Recent development on detection methods for the diagnosis of diabetic retinopathy," *Symmetry*, vol. 11, no. 6, p. 749, 2019.

[35] R. Besenczi, J. Tóth, and A. Hajdu, "A review on automatic analysis techniques for color fundus photographs," *Computational and Structural Biotechnology Journal*, vol. 14, pp. 371–384, 2016.

[36] J. Kaur and D. Mittal, "A generalized method for the detection of vascular structure in pathological retinal images," *Biocybernetics and Biomedical Engineering*, vol. 37, no. 1, pp. 184–200, 2017.

[37] L. C. Neto, G. L. Ramalho, J. F. R. Neto, R. M. Veras, and F. N. Medeiros, "An unsupervised coarse-to-fine algorithm for blood vessel segmentation in fundus images," *Expert Systems with Applications*, vol. 78, pp. 182–192, 2017.

[38] G. Gupta, S. Kulasekaran, K. Ram, N. Joshi, M. Sivaprakasam, and R. Gandhi, "Local characterization of neovascularization and identification of proliferative diabetic retinopathy in retinal fundus images," *Computerized Medical Imaging and Graphics*, vol. 55, pp. 124–132, 2017.

[39] P. Vostatek, E. Claridge, H. Uusitalo, M. Hauta-Kasari, P. Fält, and L. Lensu, "Performance comparison of publicly available retinal blood vessel segmentation methods," *Computerized Medical Imaging and Graphics*, vol. 55, pp. 2–12, 2017.

[40] G. Quellec, M. Lamard, A. Erginay, A. Chabouis, P. Massin, B. Cochener, and G. Cazuguel, "Automatic detection of referral patients due to retinal pathologies through data mining," *Medical Image Analysis*, vol. 29, pp. 47–64, 2016.

[41] R. GeethaRamani and L. Balasubramanian, "Retinal blood vessel segmentation employing image processing and data mining techniques for computerized retinal image analysis," *Biocybernetics and Biomedical Engineering*, vol. 36, no. 1, pp. 102–118, 2016.

[42] L. Zhang, M. Fisher, and W. Wang, "Retinal vessel segmentation using multiscale textons derived from keypoints," *Computerized Medical Imaging and Graphics*, vol. 45, pp. 47–56, 2015.

[43] J. H. Tan, U. R. Acharya, S. V. Bhandary, K. C. Chua, and S. Sivaprasad, "Segmentation of optic disc, fovea and retinal vasculature using a single convolutional neural network," *Journal of Computational Science*, vol. 20, pp. 70–79, 2017.

[44] S. Wang, Y. Yin, G. Cao, B. Wei, Y. Zheng, and G. Yang, "Hierarchical retinal blood vessel segmentation based on feature and ensemble learning," *Neurocomputing*, vol. 149, pp. 708–717, 2015.

[45] N. P. Singh and R. Srivastava, "Retinal blood vessels segmentation by using Gumbel probability distribution function based matched filter," *Computer Methods and Programs in Biomedicine*, vol. 129, pp. 40–50, 2016.

[46] S. Aslani and H. Sarnel, "A new supervised retinal vessel segmentation method based on robust hybrid features," *Biomedical Signal Processing and Control*, vol. 30, pp. 1–12, 2016.

[47] M. Frucci, D. Riccio, G. S. di Baja, and L. Serino, "Severe: Segmenting vessels in retina images," *Pattern Recognition Letters*, vol. 82, pp. 162–169, 2016.

[48] G. Hassan, N. El-Bendary, A. E. Hassanien, A. Fahmy, V. Snasel *et al.*, "Retinal blood vessel segmentation approach based on mathematical morphology," *Procedia Computer Science*, vol. 65, pp. 612–622, 2015.

[49] E. M. Sigurðsson, S. Valero, J. A. Benediktsson, J. Chanussot, H. Talbot, and E. Stefánsson, "Automatic retinal vessel extraction based on directional mathematical morphology and fuzzy classification," *Pattern Recognition Letters*, vol. 47, pp. 164–171, 2014.

[50] H. Pang, C. Luo, and C. Wang, "Improvement of the application of diabetic retinopathy detection model," *Wireless Personal Communications*, vol. 103, no. 1, pp. 611–624, 2018.

[51] S. S. Kar and S. P. Maity, "Retinal blood vessel extraction using tunable bandpass filter and fuzzy conditional entropy," *Computer Methods and Programs in Biomedicine*, vol. 133, pp. 111–132, 2016.

[52] Y. Zhao, J. Zhao, J. Yang, Y. Liu, Y. Zhao, Y. Zheng, L. Xia, and Y. Wang, "Saliency driven vasculature segmentation with infinite perimeter active contour model," *Neurocomputing*, vol. 259, pp. 201–209, 2017.

[53] D. Pandey, X. Yin, H. Wang, and Y. Zhang, "Accurate vessel segmentation using maximum entropy incorporating line detection and phase-preserving denoising," *Computer Vision and Image Understanding*, vol. 155, pp. 162–172, 2017.

[54] A. Christodoulidis, T. Hurtut, H. B. Tahar, and F. Cheriet, "A multi-scale tensor voting approach for small retinal vessel segmentation in high resolution fundus images," *Computerized Medical Imaging and Graphics*, vol. 52, pp. 28–43, 2016.

[55] F. Farokhian, C. Yang, H. Demirel, S. Wu, and I. Beheshti, "Automatic parameters selection of gabor filters with the imperialism competitive algorithm with application to retinal vessel segmentation," *Biocybernetics and Biomedical Engineering*, vol. 37, no. 1, pp. 246–254, 2017.

[56] G. Kovács and A. Hajdu, "A self-calibrating approach for the segmentation of retinal vessels by template matching and contour reconstruction," *Medical Image Analysis*, vol. 29, pp. 24–46, 2016.

[57] S. S. Kar and S. P. Maity, "Blood vessel extraction and optic disc removal using curvelet transform and kernel fuzzy c-means," *Computers in Biology and Medicine*, vol. 70, pp. 174–189, 2016.

[58] Y. Q. Zhao, X. H. Wang, X. F. Wang, and F. Y. Shih, "Retinal vessels segmentation based on level set and region growing," *Pattern Recognition*, vol. 47, no. 7, pp. 2437–2446, 2014.

[59] D. Koukounis, C. Ttofis, A. Papadopoulos, and T. Theocharides, "A high performance hardware architecture for portable, low-power retinal vessel segmentation," *Integration*, vol. 47, no. 3, pp. 377–386, 2014.

[60] E. Imani, M. Javidi, and H.-R. Pourreza, "Improvement of retinal blood vessel detection using morphological component analysis," *Computer Methods and Programs in Biomedicine*, vol. 118, no. 3, pp. 263–279, 2015.

[61] S. Bharkad, "Automatic segmentation of optic disk in retinal images," *Biomedical Signal Processing and Control*, vol. 31, pp. 483–498, 2017.

[62] M. Alshayeji, S. A. Al-Roomi, and S. Abed, "Optic disc detection in retinal fundus images using gravitational law-based edge detection," *Medical & Biological Engineering & Computing*, vol. 55, no. 6, pp. 935–948, 2017.

[63] M. P. Sarathi, M. K. Dutta, A. Singh, and C. M. Travieso, "Blood vessel inpainting based technique for efficient localization and segmentation of optic disc in digital fundus images," *Biomedical Signal Processing and Control*, vol. 25, pp. 108–117, 2016.

[64] A. Singh, M. K. Dutta, M. ParthaSarathi, V. Uher, and R. Burget, "Image processing based automatic diagnosis of glaucoma using wavelet features of segmented optic disc from fundus image," *Computer Methods and Programs in Biomedicine*, vol. 124, pp. 108–120, 2016.

[65] S. Abed, S. A. Al-Roomi, and M. Al-Shayeji, "Effective optic disc detection method based on swarm intelligence techniques and novel pre-processing steps," *Applied Soft Computing*, vol. 49, pp. 146–163, 2016.

[66] B. Dashtbozorg, A. M. Mendonça, and A. Campilho, "Optic disc segmentation using the sliding band filter," *Computers in Biology and Medicine*, vol. 56, pp. 1–12, 2015.

[67] D. Díaz-Pernil, I. Fondón, F. Peña-Cantillana, and M. A. Gutiérrez-Naranjo, "Fully automatized parallel segmentation of the optic disc in retinal fundus images," *Pattern Recognition Letters*, vol. 83, pp. 99–107, 2016.

[68] M. C. V. S. Mary, E. B. Rajsingh, J. K. K. Jacob, D. Anandhi, U. Amato, and S. E. Selvan, "An empirical study on optic disc segmentation using an active contour model," *Biomedical Signal Processing and Control*, vol. 18, pp. 19–29, 2015.

[69] P. S. Mittapalli and G. B. Kande, "Segmentation of optic disk and optic cup from digital fundus images for the assessment of glaucoma," *Biomedical Signal Processing and Control*, vol. 24, pp. 34–46, 2016.

[70] B. Harangi and A. Hajdu, "Detection of the optic disc in fundus images by combining probability models," *Computers in Biology and Medicine*, vol. 65, pp. 10–24, 2015.

[71] L. Xiong and H. Li, "An approach to locate optic disc in retinal images with pathological changes," *Computerized Medical Imaging and Graphics*, vol. 47, pp. 40–50, 2016.

[72] I. Qureshi, "Glaucoma detection in retinal images using image processing techniques: A survey," *International Journal of Advanced Networking and Applications*, vol. 7, no. 2, p. 2705, 2015.

[73] R. P. Rajaiah and R. J. Britto, "Optic disc boundary detection and cup segmentation for prediction of glaucoma," *Int J Sci Eng Technol Res (IJSETR)*, vol. 3, no. 10, pp. 2665–2672, 2014.

[74] N.-M. Tan, Y. Xu, W. B. Goh, and J. Liu, "Robust multi-scale superpixel classification for optic cup localization," *Computerized Medical Imaging and Graphics*, vol. 40, pp. 182–193, 2015.

[75] J. Zilly, J. M. Buhmann, and D. Mahapatra, "Glaucoma detection using entropy sampling and ensemble learning for automatic optic cup and disc segmentation," *Computerized Medical Imaging and Graphics*, vol. 55, pp. 28–41, 2017.

[76] A. Chakravarty and J. Sivaswamy, "Joint optic disc and cup boundary extraction from monocular fundus images," *Computer Methods and Programs in Biomedicine*, vol. 147, pp. 51–61, 2017.

[77] R. Arnay, F. Fumero, and J. Sigut, "Ant colony optimization-based method for optic cup segmentation in retinal images," *Applied Soft Computing*, vol. 52, pp. 409–417, 2017.

[78] M. S. Miri, M. D. Abràmoff, K. Lee, M. Niemeijer, J.-K. Wang, Y. H. Kwon, and M. K. Garvin, "Multimodal segmentation of optic disc and cup from SD-OCT and color fundus photographs using a machine-learning graph-based approach," *IEEE Transactions on Medical Imaging*, vol. 34, no. 9, pp. 1854–1866, 2015.

[79] A. Issac, M. Parthasarthi, and M. K. Dutta, "An adaptive threshold based algorithm for optic disc and cup segmentation in fundus images," in *2015 2nd International Conference on Signal Processing and Integrated Networks (SPIN)*. IEEE, 2015, pp. 143–147.

[80] M. Habib, R. Welikala, A. Hoppe, C. Owen, A. Rudnicka, and S. Barman, "Detection of microaneurysms in retinal images using an ensemble classifier," *Informatics in Medicine Unlocked*, vol. 9, pp. 44–57, 2017.

[81] M. Kumar and M. K. Nath, "Detection of microaneurysms and exudates from color fundus images by using SBGFRLS."

[82] S. Sreng, N. Maneerat, and K. Hamamoto, "Automated microaneurysms detection in fundus images using image segmentation," in *2017 International Conference on Digital Arts, Media and Technology (ICDAMT)*. IEEE, 2017, pp. 19–23.

[83] C. Pereira, D. Veiga, J. Mahdjoub, Z. Guessoum, L. Gonçalves, M. Ferreira, and J. Monteiro, "Using a multi-agent system approach for microaneurysm detection in fundus images," *Artificial Intelligence in Medicine*, vol. 60, no. 3, pp. 179–188, 2014.

[84] S. Agarwal, K. Acharjya, S. K. Sharma, and S. Pandita, "Automatic computer aided diagnosis for early diabetic retinopathy detection and monitoring: A comprehensive review," in *2016 Online International Conference on Green Engineering and Technologies (IC-GET)*. IEEE, 2016, pp. 1–7.

[85] B. Wu, W. Zhu, F. Shi, S. Zhu, and X. Chen, "Automatic detection of microaneurysms in retinal fundus images," *Computerized Medical Imaging and Graphics*, vol. 55, pp. 106–112, 2017.

[86] R. Rosas-Romero, J. Martínez-Carballido, J. Hernández-Capistrán, and L. J. Uribe-Valencia, "A method to assist in the diagnosis of early diabetic retinopathy: Image processing applied to detection of microaneurysms in fundus images," *Computerized Medical Imaging and Graphics*, vol. 44, pp. 41–53, 2015.

[87] M. Tavakoli, R. P. Shahri, H. Pourreza, A. Mehdizadeh, T. Banaee, and M. H. B. Toosi, "A complementary method for automated detection of microaneurysms in fluorescein angiography fundus images to assess diabetic retinopathy," *Pattern Recognition*, vol. 46, no. 10, pp. 2740–2753, 2013.

[88] A. Sopharak, B. Uyyanonvara, and S. Barman, "Simple hybrid method for fine microaneurysm detection from non-dilated diabetic retinopathy retinal images," *Computerized Medical Imaging and Graphics*, vol. 37, no. 5-6, pp. 394–402, 2013.

[89] N. S. Datta, H. S. Dutta, M. De, and S. Mondal, "An effective approach: Image quality enhancement for microaneurysms detection of non-dilated retinal fundus image," *Procedia Technology*, vol. 10, pp. 731–737, 2013.

[90] B. Zhang, F. Karray, Q. Li, and L. Zhang, "Sparse representation classifier for microaneurysm detection and retinal blood vessel extraction," *Information Sciences*, vol. 200, pp. 78–90, 2012.

[91] M. U. Akram, S. Khalid, and S. A. Khan, "Identification and classification of microaneurysms for early detection of diabetic retinopathy," *Pattern Recognition*, vol. 46, no. 1, pp. 107–116, 2013.

[92] W. Zhou, C. Wu, D. Chen, Y. Yi, and W. Du, "Automatic microaneurysm detection using the sparse principal component analysis-based unsupervised classification method," *IEEE Access*, vol. 5, pp. 2563–2572, 2017.

[93] F. Ren, P. Cao, W. Li, D. Zhao, and O. Zaiane, "Ensemble based adaptive over-sampling method for imbalanced data learning in computer aided detection of microaneurysm," *Computerized Medical Imaging and Graphics*, vol. 55, pp. 54–67, 2017.

[94] M. Javidi, H.-R. Pourreza, and A. Harati, "Vessel segmentation and microaneurysm detection using discriminative dictionary learning and sparse representation," *Computer Methods and Programs in Biomedicine*, vol. 139, pp. 93–108, 2017.

[95] J. Shan and L. Li, "A deep learning method for microaneurysm detection in fundus images," in *2016 IEEE First International Conference on Connected Health: Applications, Systems and Engineering Technologies (CHASE)*. IEEE, 2016, pp. 357–358.

[96] R. Srivastava, L. Duan, D. W. Wong, J. Liu, and T. Y. Wong, "Detecting retinal microaneurysms and hemorrhages with robustness to the presence of blood vessels," *Computer Methods and Programs in Biomedicine*, vol. 138, pp. 83–91, 2017.

[97] K. M. Adal, D. Sidibé, S. Ali, E. Chaum, T. P. Karnowski, and F. Mériaudeau, "Automated detection of microaneurysms using scale-adapted blob analysis and semi-supervised learning," *Computer Methods and Programs in Biomedicine*, vol. 114, no. 1, pp. 1–10, 2014.

[98] N. Kaur, S. Chatterjee, M. Acharyya, J. Kaur, N. Kapoor, and S. Gupta, "A supervised approach for automated detection of hemorrhages in retinal fundus images," in *2016 5th International Conference on Wireless Networks and Embedded Systems (WECON)*. IEEE, 2016, pp. 1–5.

[99] L. Zhou, P. Li, Q. Yu, Y. Qiao, and J. Yang, "Automatic hemorrhage detection in color fundus images based on gradual removal of vascular branches," in *2016 IEEE International Conference on Image Processing (ICIP)*. IEEE, 2016, pp. 399–403.

[100] D. Xiao, S. Yu, J. Vignarajan, D. An, M.-L. Tay-Kearney, and Y. Kanagasingam, "Retinal hemorrhage detection by rule-based and machine learning approach," in *2017 39th Annual International Conference of the IEEE Engineering in Medicine and Biology Society (EMBC)*. IEEE, 2017, pp. 660–663.

[101] G. Arun and N. Sasirekha, "Detection of retinal hemorrhage in color fundus image using splat feature segmentation," in *2015 International Conference on Innovations in Information, Embedded and Communication Systems (ICIIECS)*. IEEE, 2015, pp. 1–5.

[102] L. Tang, M. Niemeijer, J. M. Reinhardt, M. K. Garvin, and M. D. Abramoff, "Splat feature classification with application to retinal hemorrhage detection in fundus images," *IEEE Transactions on Medical Imaging*, vol. 32, no. 2, pp. 364–375, 2012.

[103] L. Tang, M. Niemeijer, and M. D. Abramoff, "Splat feature classification: Detection of the presence of large retinal hemorrhages," in *2011 IEEE International Symposium on Biomedical Imaging: From Nano to Macro*. IEEE, 2011, pp. 681–684.

[104] J. M. Molina-Casado, E. J. Carmona, and J. García-Feijoó, "Fast detection of the main anatomical structures in digital retinal images based on intra- and inter-structure relational knowledge," *Computer Methods and Programs in Biomedicine*, vol. 149, pp. 55–68, 2017.

[105] A. Ashraf, M. U. Akram, S. A. Sheikh, and S. Abbas, "Detection of macular whitening and retinal hemorrhages for diagnosis of malarial retinopathy," in *2015 IEEE International Conference on Imaging Systems and Techniques (IST)*. IEEE, 2015, pp. 1–5.

[106] A. Sharma, M. K. Dutta, A. Singh, M. Parthasarathi, and C. M. Travieso, "Dynamic thresholding technique for detection of hemorrhages in retinal images," in *2014 Seventh International Conference on Contemporary Computing (IC3)*. IEEE, 2014, pp. 113–116.

[107] S. Lahmiri and A. Shmuel, "Variational mode decomposition based approach for accurate classification of color fundus images with hemorrhages," *Optics & Laser Technology*, vol. 96, pp. 243–248, 2017.

[108] Q. Liu, B. Zou, J. Chen, W. Ke, K. Yue, Z. Chen, and G. Zhao, "A location-to-segmentation strategy for automatic exudate segmentation in colour retinal fundus images," *Computerized Nedical Imaging and Graphics*, vol. 55, pp. 78–86, 2017.

[109] E. Imani and H.-R. Pourreza, "A novel method for retinal exudate segmentation using signal separation algorithm," *Computer Methods and Programs in Biomedicine*, vol. 133, pp. 195–205, 2016.

[110] B. Harangi and A. Hajdu, "Automatic exudate detection by fusing multiple active contours and regionwise classification," *Computers in Biology and Medicine*, vol. 54, pp. 156–171, 2014.

[111] X. Zhang, G. Thibault, E. Decencière, B. Marcotegui, B. Laÿ, R. Danno, G. Cazuguel, G. Quellec, M. Lamard, P. Massin *et al.*, "Exudate detection in color retinal images for mass screening of diabetic retinopathy," *Medical Image Analysis*, vol. 18, no. 7, pp. 1026–1043, 2014.

[112] H. Tjandrasa, R. E. Putra, A. Y. Wijaya, and I. Arieshanti, "Classification of non-proliferative diabetic retinopathy based on hard exudates using soft margin SVM," in *2013 IEEE International Conference on Control System, Computing and Engineering*. IEEE, 2013, pp. 376–380.

[113] M. U. Akram, S. Khalid, A. Tariq, S. A. Khan, and F. Azam, "Detection and classification of retinal lesions for grading of diabetic retinopathy," *Computers in Biology and Medicine*, vol. 45, pp. 161–171, 2014.

[114] M. Omar, F. Khelifi, and M. A. Tahir, "Detection and classification of retinal fundus images exudates using region based multiscale LBP texture approach," in *2016 International Conference on Control, Decision and Information Technologies (CoDIT)*. IEEE, 2016, pp. 227–232.

[115] S. Banerjee and D. Kayal, "Detection of hard exudates using mean shift and normalized cut method," *Biocybernetics and Biomedical Engineering*, vol. 36, no. 4, pp. 679–685, 2016.

[116] M. M. Fraz, W. Jahangir, S. Zahid, M. M. Hamayun, and S. A. Barman, "Multiscale segmentation of exudates in retinal images using contextual cues and ensemble classification," *Biomedical Signal Processing and Control*, vol. 35, pp. 50–62, 2017.

[117] P. Prentasic, "Detection of diabetic retinopathy in fundus photographs," *University of Zagreb, Faculty of Electrical Engineering and Computing Unska*, vol. 3, no. 10000, pp. 6–8, 2013.

[118] D. Sidibé, I. Sadek, and F. Mériaudeau, "Discrimination of retinal images containing bright lesions using sparse coded features and SVM," *Computers in Biology and Medicine*, vol. 62, pp. 175–184, 2015.

[119] M. P. Paing, S. Choomchuay, and M. R. Yodprom, "Detection of lesions and classification of diabetic retinopathy using fundus images," in *2016 9th Biomedical Engineering International Conference (BMEiCON)*. IEEE, 2016, pp. 1–5.

[120] M. García, C. Valverde, M. I. López, J. Poza, and R. Hornero, "Comparison of logistic regression and neural network classifiers in the detection of hard exudates in retinal images," in *2013 35th Annual International Conference of the IEEE Engineering in Medicine and Biology Society (EMBC)*. IEEE, 2013, pp. 5891–5894.

[121] L. Laaksonen, A. Hannuksela, E. Claridge, P. Fält, M. Hauta-Kasari, H. Uusitalo, and L. Lensu, "Evaluation of feature sensitivity to training data inaccuracy in detection of retinal lesions," in *2016 Sixth International Conference on Image Processing Theory, Tools and Applications (IPTA)*. IEEE, 2016, pp. 1–6.

[122] C. Pereira, L. Gonçalves, and M. Ferreira, "Exudate segmentation in fundus images using an ant colony optimization approach," *Information Sciences*, vol. 296, pp. 14–24, 2015.

[123] I. N. Figueiredo, S. Kumar, C. M. Oliveira, J. D. Ramos, and B. Engquist, "Automated lesion detectors in retinal fundus images," *Computers in Biology and Medicine*, vol. 66, pp. 47–65, 2015.

[124] P. Prentašić and S. Lončarić, "Detection of exudates in fundus photographs using deep neural networks and anatomical landmark detection fusion," *Computer Methods and Programs in Biomedicine*, vol. 137, pp. 281–292, 2016.

[125] S. A. G. Naqvi, M. F. Zafar, and I. ul Haq, "Referral system for hard exudates in eye fundus," *Computers in Biology and Medicine*, vol. 64, pp. 217–235, 2015.

[126] J. Kaur and D. Mittal, "A generalized method for the segmentation of exudates from pathological retinal fundus images," *Biocybernetics and Biomedical Engineering*, vol. 38, no. 1, pp. 27–53, 2018.

[127] B. Al-Bander, W. Al-Nuaimy, B. M. Williams, and Y. Zheng, "Multiscale sequential convolutional neural networks for simultaneous detection of fovea and optic disc," *Biomedical Signal Processing and Control*, vol. 40, pp. 91–101, 2018.

[128] R. Gargeya and T. Leng, "Automated identification of diabetic retinopathy using deep learning," *Ophthalmology*, vol. 124, no. 7, pp. 962–969, 2017.

[129] P. S. Silva, H. El-Rami, R. Barham, A. Gupta, A. Fleming, J. van Hemert, J. D. Cavallerano, J. K. Sun, and L. P. Aiello, "Hemorrhage and/or microaneurysm severity and count in ultrawide field images and early treatment diabetic retinopathy study photography," *Ophthalmology*, vol. 124, no. 7, pp. 970–976, 2017.

[130] J. Dash and N. Bhoi, "A thresholding based technique to extract retinal blood vessels from fundus images," *Future Computing and Informatics Journal*, vol. 2, no. 2, pp. 103–109, 2017.

[131] G. Leontidis, B. Al-Diri, and A. Hunter, "A new unified framework for the early detection of the progression to diabetic retinopathy from fundus images," *Computers in Biology and Medicine*, vol. 90, pp. 98–115, 2017.

[132] J. E. Koh, U. R. Acharya, Y. Hagiwara, U. Raghavendra, J. H. Tan, S. V. Sree, S. V. Bhandary, A. K. Rao, S. Sivaprasad, K. C. Chua *et al.*, "Diagnosis of retinal health in digital fundus images using continuous wavelet transform (CWT) and entropies," *Computers in Biology and Medicine*, vol. 84, pp. 89–97, 2017.

[133] M. Lane, V. Lane, J. Abbott, T. Braithwaite, P. Shah, and A. K. Denniston, "Multiple deprivation, vision loss, and ophthalmic disease in adults: Global perspectives," *Survey of Ophthalmology*, vol. 63, no. 3, pp. 406–436, 2018.

[134] B. Barua and M. M. Hasan, "A new approach of detection and segmentation of blood vessels for the classification of healthy and diseased retinal images," in *2016 3rd International Conference on Electrical Engineering and Information Communication Technology (ICEEICT)*. IEEE, 2016, pp. 1–6.

[135] R. Santhakumar, M. Tandur, E. Rajkumar, K. Geetha, G. Haritz, and K. T. Rajamani, "Machine learning algorithm for retinal image analysis," in *2016 IEEE Region 10 Conference (TENCON)*. IEEE, 2016, pp. 1236–1240.

[136] N. Asiri, M. Hussain, F. Al Adel, and N. Alzaidi, "Deep learning based computer-aided diagnosis systems for diabetic retinopathy: A survey," *Artificial Intelligence in Medicine*, 2019.

[137] K. Bhatia, S. Arora, and R. Tomar, "Diagnosis of diabetic retinopathy using machine learning classification algorithm," in *2016 2nd International Conference on Next Generation Computing Technologies (NGCT)*. IEEE, 2016, pp. 347–351.

[138] S. Devarakonda, K. Vupparaboina, A. Richhariya, J. Chhablani, and S. Jana, "Automated detection of retinal disorders from OCT images using artificial neural network," in *2016 IEEE Annual India Conference (INDICON)*. IEEE, 2016, pp. 1–6.

[139] H. H. Vo and A. Verma, "New deep neural nets for fine-grained diabetic retinopathy recognition on hybrid color space," in *2016 IEEE International Symposium on Multimedia (ISM)*. IEEE, 2016, pp. 209–215.

[140] A. Lahiri, A. G. Roy, D. Sheet, and P. K. Biswas, "Deep neural ensemble for retinal vessel segmentation in fundus images towards achieving label-free angiography," in *2016 38th Annual International Conference of the IEEE Engineering in Medicine and Biology Society (EMBC)*. IEEE, 2016, pp. 1340–1343.

[141] X. Wang, L. Zhang, L. Lin, Z. Liang, and W. Zuo, "Deep joint task learning for generic object extraction," in *Advances in Neural Information Processing Systems*, 2014, pp. 523–531.

[142] R. F. Mansour, "Deep-learning-based automatic computer-aided diagnosis system for diabetic retinopathy," *Biomedical Engineering Letters*, vol. 8, no. 1, pp. 41–57, 2018.

[143] J. Lachure, A. Deorankar, S. Lachure, S. Gupta, and R. Jadhav, "Diabetic retinopathy using morphological operations and machine learning," in *2015 IEEE International Advance Computing Conference (IACC)*. IEEE, 2015, pp. 617–622.

[144] P. Nijalingappa and B. Sandeep, "Machine learning approach for the identification of diabetes retinopathy and its stages," in *2015 International Conference on Applied and Theoretical Computing and Communication Technology (iCATccT)*. IEEE, 2015, pp. 653–658.

[145] A. Kunwar, S. Magotra, and M. P. Sarathi, "Detection of high-risk macular edema using texture features and classification using SVM."

[146] J. T. Arenas-Cavalli, S. A. Rios, M. Pola, and R. Donoso, "A web-based platform for automated diabetic retinopathy screening," *Procedia Computer Science*, vol. 60, pp. 557–563, 2015.

[147] Y. Guo, Y. Liu, A. Oerlemans, S. Lao, S. Wu, and M. S. Lew, "Deep learning for visual understanding: A review," *Neurocomputing*, vol. 187, pp. 27–48, 2016.

[148] Q. Abbas, M. Ibrahim, and M. Jaffar, "Video scene analysis:An overview and challenges on deep learning algorithms. j multimed tools appl," 2017.

[149] Y. Peng, S. Dharssi, Q. Chen, T. D. Keenan, E. Agrón, W. T. Wong, E. Y. Chew, and Z. Lu, "Deepseenet: A deep learning model for automated classification of patient-based age-related macular degeneration severity from color fundus photographs," *Ophthalmology*, vol. 126, no. 4, pp. 565–575, 2019.

[150] F. D. Verbraak, M. D. Abramoff, G. C. Bausch, C. Klaver, G. Nijpels, R. O. Schlingemann, and A. A. van der Heijden, "Diagnostic accuracy of a device for the automated detection of diabetic retinopathy in a primary care setting," *Diabetes Care*, vol. 42, no. 4, pp. 651–656, 2019.

[151] T. A. Soomro, J. Gao, T. Khan, A. F. M. Hani, M. A. Khan, and M. Paul, "Computerised approaches for the detection of diabetic retinopathy using retinal fundus images: A survey," *Pattern Analysis and Applications*, vol. 20, no. 4, pp. 927–961, 2017.

[152] W. Zhang, J. Zhong, S. Yang, Z. Gao, J. Hu, Y. Chen, and Z. Yi, "Automated identification and grading system of diabetic retinopathy using deep neural networks," *Knowledge-Based Systems*, vol. 175, pp. 12–25, 2019.

[153] G. García, J. Gallardo, A. Mauricio, J. López, and C. Del Carpio, "Detection of diabetic retinopathy based on a convolutional neural network using retinal fundus images," in *International Conference on Artificial Neural Networks*. Springer, 2017, pp. 635–642.

[154] S. Otálora, O. Perdomo, F. González, and H. Müller, "Training deep convolutional neural networks with active learning for exudate classification in eye fundus images," in *Intravascular Imaging and Computer Assisted Stenting, and Large-Scale Annotation of Biomedical Data and Expert Label Synthesis*. Springer, 2017, pp. 146–154.

[155] R. Arunkumar and P. Karthigaikumar, "Multi-retinal disease classification by reduced deep learning features," *Neural Computing and Applications*, vol. 28, no. 2, pp. 329–334, 2017.

[156] B. Akilesh, T. Marwah, V. N. Balasubramanian, and K. Rajamani, "On the relevance of very deep networks for diabetic retinopathy diagnostics," in *Applications of Cognitive Computing Systems and IBM Watson.* Springer, 2017, pp. 47–54.

[157] S. K. Raju Maher and D. M. Dhopeshwarkar, "Review of automated detection for diabetes retinopathy using fundus images," *International Journal of Advanced Research in Computer Science and Software Engineering*, vol. 5, no. 3, 2015.

[158] N. Thomas and T. Mahesh, "Detecting clinical features of diabetic retinopathy using image processing," *International Journal of Engineering Research & Technology (IJERT)*, vol. 3, no. 8, pp. 558–561, 2014.

[159] P. M. Bossuyt, J. B. Reitsma, D. E. Bruns, C. A. Gatsonis, P. P. Glasziou, L. M. Irwig, J. G. Lijmer, D. Moher, D. Rennie, and H. C. De Vet, "Towards complete and accurate reporting of studies of diagnostic accuracy: The stard initiative," *Radiology*, vol. 226, no. 1, pp. 24–28, 2003.

[160] I. Qureshi, J. Ma, and K. Shaheed, "A hybrid proposed fundus image enhancement framework for diabetic retinopathy," *Algorithms*, vol. 12, no. 1, p. 14, 2019.

[161] A. Ashraf, M. U. Akram, and S. A. Sheikh, "Detection of retinal whitening, cotton wool spots and retinal hemorrhages for diagnosis of malarial retinopathy," in *TENCON 2015-2015 IEEE Region 10 Conference.* IEEE, 2015, pp. 1–5.

[162] K. He and J. Sun, "Convolutional neural networks at constrained time cost," in *Proceedings of the IEEE Conference on Computer Vision and Pattern Recognition*, 2015, pp. 5353–5360.

[163] H. Li, R. Zhao, and X. Wang, "Highly efficient forward and backward propagation of convolutional neural networks for pixelwise classification," *arXiv preprint arXiv:1412.4526*, 2014.

[164] W. Ouyang, P. Luo, X. Zeng, S. Qiu, Y. Tian, H. Li, S. Yang, Z. Wang, Y. Xiong, C. Qian *et al.*, "Deepid-net: Multi-stage and deformable deep convolutional neural networks for object detection," *arXiv preprint arXiv:1409.3505*, 2014.

[165] Y. Sun, X. Wang, and X. Tang, "Deep convolutional network cascade for facial point detection," in *Proceedings of the IEEE Conference on Computer Vision and Pattern Recognition*, 2013, pp. 3476–3483.

[166] S. Mallat, *A Wavelet Tour of Signal Processing.* Elsevier, 1999.

[167] D. L. Donoho, "De-noising by soft-thresholding," *IEEE Transactions on Information Theory*, vol. 41, no. 3, pp. 613–627, 1995.

[168] S. Tan, L. Jiao, and I. A. Kakadiaris, "Wavelet-based bayesian image estimation: From marginal and bivariate prior models to multivariate prior models," *IEEE Transactions on Image Processing*, vol. 17, no. 4, pp. 469–481, 2008.

[169] A. Fathi and A. R. Naghsh-Nilchi, "Efficient image denoising method based on a new adaptive wavelet packet thresholding function," *IEEE Transactions on Image Processing*, vol. 21, no. 9, pp. 3981–3990, 2012.

[170] A. L. Da Cunha, J. Zhou, and M. N. Do, "The nonsubsampled contourlet transform: Theory, design, and applications," *IEEE Transactions on Image Processing*, vol. 15, no. 10, pp. 3089–3101, 2006.

[171] J.-L. Starck, F. D. Murtagh, and A. Bijaoui, *Image Processing and Data Analysis: The Multiscale Approach.* Cambridge University Press, 1998.

[172] R. H. Bamberger and M. J. Smith, "A filter bank for the directional decomposition of images: Theory and design," *IEEE Transactions on Signal Processing*, vol. 40, no. 4, pp. 882–893, 1992.

[173] J. Jia, Y. Zhang, L. Chen, and Z. Zhao, "Normal inverse Gaussian model-based image denoising in the NSCT domain," *Mathematical Problems in Engineering*, vol. 2015, 2015.

[174] R. C. Gonzalez, R. E. Woods, and S. L. Eddins, *Digital Image Processing Using MATLAB.* Pearson Education India, 2004.

[175] O. E. Barndorff-Nielsen, "Normal inverse Gaussian distributions and stochastic volatility modelling," *Scandinavian Journal of Statistics*, vol. 24, no. 1, pp. 1–13, 1997.

[176] M. I. H. Bhuiyan, M. O. Ahmad, and M. Swamy, "Wavelet-based despeckling of medical ultrasound images with the symmetric normal inverse Gaussian prior," in *2007 IEEE International Conference on Acoustics, Speech and Signal Processing-ICASSP'07*, vol. 1. IEEE, 2007, pp. I–721.

[177] X. Zhang and X. Jing, "Image denoising in contourlet domain based on a normal inverse Gaussian prior," *Digital Signal Processing*, vol. 20, no. 5, pp. 1439–1446, 2010.

[178] N. Otsu, "A threshold selection method from gray-level histograms," *IEEE Transactions on Systems, Man, and Cybernetics*, vol. 9, no. 1, pp. 62–66, 1979.

[179] M. S. Miri and A. Mahloojifar, "Retinal image analysis using curvelet transform and multistructure elements morphology by reconstruction," *IEEE Transactions on Biomedical Engineering*, vol. 58, no. 5, pp. 1183–1192, 2010.

[180] V. Jaya and R. Gopikakumari, "IEM: A new image enhancement metric for contrast and sharpness measurements," *International Journal of Computer Applications*, vol. 79, no. 9, 2013.

[181] S. Sekhar, W. Al-Nuaimy, and A. Nandi, "Automatic localization of optic disc and fovea in retinal fundus," in *16th European Signal Processing Conference*, 2008.

[182] J. A. Bangham, R. W. Harvey, P. D. Ling, and R. V. Aldridge, "Morphological scale-space preserving transforms in many dimensions," *Journal of Electronic Imaging*, vol. 5, no. 3, pp. 283–300, 1996.

[183] S. Mukhopadhyay and B. Chanda, "Multiscale morphological segmentation of gray-scale images," *IEEE Transactions on Image Processing*, vol. 12, no. 5, pp. 533–549, 2003.

[184] N. A. Hamadani, "Automatic Target Cueing in IR Imagery." Air Force Inst of Teh Wright-Patterson Afb Oh School of Engineering, Tech. Rep., 1981.

[185] H. Kolb, R. F. Nelson, P. K. Ahnelt, I. Ortuño-Lizarán, and N. Cuenca, "The architecture of the human fovea," *Webvision: The Organization of the Retina and Visual System [Internet]*, 2020.

[186] S. Tick, F. Rossant, I. Ghorbel, A. Gaudric, J.-A. Sahel, P. Chaumet-Riffaud, and M. Paques, "Foveal shape and structure in a normal population," *Investigative Ophthalmology & Visual Science*, vol. 52, no. 8, pp. 5105–5110, 2011.

[187] J. Odstrcilik, R. Kolar, A. Budai, J. Hornegger, J. Jan, J. Gazarek, T. Kubena, P. Cernosek, O. Svoboda, and E. Angelopoulou, "Retinal vessel segmentation by improved matched filtering: Evaluation on a new high-resolution fundus image database," *IET Image Processing*, vol. 7, no. 4, pp. 373–383, 2013.

[188] A. M. Mendonca and A. Campilho, "Segmentation of retinal blood vessels by combining the detection of centerlines and morphological reconstruction," *IEEE Transactions on Medical Imaging*, vol. 25, no. 9, pp. 1200–1213, 2006.

[189] J. Staal, M. D. Abràmoff, M. Niemeijer, M. A. Viergever, and B. Van Ginneken, "Ridge-based vessel segmentation in color images of the retina," *IEEE Transactions on Medical Imaging*, vol. 23, no. 4, pp. 501–509, 2004.

[190] M. E. Martinez-Perez, A. D. Hughes, S. A. Thom, A. A. Bharath, and K. H. Parker, "Segmentation of blood vessels from red-free and fluorescein retinal images," *Medical Image Analysis*, vol. 11, no. 1, pp. 47–61, 2007.

[191] M. Niemeijer, J. Staal, B. van Ginneken, M. Loog, and M. D. Abramoff, "Comparative study of retinal vessel segmentation methods on a new publicly available database," in *Medical Imaging 2004: Image Processing*, vol. 5370. International Society for Optics and Photonics, 2004, pp. 648–656.

[192] J. Sivic and A. Zisserman, "Video google: A text retrieval approach to object matching in videos," in *null*. IEEE, 2003, p. 1470.

[193] E. Decencière, G. Cazuguel, X. Zhang, G. Thibault, J.-C. Klein, F. Meyer, B. Marcotegui, G. Quellec, M. Lamard, R. Danno *et al.*, "Teleophta: Machine learning and image processing methods for teleophthalmology," *Irbm*, vol. 34, no. 2, pp. 196–203, 2013.

[194] "www.chcf.org/blog/artificial-intelligence-eases-burden-of-blindness-in-diabetes/." web.

[195] M. Tan and Q. Le, "Efficientnet: Rethinking model scaling for convolutional neural networks," in *International Conference on Machine Learning*. PMLR, 2019, pp. 6105–6114.

[196] C. François, *Deep Learning with Python*. Manning Publications Company, 2018.

[197] M. L. McHugh, "Interrater reliability:The kappa statistic," *Biochemia Medica: Biochemia Medica*, vol. 22, no. 3, pp. 276–282, 2012.

LIST OF PUBLICATIONS

Journals

1. Noushira K.I,Anil Kumar K.R, Meenakshy K., "A Survey on Feature Extraction Methods in Retinal Fundus Images for Diabetic Retinopathy", International Journal of Computer Sciences and Engineering,ISSN: 2347-2693, Vol.7, Issue 4, April 2019 pp 77-87.

2. Anil Kumar K.R and Meenakshy K.,"Retinal Vasculature Extraction using Non-subsampled Contourlet Transform and Multi-structure Element Morphology by Reconstruction", International Journal of Recent Technology and Engineering, ISSN: 2271-3878, Vol.8, Issue-2, July-2019, pp: 116-125.

3. Anil Kumar K.R.,Noushira K.I., Meenakshy K.," Classification of Diabetic Retinopathy Features using Bag of Feature Model", International Journal of Innovative Technology and Exploring Engineering, ISSN: 2278-3075, Vol-9, Issue-1, Nov 2019, pp: 381-385.

4. Anil Kumar K.R., Megha P.M., and Meenakshy K.,"Diabetic Retinopathy Detection & Classification Techniques: A Review", International Journal of Scientific & Technology Research, ISSN: 2277-8616, Vol-9, Issue-3, March 2020,pp:1621-1628.

Conference

1. Anil Kumar K.R and Meenakshy K.,"Extraction of Blood Vessels in Retinal Images for Automatic Diagnisis of Diabetic Retinopathy", IC-AMMN-2K16, DTE sponsored International Conference on Advances in applied mathematics, materials science and nanotechnology engineering and industrial applications organized by Federal Institute of Science and Technology, Hormis Nagar, Angamaly, Kerala during 07-01-2016 to 09-01-2016.